Experimental study on cohesion of extraterrestrial solid particles: Roles in microgravity

長足，友哉

Doctoral Dissertation

Experimental study on cohesion of extraterrestrial solid particles: Roles in microgravity

(地球外固体粒子の付着力に関する実験的研究:

微小重力場における役割)

January 2022

Graduate School of Science, Kobe University

Yuuya Nagaashi

Abstract

The cohesive force of solid particles is more important in environments where the effect of gravity is smaller. Planets are formed in a disk of sub-micron-sized solid particles, dust, and gas around a star. The cohesive force of the dust has a significant effect on the coagulation process from dust to kilometer-sized planetesimals, which is the first step of planet formation. The cohesive force of solid particles also affects the strength of rubble pile asteroids and the mobility of particles on the surfaces of the bodies, as well as the wind friction threshold speeds for particle movement on bodies with atmosphere. Although natural particles are non-spherical, many theoretical and numerical studies have assumed a cohesive force proportional to the particle size based on measurements of the cohesive force of micron-sized spheres and theories. Indirect cohesive force measurements based on tensile strength measurements of particle aggregates have shown the possibility of a tenfold increase in cohesive force due to heating to remove adsorbed water molecules. In this study, in order to investigate the effect of particle shape and size as well as the water molecule adsorption on cohesive force, we measured the cohesive force of meteorite fragments with and without heating to remove adsorbed water molecules prior to measurements under ambient and reduced pressure.

In Chapter 2, the measurement procedure was presented. The shape of the particles, cohesive force of the particles against a smooth slide at the above various conditions, and the amount of water molecule adsorption at ambient condition were measured. Several tens or several micron-sized meteorite fragments were prepared with a mortar and pestle or by a projectile impact. As a comparison, several tens micron-sized glass and silica particles, and aggregates consisting of submicron-sized amorphous silica spheres were prepared.

In Chapters 3 and 4, the measurements were presented and discussed. Circularity, which corresponds to roughness above micron size in this study, affects the low cohesive force of irregularly shaped particles, and arithmetic mean roughness, which corresponds to roughness above submicron size in this study, affects the low cohesive force of meteorite fragments with rough surfaces. However, there was a six-fold difference in cohesive force among meteorites and aggregates, which have similar circularity and arithmetic mean roughness. Meteorites with finer surface structures found at higher resolution observations using an electron microscope, and fine-grained matrix-rich meteorites tend to have low cohesive force. The measured cohesive force of meteorite fragments of several microns in size was a fraction of that of several tens of microns in

size, but when the small fragments were pressed against a slide with a pressure that did not cause plastic deformation before measurements, the cohesive force of the both became similar. This suggests that under the Earth's gravity, several tens of micron-sized particles contact with a slide at roughly three points, whereas several micron-sized particles contact at a single point. This is supported by the fact that the measured cohesive force of aggregates was several times higher than that of their constituent spheres, which is theoretically predicted from the sphere size. These results also show the cohesive force of meteorite fragments and aggregates is determined by the surface structure, i.e., the constituent grain size, and is independent of the bulk size, unless plastic deformation occurs. The increase in cohesive force due to the removal of adsorbed water molecules was 3–4 times. This is smaller than about 10-fold increase, which was estimated based on tensile strength measurements of aggregates, i.e., an indirect method, even at similar conditions. The calculation based on a simple model of a previous study ignoring the attraction between adsorbed molecules, using the amount of water molecule adsorption in this study, also predicted a larger increase in cohesive force. These suggest that the previous estimates have been overestimates.

In Chapter 5, based on the findings the mobility of particles on the surface of asteroids is discussed. The application to the dust growth in protoplanetary disks was also discussed. The 3–4 fold increase in cohesive force due to the removal of adsorbed water molecules suggests that dust aggregates can grow at higher velocity collisions than those predicted at ambient condition, although not as much as was pointed out in a previous study that assumed a 10-fold increase in surface energy, i.e., cohesive force. Considering the number of contact points between the particles and the slide, and the effect of removal of adsorbed water molecules, the interparticle cohesive force per a contact point of asteroid particles, which is independent of the size unless plastic deformation occurs, was estimated from the measured cohesive force. Based on this estimate, we re-examined the size of particles that can easily move on the surface according to a previous study. Even if the number of contact points and the possibility of plastic deformation on the surface are considered, particles smaller than several tens of centimeters are more mobile than previously estimated assuming that the cohesive force increases linearly with the particle size, and the most mobile particle size is expected to be ~1 cm. This estimate is consistent with the observations that there are signatures of mass movements on asteroid surfaces, and that the size of the particles covering the low areas of asteroid Itokawa and those ejected from asteroid Bennu is millimeter to centimeter.

Contents

Chapter 1

Introduction

1.1 The role of cohesive force in various gravity conditions

1.1.1 Protoplanetary dust particles

The cohesive force of solid particles is important for the early stages of planet formation in protoplanetary disks. A newborn young star is surrounded by a disk of gas and solid particles, dust, which are thought to be submicron in size. This is called a protoplanetary disk, and planets are thought to form by repeated accretion of the dust particles in the disk. Initially, the dust particles are expected to grow to planetesimals, which are kilometer-sized bodies. Once they reach this size, they have self-gravity enough to grow further in subsequent collisions, and are thought to evolve into protoplanets and then planets. However, for bodies smaller than planetesimals, it is difficult to grow gravitationally. The conventional processes proposed for the formation of planetesimals can be divided into two main processes: those due to gravitational instability (Goldreich & Ward 1973) and those due to the van der Waals force induced coagulation (Weidenschilling 1980). The former is difficult to occur because gas turbulence in protoplanetary disks prevents the dust particles from concentrating sufficiently. The latter, on the other hand, also has the following problems.

The collision velocity between dust particles in protoplanetary disks and the critical velocity for collisional growth is important for understanding their growth through sticking (Blum and Wurm, 2008). When the size of dust particles or their aggregates is less than ~10–100 μm, Brownian motion dominates the relative velocity, which is typically ≤ 1 mm s^{-1}. For larger sizes, dust particles settle towards the midplane of the disk and migrate towards the central star (Adachi et al., 1976; Weidenschilling 1977). In the minimum mass solar nebula model (Hayashi 1981), the drift motions lead to collision velocities of up to 50 m s^{-1} (e.g., Adachi et al. 1976, Weidenschilling & Cuzzi 1993). The gas turbulence is also a significant contributor of the collision velocity, which may become higher under strong gas turbulence (e.g., Ormel and Cuzzi, 2007). The question is whether they can grow at this relative velocity. The numerical experiments have examined the critical velocity for collisional growth (the upper velocity at which mass is gained by the collision) between dust aggregates (e.g., Wada et al., 2009). Water-ice is considered to have a surface energy of ~0.1 J m^{-2} at 0 °C (Israelachvili, 2011) and thus be

highly cohesive. For a collision between two aggregates with same size consisting of water-ice spheres with a radius of 0.1 μm, the critical velocity is predicted to be ~60 m s^{-1}, and so they may grow to planetesimals due to sticking each other (Wada et al., 2009). In contrast, silicate is considered to have a surface energy of 0.025 J m^{-2} at ambient condition (Kendall et al., 1987) and thus have a low cohesive force. For silicate spheres, the critical velocity is predicted to be ~6 m s^{-1}, and so they suffer the fragmentation (Wada et al., 2009). This is referred to as the "fragmentation barrier." In addition to numerical studies, laboratory studies (e.g., Güttler et al., 2010; Weidling et al., 2012; Kothe et al., 2013) have shown similar results regarding the critical velocity for the growth of silicate dust particles. In this study, we specifically address this issue.

On the other hand, the drift motion of dust particles toward the central star not only causes collisional disruption, but itself becomes an important problem. For bodies with a meter in diameter at 1 au, lifetime is shortest and estimated to be ~100 years (Weidenschilling and Cuzzi, 1993). This is called the "radial-drift barrier", and thus the collisional growth of dust particles must be completed earlier than this. Also, laboratory studies have claimed another barrier. In the process of collisional growth, repeated collisions compact the surface of the aggregates, which may lead to bouncing during a collision. Bouncing inhibits further growth, and in the case of rocky dust particles, the growth could stop at millimeters to centimeters in size. This is referred to as the "bouncing barrier" (e.g., Güttler et al., 2010). It should be noted, however, that in a numerical study aggregates do not grow dense enough to cause bouncing in protoplanetary disk environments (Wada et al., 2011), i.e., there are discrepancies between the results of a numerical study and laboratory study.

Several ideas have been proposed to overcome these barriers. In the case of water-ice dust particles, the collisional growth would be able to explain the formation of icy planetesimals (Kataoka et al., 2013). Due to its highly cohesive properties, fragmentation barrier can be ignored, and the dust particles grow into low-density dust aggregates during the process of collisional growth. This can prohibit bouncing and falling into the central star, and subsequent gas and self-gravity compressions lead to compact icy planetesimals. However, this idea cannot explain the growth of rocky dust particles. The formation of planetesimals by gravitational instability in a concentration region of dust particles induced by the interaction of dust particles and gas such as streaming instability (Youdin & Goodman 2005) has also been proposed. This process is so rapid that the radial drift is little problem, but for it to work effectively it requires decimeter-sized particles (Johansen et al. 2015) larger than millimeter- to centimeter-sized particles that are found to bounce in laboratory experiments in case of silica particles. As mentioned above, the formation

process of planetesimals, especially rocky planetesimals, remains unresolved due to the challenges resulting from their low cohesive properties. However, as discussed in more detail later, water molecules adsorbed on the surface of particles in the Earth's atmosphere may reduce the surface energy, and thus the surface energy in interplanetary space may have been underestimated (Kimura et al., 2015; Steinpilz et al., 2019; Pillich et al., 2021). In addition, the surface energy may be even higher in high temperature environment (Yamamoto et al., 2014; Kimura et al., 2015; Pillich et al., 2021). In this study we focus on the former effect by removing adsorbed water molecules.

1.1.2 Planetary ring particles

Giant planets in our solar system, such as Saturn, Uranus, and Neptune have diverse rings. Saturn's ring particles are more than 90 to 95% water ice (Cuzzi et al., 2010). The rings of Uranus and Neptune may have a large rocky component (Tiscareno et al., 2013). Planetary rings are composed of particles with various sizes, and the size distribution of Saturn's rings has been studied in detail by ground-based observations as well as by the Voyager and Cassini explorations. The size distribution is thought to be reflecting subsequent collisional accretion and fragmentation processes of particles rather than a direct ring formation event such as tidal or collisional disruption. In this respect, the picture is similar to that of dust growth in the early stage of planet formation in protoplanetary disks.

From Voyager, Cassini, and ground-based observations, the following findings have been obtained about the particle size distribution of Saturn's main rings (e.g., Zebker et al., 1985, French and Nicholson, 2000, Harbison et al., 2013). The particle size distribution has a power-law distribution of radii, r, roughly between centimeters and ten meters, $\sim r^{-q}$ ($q \sim 3$). For larger sizes, there is a steep cutoff. The abundance of smaller sizes is lower than expected from the power law distribution. To explain these observations, several studies have taken into account the effect of cohesive force of particles in processes of collisional accretion and fragmentation (e.g., Brilliantov et al., 2015, Ohtsuki et al., 2020). The cohesive force of particles is important for understanding the kinetic processes of planetary ring particles as well as protoplanetary dust particles.

1.1.3 Surface and shape evolution of small bodies

The van der Waals force may be the dominant force acting on particles of less than centimeter and less than meter size on a small body with a surface gravitational acceleration of 10^{-3} and 10^{-6} of the Earth, respectively (Scheeres et al., 2010). This suggests the interparticle cohesive force has a significant impact on the surface environment of small bodies. The cohesive force prevents the gravitational reconfiguration of particles in the particle layer on the surface of small bodies, thus maintains the porosity of the layer (Kiuchi and Nakamura, 2014). In that study, based on the experimental data on the bond number $B_o = F_v/F_g$ (where F_v is the van der Waals force between two macroscopic spheres and F_g is gravity) and porosity, the relationship between the maximum porosity and particle size on the surface of small bodies was estimated. The porosity of the surface particle layer is an important parameter that affects the thermal conductivity of the layer (Gundlach and Blum, 2013; Sakatani et al., 2016). The formation of impact craters on those layers is affected by porosity (Housen et al., 2018). Moreover, the cohesive strength of the particle layer would also affect the sampling efficiency in exploration missions (Schäfer et al., 2017).

The strength of a rubble pile, which is not a monolith but a collection of many solid particles, would determine how fast it can spin without losing mass or disintegrating. The YORP effect is known as a phenomenon that can systematically change the rotation state of asteroids (e.g., Rubincam 2000). The torque resulting from thermal radiation from the surface of a body warmed by sunlight can change the rotational period and the orientation of the rotation axis. The time scale is 10^8 years for 10-km-diameter bodies and shorter for smaller bodies. The small but non-zero cohesive strength of a small rubble pile asteroid determines the maximum rotation period at which shedding mass or disrupting can be avoided (e.g., Holsapple, 2007; Sánchez and Scheeres, 2014). In addition, the cohesive strength affects their deformation and failure modes associated with the acceleration of their rotation (e.g., Hirabayashi et al., 2015; Sánchez and Scheeres, 2016; Sugiura et al., 2021). Numerical studies based on a plastic finite element model (e.g., Hirabayashi et al., 2015) and a soft-sphere discrete element method (e.g., Sánchez and Scheeres, 2016) have examined the effect of the structure of rubble piles on the modes. Deformation along with an accelerated rotation when the structure is uniform or weak surface may result in a reshape into a top shape like asteroids Ryugu and Bennu. On the other hand, a numerical study based on a smoothed particle hydrodynamics method (Sugiura et al., 2021) discussed using the general formula for the shear strength of a powder layer, Y_d;

$$Y_d = \tan(\varphi)\, p + c, \tag{1-1}$$

where φ is the internal friction angle which depends on the particle shape, c is the cohesive strength of the powder layer, and p is the confining pressure. The effective friction angle φ_{eff}, where $Y_d = \tan(\varphi_{\text{eff}})\, p$, was introduced, and the effect of the friction angle including the effect of cohesive strength on the deformation was discussed. The top shape is formed only if the effective friction angle is 70° or greater for Ryugu, which corresponds to a cohesive strength of about 100 Pa assuming an internal friction angle of 40°. Understanding a cohesive strength of a particle layer is important for discussing the shape and surface evolution of rubble piles.

1.1.4 Mobility of particles on planetary bodies

The mobility of particles on the surface of a small body can be discussed using the gravitational force acting to the particles and the cohesive force between the particles. Assuming the van der Waals force between two macroscopic spheres, which is calculated using the Hamaker constant of lunar regolith particles and is proportional to the particle size, as the interparticle cohesive force (Perko et al., 2001, Scheeres et al., 2010), a previous study discussed the mobility of the particles on asteroid Bennu (Bierhaus et al., 2021). The total force of the gravity F_g and the van der Waals force F_{VDW} acting to a spherical particle with a radius of r on an asteroid is divided by the cross-sectional area of the particle to write in pressure unit as follows:

$$p_{\text{T}} = \frac{F_g}{\pi r^2} + \frac{F_{\text{VDW}}}{\pi r^2}. \tag{1-2}$$

Since $F_g \propto r^3$ and $F_{\text{VDW}} \propto r$, the cohesive force is dominant for smaller particles while for larger particles gravitational force is dominant, and there is a minimum pressure. The particle diameter at the minimum pressure corresponds to the size that is most easily mobilized, and on Bennu, the particle diameter was estimated to be several tens of centimeters (Bierhaus et al., 2021).

This discussion is similar to that on wind-induced dust and/or sand motions on larger bodies with atmospheres (Kok et al., 2012, Shao and Lu, 2000). Dust storms are common on Mars, and they have a significant impact on the planetary weather (Heavens et al., 2011). Topography that appears to be driven by winds, such as sand dunes and ripples, has also been observed on Venus, Titan, and Pluto, as well as Earth and Mars (Greeley et al., 1992, Lorenz et al., 2006, Telfer et al., 2018). With respect to these wind-induced activities, laboratory experiments to investigate the threshold friction velocity at

which wind-induced erosion occurs have been conducted using wind tunnels not only at the Earth's environment but also at simulated atmospheric pressure and/or gravity on Mars (e.g., Greeley and Iveysen, 1985, Kruss et al., 2020). Similar to the above discussion, the following simple expression by comparing the shear stress required to lift a particle with the sum of the gravitational force and the cohesive force proportional to particle size was proposed (Shao and Lu, 2000):

$$\rho_g u_t^{*2} = A_N \left(2\rho_p g r + \frac{\gamma}{2r} \right), \qquad (1-3)$$

where u_t^* is the threshold friction velocity and ρ_g is the atmospheric density. The first term on the right-hand side including the gravitational acceleration g is a term associated with gravitational force, the second term including the surface energy γ is a term associated with cohesive force, and A_N is a dimensionless coefficient. Thus, the cohesive force of solid particles is an essential parameter for understanding the mobility of particles both on small bodies without atmospheres and on relatively large bodies with atmosphere.

1.2 Cohesive force of solid particles

1.2.1 The Van der Waals force and pull-off force in the JKR theory

In this section, we introduce the van der Waals force and the pull-off force in the JKR theory between two macroscopic spheres, which are often used to estimate the inter-particle force.

First, we introduce the van der Waals force between two macroscopic spheres following Israelachvili (2011). As a function of the separation distance r between molecules, the van der Waals interaction energy, $w_{VDW}(r)$, is expressed by the following equation:

$$w_{VDW}(r) = -\frac{C_{VDW}}{r^6}, \qquad (1-4)$$

where C_{VDW} is the constants for the van der Waals interaction. At very small distances, the electron clouds overlap and a strong repulsion appears. There is no general formula for this repulsion, but the following empirical Lennard-Jones potential $w_{LJ}(r)$ including both attraction and repulsion, is often used:

$$w_{LJ}(r) = \frac{C_{re}}{r^{12}} - \frac{C_{VDW}}{r^6}, \qquad (1-5)$$

where C_{re} is material constants related to the repulsion between molecules.

To extend this interaction between molecules to macroscopic particles, we need to integrate the potential function over the shape of the interacting particles. Here we assume that it is simply attractive and given by Equation 1-4. First, we consider an isolated molecule at a distance D from the surface of a solid with number density ρ consisting of identical molecules, as shown in Figure 1-1a. The net interaction energy between the single molecule and the flat material is the sum of the interactions of that molecule with all the molecules in the material. Since the number of molecules within the volume of a circular ring with radius x and cross section $dxdz$ is $2\pi\rho xdxdz$, the net interaction energy is calculated as

$$w_{VDW}(D) = -2\pi C_{VDW}\rho \int_{z=D}^{z=\infty} dz \int_{x=0}^{x=\infty} \frac{xdx}{(z^2+x^2)^3} = -\frac{\pi C_{VDW}\rho}{6D^3}, \qquad (1-6)$$

Next, we consider a situation where a molecular sheet with unit surface area and thickness dz is at distance z away from a spreading surface with a larger area, as in Figure 1-1b. The interaction energy between the sheet and the surface is $-\pi C_{VDW}\rho \cdot \rho dz/6z^3$ from Equation 1-6. Thus, for the case between the two surfaces,

$$W_{VDW}(D)_{\text{planes}} = -\frac{\pi C_{VDW}\rho^2}{6} \int_D^\infty \frac{dz}{z^3} = -\frac{\pi C_{VDW}\rho^2}{12D^2}, \qquad (1-7)$$

This corresponds to the interaction per unit area between two surfaces if D is sufficiently small compared to the transverse size of the surfaces. The force per unit area between two surfaces is

$$F_{VDW}(D)_{\text{planes}} = -\frac{dW_{VDW}(D)_{\text{planes}}}{dD} = -\frac{\pi C_{VDW}\rho^2}{6D^3}. \qquad (1-8)$$

Next, we consider two macroscopic spheres (radii of R_1, $R_2 \gg D$) separated by a distance D between the surfaces. As shown in Figure 1-1c, the force $F(D)_{\text{spheres}}$ between the spheres is obtained by integrating the force between microcircular regions of area $2\pi xdx$ on both spheres separated by a distance $Z = D + z_1 + z_2$, which are assumed to be locally flat. Since only small values of Z contribute to the integral, $F(D)_{\text{spheres}}$ is written as follows:

$$F_{VDW}(D)_{\text{spheres}} = \int_{Z=D}^{Z=\infty} 2\pi x \, dx \, F(Z)_{\text{planes}}. \qquad (1-9)$$

Here, using the geometric relationship of $x^2 \sim 2R_1z_1 = 2R_2z_2$,

$$Z = D + z_1 + z_2 = D + \frac{x^2}{2R}, \qquad (1-10)$$

$$\frac{1}{R} = \frac{1}{R_1} + \frac{1}{R_2}, \qquad (1-11)$$

where R is referred to as the reduced radius. Thus, Equation 1-9 is rewritten to as follows:

$$F_{VDW}(D)_{\text{spheres}} = \int_D^\infty 2\pi R F(Z)_{\text{planes}} dZ = 2\pi R W_{VDW}(D)_{\text{planes}} = -\frac{AR}{6D^2}. \quad (1-12)$$

$$A = \pi^2 C_{VDW} \rho^2. \quad (1-13)$$

where A is referred to as the Hamaker constant. The van der Waals force between two macroscopic spheres is proportional to the reduced radius R, and inversely proportional to the square of the distance between the surfaces, D. Equation 1-12 is referred to in various fields and is often used to estimate the cohesive force of asteroidal particles as described in sections 1.1.3 and 1.1.4.

The surface energy γ of material can be calculated based on Equation 1-12 since γ is defined as $W_{VDW}(D)_{\text{planes}} = -2\gamma$. For example, using the theoretical Hamaker constant of 6.3×10^{-20} J in a vacuum or air for silica and the typical $D = 0.165$ nm (Israelachvili, 2011), we can derive 0.031 J m^{-2} for silica based on Equation 1-12. However, note that for materials with strong hydrogen bonds, the calculation leads to an underestimation, and for example using the theoretical Hamaker constant of 3.7×10^{-20} J in a vacuum or air for water and Equation 1-12 yields 0.018 J m^{-2}, which is considerably smaller than the experimental value of 0.073 J m^{-2} at 20°C (Israelachvili, 2011).
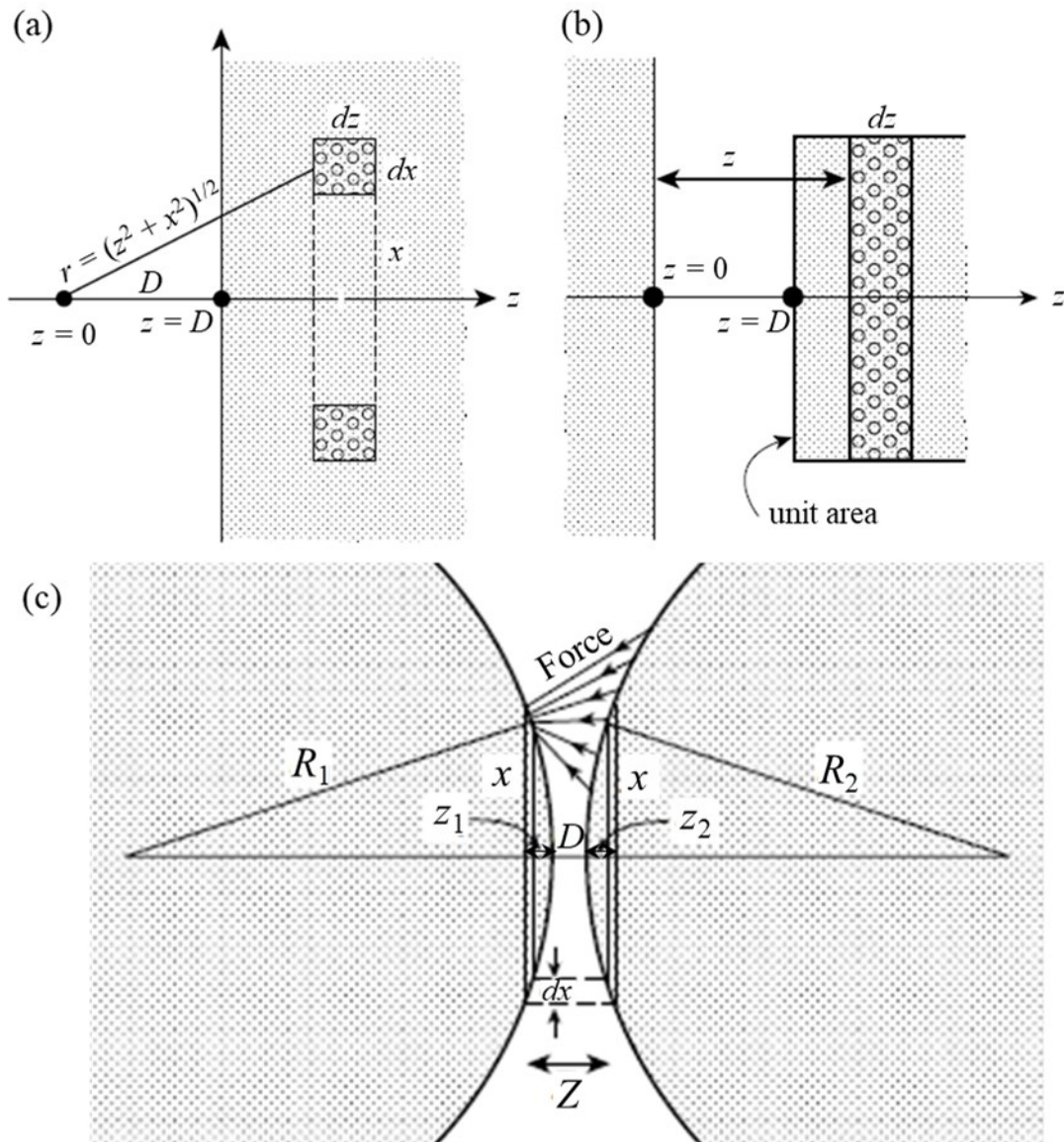
Figure 1-1 Derivation of the van der Waals force between two macroscopic spheres. (a) An isolated molecule near a flat surface. (b) Two flat surfaces. (c) Two macroscopic spheres. (a,b) and (c) are based on Figures 11.2 and 11.4 in Israelachvili (2011), respectively.

In the above, the deformation of the spheres is not considered. In the following, we introduce the pull-off force between two contacting spheres in Johnson-Kendall-Roberts (JKR) theory (Johnson et al., 1971), which is based on the Hertz theory of elastic contact (Hertz, 1896) with the consideration of cohesive forces. We consider the situation shown in Figure 1-2a, where two elastic spheres of radii R_1 and R_2, Young's modulus E_1 and E_2,

and Poisson's ratios v_1 and v_2 are in contact with an applied load F_0. The contact radius a_0 and displacement δ_0 between the two spheres when no surface force is acting are given by the Hertz theory as follows:

$$a_0{}^3 = \frac{3F_0 R}{4E^*}, \tag{1-14}$$

$$\delta_0 = \frac{a_0{}^2}{R}, \tag{1-15}$$

$$\frac{1}{E^*} = \frac{1 - v_1{}^2}{E_1} + \frac{1 - v_2{}^2}{E_2}. \tag{1-16}$$

When an attractive force acts between the surfaces, the contact radius at equilibrium increases from a_0 to a_1. The load remains at F_0, but the apparent Hertz load F_1 and displacement δ_1 corresponding to the contact radius a_1 are written as follows (condition A in Figure 1-2b,c):

$$a_1{}^3 = \frac{3F_1 R}{4E^*}, \tag{1-17}$$

$$\delta_1 = \frac{a_1{}^2}{R}. \tag{1-18}$$

The total energy U_T in this system is expressed as the sum of the elastic energy U_E, the mechanical energy U_M due to a load, and the binding energy between the surfaces U_S:

$$U_T = U_E + U_M + U_S. \tag{1-19}$$

Next, we consider the respective energies. The total elastic energy of the system ignoring surface forces, is expressed as the amount of energy U_1, required to reach condition A in Figure 1-2b,c (load of F_1, displacement of δ_1, contact radius of a_1), minus the amount of energy U_2, required to reach condition B (load of F_0, displacement of δ_2, contact radius of a_1):

$$U_E = U_1 - U_2. \tag{1-20}$$

U_1 is given as follows:

$$U_1 = \int_0^{\delta_1} F d\delta = \int_0^{F_1} \frac{1}{2} \left(\frac{4}{3}\right)^{1/3} \frac{F^{2/3}}{E^{*2/3} R^{1/3}} dF = \frac{3}{10} \left(\frac{4}{3}\right)^{1/3} \frac{F_1{}^{5/3}}{E^{*2/3} R^{1/3}}. \tag{1-21}$$

The change of the displacement from condition A to condition B with a constant contact radius can be achieved by the addition of a pressure distribution resulting in a uniform displacement within the contact surface to the Hertz pressure distribution. Under the added pressure distribution the relationship between a load and a displacement is given as $F = 2E^* a_1 (\delta - \delta_1) - F_1$, thus U_2 is given as follows:

$$U_2 = \int_{\delta_2}^{\delta_1} F d\delta = \int_{F_0}^{F_1} \frac{F}{2E^* a_1} dF = \frac{1}{4} \left(\frac{4}{3}\right)^{1/3} \frac{1}{E^{*2/3} R^{1/3}} \left(\frac{F_1{}^2 - F_0{}^2}{F_1{}^{1/3}}\right). \tag{1-22}$$

14

The mechanical potential energy U_M due to the applied load F_0 is given as follows:

$$U_M = -F_0 \delta_2 = -F_0 \left(\delta_1 - \frac{F_1 - F_0}{2E^* a_1} \right)$$

$$= -\frac{3}{4} \left(\frac{4}{3} \right)^{1/3} \frac{F_0}{E^{*2/3} R^{1/3}} \left(\frac{1}{3} F_1^{2/3} + \frac{2}{3} F_0 F_1^{-1/3} \right). \qquad (1-23)$$

The binding energy U_S due to cohesive force is given as follows:

$$U_S = -2\gamma \pi a_1^2 = -2\gamma \pi \left(\frac{3RF_1}{4E^*} \right)^{\frac{2}{3}}, \qquad (1-24)$$

where γ is the surface energy per unit area of the surfaces.

From Equations 1-19–24, the equilibrium condition of $dU_T/da_1 = dU_T/dF_1 = 0$ gives the following formula:

$$F_1 = F_0 + 6\pi\gamma R + \sqrt{12\pi\gamma R F_0 + (6\pi\gamma R)^2}, \qquad (1-25)$$

Thus, the contact radius considering the effect of surface energy can be written as follows:

$$a^3 = \frac{3R}{4E^*} \left\{ F + 6\pi\gamma R + \sqrt{12\pi\gamma R F + (6\pi\gamma R)^2} \right\}. \qquad (1-26)$$

This is equal to Equation 1-14 when $\gamma = 0$. In order to obtain a real solution to Equation 1-26, the following condition is needed:

$$12\pi\gamma R F \leq (6\pi\gamma R)^2 \qquad (1-27)$$

Thus, the separation of the two spheres occurs at the following conditions:

$$F_{JKR} = 3\pi\gamma R. \qquad (1-28)$$

This is the pull-off force required to separate the two contacting spheres in the JKR theory. It is proportional to the reduced radius, R, as well as the van der Waals force between two macroscopic spheres as expressed in Equation 1-12.

The critical kinetic energy required to separate two contacting spheres based on the JKR theory, E_{break}, is obtained by totaling the U_T at equilibrium and when the two spheres separate as follows (Chokshi et al., 1993, Dominik and Tielens, 1997, Wada et al., 2009, Wada et al., 2013):

$$E_{break} \sim 37 \frac{\gamma^{5/3} R^{4/3}}{E^{*2/3}}. \qquad (1-29)$$

The dust growth in protoplanetary disks and the accretion and disruption processes of planetary rings, as described in sections 1.1.1 and 1.1.2, have been discussed in terms of the critical energy, or the surface energy γ.
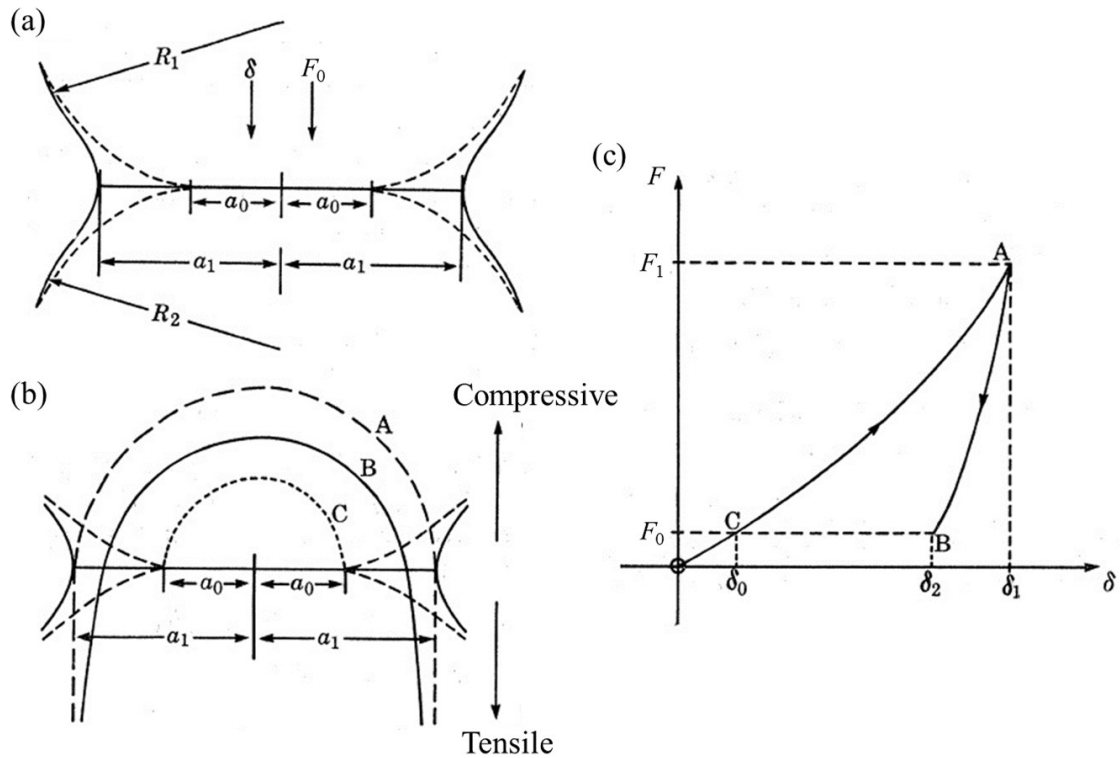
Figure 1-2 Contact between two elastic spheres. (a) Solid and dashed lines show the contact with (contact radius a_1) and without surface force (contact radius a_0) under load F_0, respectively. (b) The distribution of stress. Condition A is the Hertz stress at $a = a_1$ and $F = F_1$. Condition B is the actual stress at $a = a_1$ and $F = F_0$. Condition C is the Hertz stress at $a = a_0$ and $F = F_0$. (c) Relationship of load and displacement. These are based on Figure 1 in Johnson et al. (1971).

1.2.2 Measurements of cohesive force

Laboratory studies on the cohesive force of solid particles in planetary science have been carried out mainly using the following methods.

A cantilever method is used to directly measure the cohesive force. The cohesive force between spherical silica SiO_2 particles with radius of 0.5–2.5 μm at conditions of room temperature, pressure of 10^2–10^5 Pa, and humidity of 10–40% were measured using atomic force microscope (AFM) cantilevers (Heim et al., 1999). Two particles were bonded to the microscope slide and the edge of the AFM cantilever with epoxy respectively. The particles are brought into contact with each other and then separated. The force required for the separation is measured based on the deflection of the cantilever

16

and its spring constant. The results of the measurements show that the cohesive force of micron-sized silica spheres increases in proportion to the particle size and is consistent with the van der Waals force between two macroscopic spheres in Equation 1-12 and the pull-off force of the JKR theory in Equation 1-28. A similar but much larger scale approach has been used to measure the force between a 10 mm square plate of a carbonaceous chondrite and ~3 mm diameter pins, consisting of serpentine, olivine, bronzite, siderite, and Fe-Ni, when the pins were pressed and pulled against the plate (Kleinhenz et al., 2017). The results of the measurements suggest the possibility that cohesive force varies with minerals. However, due to the small number of measurements, it is not possible to draw any conclusions about material dependence.

The tensile strength of an aggregate consisting of particulates sticking to each other may reflect the inter-particle cohesive force. Measurements of tensile strength were performed on cylindrical aggregates with diameters and heights ranging from millimeters to centimeters, consisting of micron-sized silica spheres, water ice particles, organic particles, mixtures of two types of water ice particles, silica spheres, and fly ash particles, mixtures of quartz and iron particles, and fragments of an ordinary chondrite (Gundlach et al., 2018, Steinpilz et al., 2019, Bischoff et al., 2020, Haack et al., 2020, Kruss and Wurm, 2020, Bogdan et al., 2020, Pillich et al., 2021). The Brazilian test was performed on the aggregates, and the tensile strength σ_B is calculated from the following equation:

$$\sigma_B = \frac{2F_t}{\pi d_c L}, \qquad\qquad (1-30)$$

where F_t is the maximum load, d_c is the sample diameter, and L is the sample length. On the other hand, the equation of tensile strength of a powder layer often used in the field of powder engineering (Rumpf 1970) is

$$\sigma_R = \frac{9\varphi N}{8\pi d^2}F, \qquad\qquad (1-31)$$

where σ_R is the tensile strength in this equation, φ is the packing fraction, N is the coordination number, d is the particle diameter. F is the interparticle cohesive force, which might be obtained by considering $\sigma_B = \sigma_R$ (Bogdan et al., 2020, Pillich et al., 2021).

The third is the centrifugal method, which is the experimental method used in this study. This is a method used in the field of powder engineering. A centrifugal force is applied to a plate to which particles are attached, and the cohesive force is measured based on the centrifugal force with which the particles leave the plate (e.g., Krupp 1967, Nagaashi et al., 2018). This technique is described in detail in Section 2.4.

1.2.3 Effect of water molecule adsorption

Gas molecules adsorb on the surface of solid particles. In the Earth's atmosphere, the adsorption of water molecules in particular can have a significant effect on cohesive force. The adsorption of gas molecules can be mainly classified into chemisorption and physisorption (Thiel and Madey, 1987, Hibbitts et al., 2011). Due to partial covalent bonding, a monolayer of water molecules can exist stably on the surface even under ultra-high vacuum ($<10^{-8}$ torr, or $\sim 10^{-6}$ Pa). This is generally referred to as chemisorption. Water molecules can also adsorb through the van der Waals force, which is much weaker than covalent bonds. This is generally referred to as physisorption. The operation used to remove the adsorbed terrestrial water molecules from sample particles is usually heating of the sample. Most of terrestrial water molecules adsorbed on lunar soil samples is desorbed at a temperature of 200 °C or less, but occasionally is not be desorbed even at about 500 °C (Epstein and Taylor, 1974). Thermal desorption experiments on lunar regolith simulants or analogs have shown that there is a strong compositional dependence of water adsorption by lunar materials (Hibbitts et al., 2011). The results show that lunar basalt glass analog is hydrophobic, while basalt lunar mare simulant and highland analog, albite, exhibit chemisorption of water. Especially some chemisorbed water of albite remain until ~450 K.

The effect of removal of adsorbed water molecules by heating on cohesive force of particles has been investigated for amorphous silica. The surface energy values of amorphous silica have been obtained using various techniques at ambient and heating conditions (Kimura et al., 2015). Figure 1-3 shows the values obtained by laboratory experiments at ambient and heating (< 400 °C) conditions. Figure 1-3 also shows a theoretical value of 0.031 J m^{-2} as described in section 1.2.1 (Israelachvili, 2011). At higher temperature (> 400 °C) conditions, greater surface energies of amorphous silica have been measured (Kimura et al., 2015), which may be important for dust growth very close to a central star (< 0.1 au; Pillich et al., 2021), however this is not addressed in this study. At the ambient condition multi-layered water molecules may be present, while at the heated condition (< 400 °C) monolayered water molecules or silanol groups may be present, which may correspond to a vacuum condition (Kimura et al., 2015). In Figure 1-3, even at ambient condition, there is a range of several times the surface energy. Comparing the values obtained by the same technique in the same study between ambient and heating conditions (1–5 in Figure 1-3), the values are larger in the heating conditions, increasing from a little to seven times. On the other hand, tensile strength measurements of aggregates consisting of micron-sized amorphous silica spheres as described in section

1.2.2 when heated at 250 °C for 24 hours (Steinpilz et al., 2019) led to an increase of the strength by up to 10 times, which was attributed to an increase of the surface energy. Tensile strength measurements of aggregates consisting of ordinary chondrite fragments have shown similar results at similar conditions (Pillich et al., 2021).

In direct shear strength tests conducted on several soil samples assuming the lunar soil, it has been confirmed that at heated (125–350 °C) and ultra-high vacuum (down to 10^{-10}–10^{-9} torr, or ~10^{-8}–10^{-7} Pa) the cohesion increases by a factor of two to three for sand and silica and decrease for olivine (Vey and Nelson, 1965, Bromwell 1966, Nelson and Vey, 1968). The increase is also thought to be due to the increase in interparticle forces caused by the removal of adsorbed gas molecules. The increase was explained by the introduction of surface cleanliness $S = \Omega/t$, where Ω is radius of mineral molecules, as a parameter to quantify the thickness of adsorbed gas, t, on soil particles determined by the balance of intermolecular potential energy and condensation energy (Perko et al., 2001). In this model, as shown in Figure 1-4, the distance between particle surfaces in the van der Waals force between two macroscopic spheres in Equation 1-12, D, is replaced by $2t$,

$$F_{\text{VDW}} = \frac{AR}{24t^2} = \frac{AS^2R}{24\Omega^2},\qquad(1-32)$$

The S ranges from 1 with no adsorbate to nearly 0 for a saturated surface. The removal of adsorbate between the particles results in an increase in the van der Waals force.
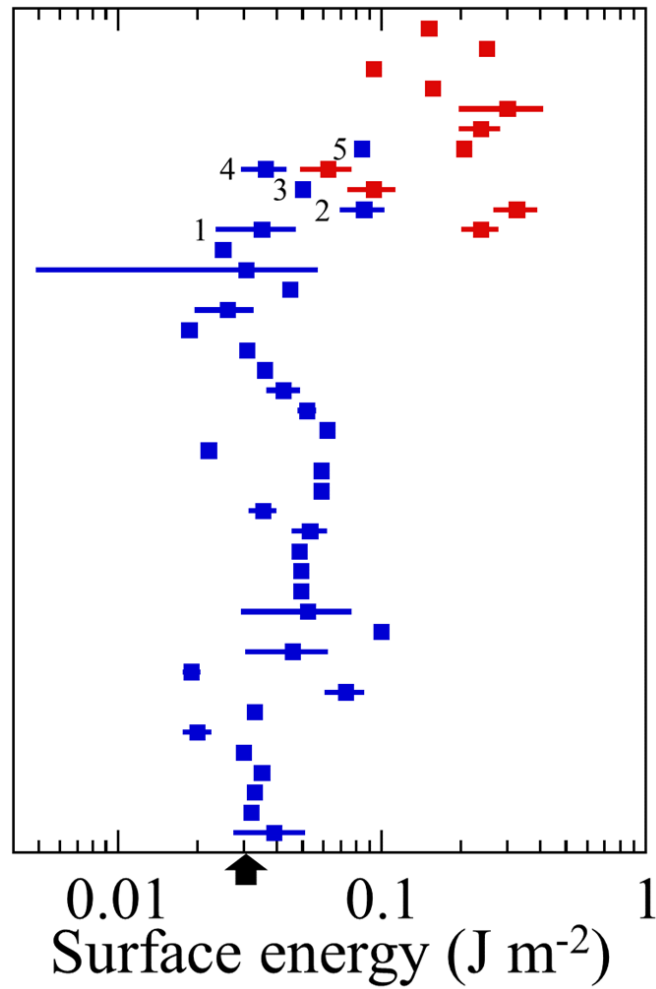
Figure 1-3 Surface energies of experimentally obtained amorphous silica in different conditions. Blue denotes the values at ambient condition, and red denotes the values at heating (< 400 °C) conditions. Arrow indicates the theoretical surface energy of silica in a vacuum or air, as described in section 1.2.1 (Israelachvili, 2011). This is based on Figure 1 in Kimura et al. (2015).
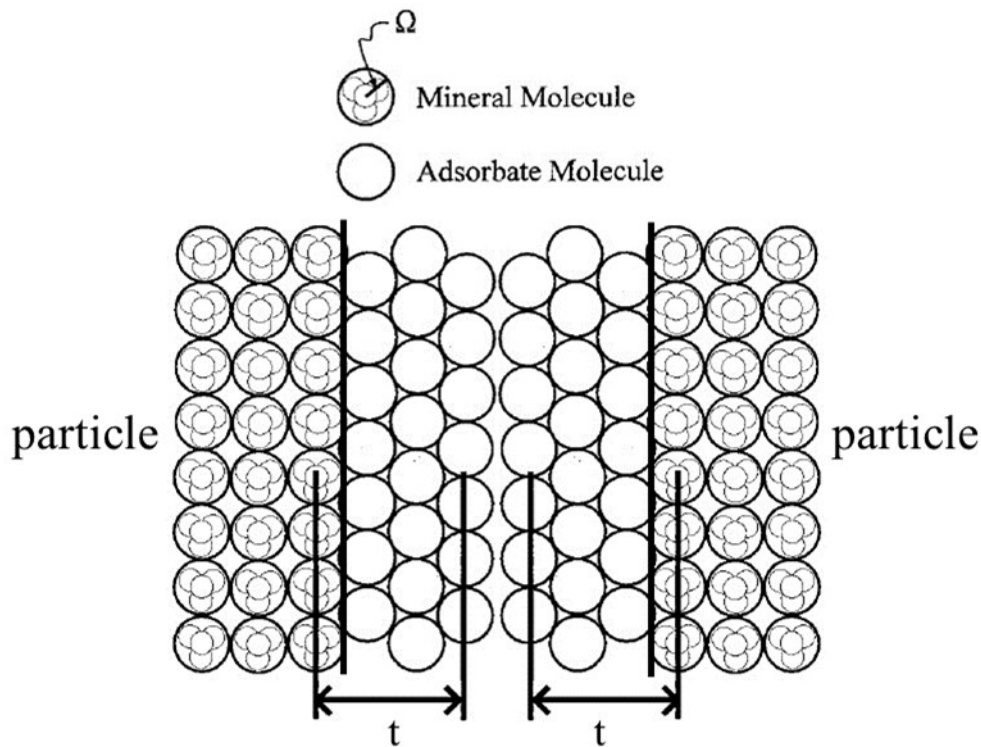
Figure 1-4 Adsorbate thickness between two surfaces. This is based on Figure 2 in Perko et al. (2001).

1.3 Scope of this work

The cohesive forces of asteroidal particles are often estimated based on measurements of micron-sized silica spheres and theoretical formula assuming perfect spheres, whose cohesive force increases in proportion to the particle size. However, even for spherical particles with tens of microns in size, the cohesive forces measured by atomic force microscope cantilevers (LaMarche et al., 2017) and the centrifugal method (Nagaashi et al., 2018) are orders of magnitude smaller than the estimation. In addition, rubble piles are thought to be the results of the re-accumulation of fragments from the collisional disruption of the parent body (Michel et al., 2001). The constituent particles are the re-accumulated fragments and subsequently crushed fragments due to impacts (Housen et al., 1979) or thermal fatigue (Delbo et al., 2014), resulting in irregularly shaped particles. Although the cohesive force of asteroidal particles is often discussed assuming that it is similar to that of the lunar regolith particle, a comparison of lunar

regolith particles with particles recovered from asteroid Itokawa reveals that the former are abraded and more rounded (Tsuchiyama et al., 2011). Moreover, the size dependence and the effect of the removal of adsorbed water molecules on the cohesive force of the asreroidal particles are still unclear.

In this work, to address issues related to the effect of shape and size of particle and water molecule adsorption on the cohesive forces, the cohesive forces of tens of micron-sized or micron-sized meteorite fragments and tens of micron-sized aggregates consisting of submicron-sized amorphous silica spheres were investigated. First, as indicators to characterize particle shape the axial ratio, circularity, and arithmetic mean roughness of the particles were measured, and then the cohesive force was measured using a centrifugal method. Furthermore, the amount of water molecules adsorbed on the particles was measured, and then the cohesive force was measured when the particles were heated or evacuated to remove the water molecules. Based on the results, the mobility of the particles on the surface of asteroids was discussed. The application to the growth process of silicate dust particles in protoplanetary disks and the strength of rubble pile asteroids was also described.

Chapter 2

Experiments

Parts of this chapter have been published as Nagaashi, Y., Aoki, T., Nakamura, A. M., 2021, Icarus, 360, 114357, and will be published as Nagaashi, Y. and Nakamura, A. M. (in prep.).

2.1 Preparation of particles

We used three carbonaceous chondrite samples, Tagish Lake (C2-ung), Murchison (CM2), and Allende (CV3), three ordinary chondrite samples, Northwest Africa (NWA) 539 (LL3.5), NWA 1794 (LL5), and NWA 542 (LL6), and a eucrite sample, Millbillillie. Carbonaceous and ordinary chondrites are composed of particles including chondrules and fine-grained (generally <5 μm) matrix silicate-rich particles whose abundance and grain size vary with meteorites, whereas eucrites are basalts (Weisberg et al., 2006). Tagish Lake has experienced aqueous alteration and does not belong to any specific group but is mineralogically and chemically similar to the CI and CM groups (Brown et al., 2000).

We prepared meteorite powders of several tens of microns. For the Allende meteorite, we also prepared powders of several microns. We crushed the pieces of the meteorites using an agate mortar and pestle, and used sieves to roughly eliminate particles with sizes larger than 75 μm and smaller than 25 μm for the samples with several tens of microns, and larger than 16 μm and smaller than 5 μm for the samples with several microns (hereinafter referred to as "small"). In addition, for Allende and Tagish Lake meteorites, ejecta fragments from projectile impacts on the pieces were collected as samples. The impacts were carried out at low velocities of 0.129–0.136 km s^{-1} at ambient pressure using a He gas-gun installed at Kobe University and at high velocities of 2.85–2.92 km s^{-1} at a reduced pressure (a few Pa) using a two-stage hydrogen-gas gun installed at Institute of Space and Astronautical Science. The projectiles were 1/8-inch stainless steel spheres for the former and 1 mm aluminum spheres for the latter. The experimental conditions are shown in Table 2-1. The ejecta fragments were recovered inside acrylic containers. The size of the particles was between 25 and 75 μm in the same way as the ground particles.

We used several tens of micron-sized polydispersed spherical glass beads, irregularly shaped glass powder (Fujikihan Co., Ltd.), and silica sand (Miyazaki Chemical Co., Ltd.) particles. The distributions of the equivalent circular diameter of the samples measured on the images acquired by attaching a digital camera to an optical microscope are shown in Figure 2-1. The size distributions of particles acquired by the images were consistent with those determined by a confocal laser refractometer (Nagaashi et al., 2018). The median diameters and particle densities of the samples are summarized in Table 2-2.

As a sample with a known surface structure, we used aggregates of polydisperse silica spheres (Admatechs Co., Ltd.) with a density of 2.26 g cm^{-3} (manufacturer's information). The cumulative number fraction of diameters of 186 spheres measured in scanning electron microscope (SEM) images is shown in Figure 2-1. The diameters are in the range of 0.1–1 μm with a median of 0.44 μm. By sieving them, it is possible to prepare aggregates of the mesh size or smaller (e.g., Weidling et al., 2012, Kothe et al., 2013). We prepared the aggregates using a sieve with a mesh size of 106 μm, and the aggregates of several tens of microns were picked up for the measurements.

The SEM images of the samples are shown in Figure 2-2. The meteorite fragments seem to have rougher surfaces and rounder shapes than the glass powder or silica sand particles. Tagish Lake samples have much finer surface structures than Allende samples, whether crushed by a mortar and pestle or by impacts.

Density measurements were performed on meteorite samples (Murchison, Allende, NWA 1794, and Millbillillie) using a helium gas pycnometer (AccuPyc II 1340). The measured densities of Murchison, Allende, and Millbillillie samples, 2.94, 3.56, and 3.25 g cm^{-3}, respectively, are consistent with the grain densities of these meteorites measured in previous studies using helium ideal-gas pycnometry, which were 2.96, 3.66, and 3.2 g cm^{-3}, respectively (Macke et al., 2011a; Macke et al., 2011b). The measured density of NWA 1794, 3.45 g cm^{-3}, is within the grain density range of LL chondrites, which is 3.54±0.13 g cm^{-3} (Consolmagno et al., 2008). According to the literature, Tagish Lake has a grain density of 2.72 g cm^{-3} (Hildebrand et al., 2006). The bulk porosities of hand-sized samples of Murchison, Allende, Tagish Lake, and Millbillillie can vary over a wide range with their average values standing at 22%, 22%, 40%, and 11%, respectively (Hildebrand et al., 2006, Macke et al., 2011a, Macke et al., 2011b), whereas the porosity of LL chondrites is approximately 10% (Consolmagno et al., 2008). The bulk density of meteorite fragments is probably smaller than their grain density; however, it could be larger than that of hand-sized samples, depending on the type of the meteorite and the size of the void spaces (Consolmagno et al., 2008). We refer to the literature value of

grain density of Tagish Lake and the measured density of Murchison, Allende, and Millbillillie, as well as to that of NWA 1794 for the densities of NWA 539 and NWA 542 samples, as the upper limit of the particle density hereinafter. We assume the bulk density of 0.84 g cm^{-3} for the aggregates according to sub-mm to mm-sized silica sphere aggregates studied previously (Weidling et al., 2012, Kothe et al., 2013).

Table 2-1 Experimental conditions of projectile impacts on meteorite pieces.

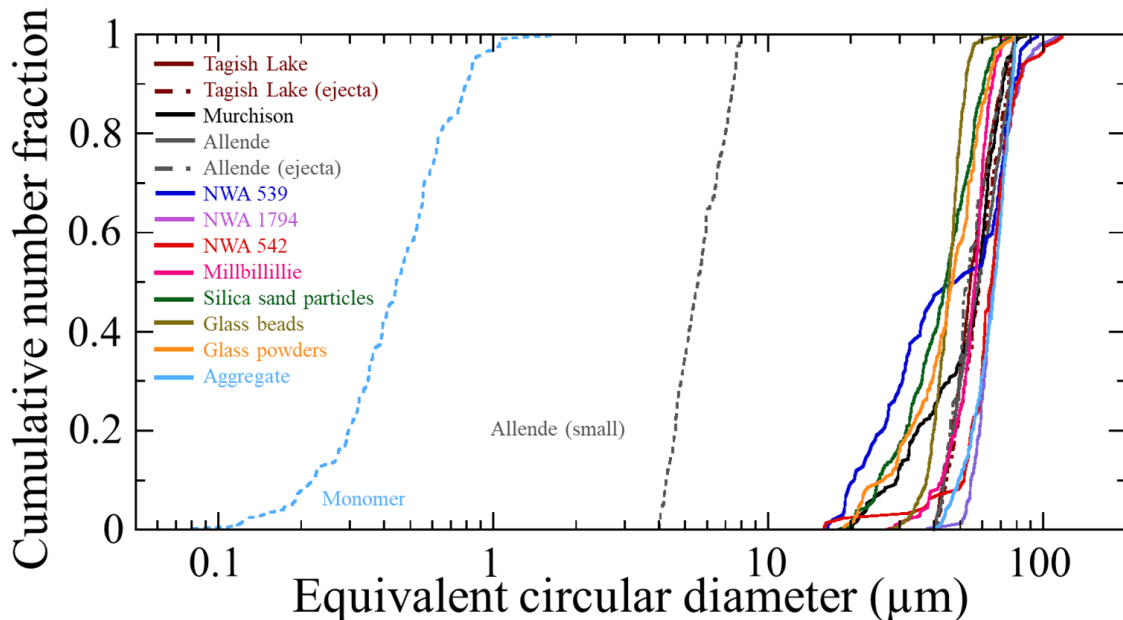| Target		Projectile			Atmospheric
Material	Mass (g)	Material	Diameter (mm)	Impact velocity (km s^{-1})	pressure (Pa)
Allende (CV3)	21.216	Aluminum	1	2.92	1.5
	21.087			2.85	2.0
	20.381			0.129	
Tagish Lake (C2-ung)	0.031	Stainless steel	3.2	0.133	10^5
	0.026			0.136	

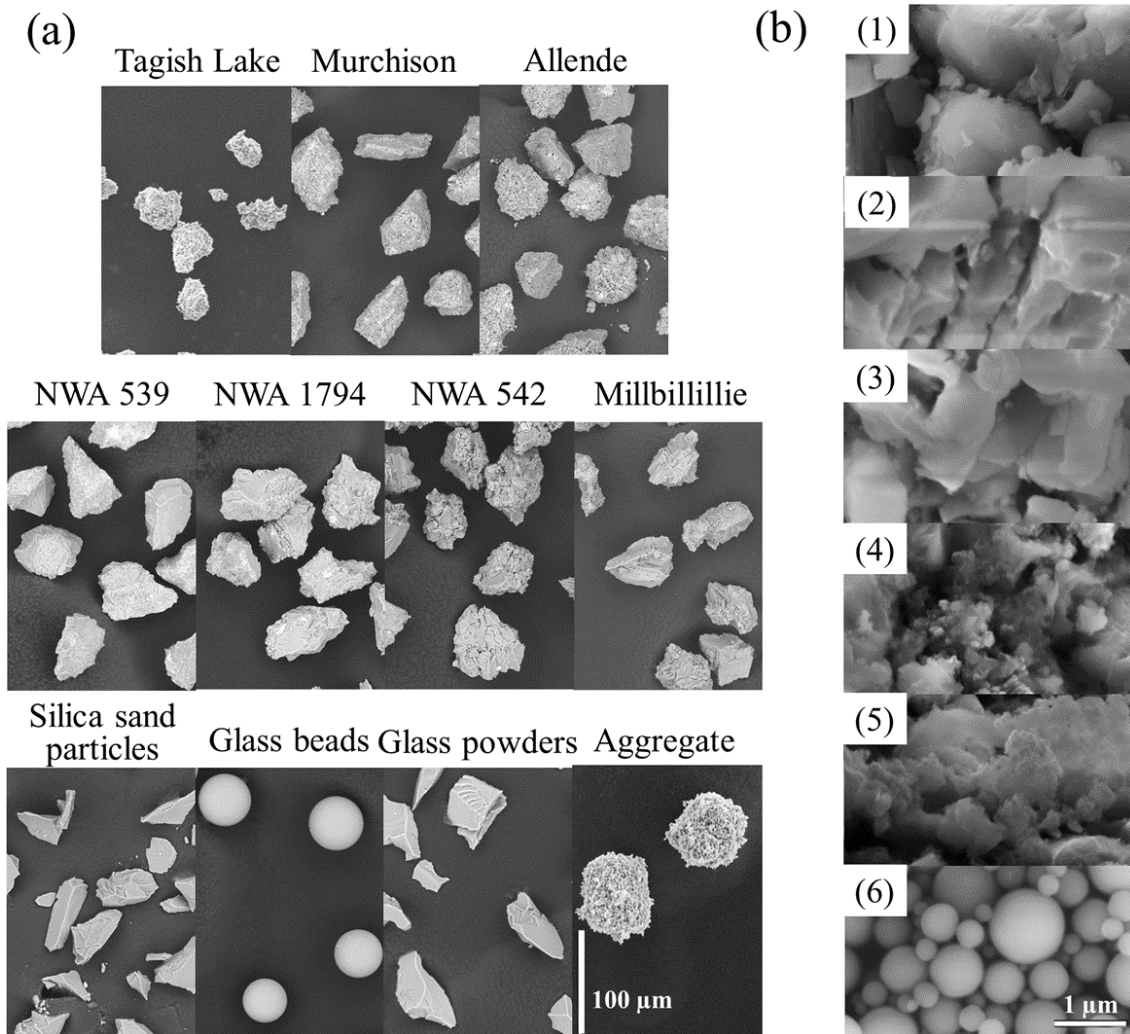**Figure 2-1 Particle size distributions.**

Figure 2-2 Scanning electron microscopy (SEM) images. (a) Images of Tagish Lake meteorite, Murchison meteorite (CM2), Allende meteorite (CV3), NWA 539 (LL3.5), NWA 1794 (LL5), NWA 542 (LL6), Millbillillie (eucrite), silica sand particles, glass beads, glass powders, and aggregates of amorphous silica spheres. (b) Enlarged images. (1) A ground fragment of Allende. (2) An ejecta fragment by low-velocity impact of Allende. (3) An ejecta fragment by high-velocity impact of Allende. (4) A ground fragment of Tagish Lake. (5) An ejecta fragment by low-velocity impact of Tagish Lake. (6) An aggregate of amorphous silica spheres.

Table 2-2 Median diameter and density of the particles.

	Median diameter (μm)	Density (kg m^{-3})
Tagish Lake (C2-ung)	54	2720
Tagish Lake (ejecta)	59	
Murchison (CM2)	58	2942
Murchison (large)	570	
Allende (CV3)	58	
Allende (ejecta)	53	3564
Allende (small)	5.6	
NWA 539 (LL3.5)	48	3453
NWA 1794 (LL5)	65	3453
NWA 542 (LL6)	65	3453
Millbillillie (eucrite)	57	3251
Silica sand particles	44	2645
Silica sand particles (large)	450	
Glass beads	46	2500
Glass powders	47	2500
Glass powders (large)	1100	
Silica sphere aggregate	67	840
Silica sphere monomer	0.44	2260

2.2 Shape measurements of particles

We obtained the axial ratio and circularity of the particles from the optical microscope images of the samples with spatial resolution of 1.3 or 0.66 μm pixel^{-1} using ImageJ software (Schneider et al., 2012). We obtained the axial ratio $A_x = b/a$, the ratio of the minor axis b to the major axis a length when the two-dimensional projection of the particle is approximated as an ellipse. We obtained the circularity $C = 4\pi S/L^2$ where S is the projection area and L is its perimeter. To establish the empirical relationship between the size and the mass of irregularly shaped particles, we prepared another set of Murchison and glass powder samples with particle sizes of 570 μm and 1100 μm, respectively (referred to as "large" in Table 2-2), which are larger than those of the samples prepared for measuring the cohesive force. We measured the projected areas and long axes of the individual particles and the total masses of 553 Murchison particles and 101 glass powders. We also measured the axial ratio of 450 μm silica sand particles (referred to as "large" in Table 2-2).

A confocal laser scanning microscope (LEXT OLS3100) was used to obtain particle-wide surface profiles for one or two particles of the samples with horizontal and vertical resolutions of 0.125 μm and 0.01 μm, respectively. We also measured the surface profile of the smooth glass slide used for measuring the cohesive force. We randomly extracted two to three line scans from each surface profile and calculated the arithmetic mean roughness, R_a, for each scan (Appendix A).

2.3 Measurements of the amount of water molecule adsorption on particles

2.3.1 Water vapor adsorption isotherm

We used a high-precision gas and vapor physisorption instrument (BELSORP-max II) to estimate the amount of adsorbed water molecules at the ambient pressure at which the cohesive force measurement was taken. The constant volume method was adopted, in which a change in the gas pressure in the container between before and after gas adsorption on the particles was detected. The amount of gas molecules is estimated

based on the equation of state of ideal gas, whereby the amount adsorbed on the particles is determined. Before conducting the measurement, vessels containing sub-cm^3 samples were evacuated at 150 °C, which is a nominal pretreatment for silica to expose the surface (e.g., Tarasevich, 2007), for 6 h. The amount of adsorption was measured as the relative pressure, which is the ratio of the equilibrium pressure of adsorption to the saturated vapor pressure, was changed. The measurements were conducted on the Allende and NWA 1794 samples.

2.3.2 Thermogravimetry and differential thermal analysis

We measured the cohesive force after the samples were heated to remove adsorbed water molecules on the particle surfaces as well as at ambient condition. Meteorites can be altered by heating. Therefore, we conducted a simultaneous thermal analysis using ThermoGravimetry/Differential Thermal Analyzer (TG-DTA) (Rigaku Thermo plus EVO). Allende and Tagish Lake samples of 13.9 and 15.7 mg, respectively, in a platinum container and an empty container as reference were heated simultaneously in air at a temperature increase rate 5 °C min^{-1} up to 300 °C and 10 °C min^{-1} up to 600 °C. By simultaneously measuring the change in mass of the sample and the change in temperature difference from the reference (probing presence of exothermic or endothermic reaction), the presence or absence of material change at each temperature can be evaluated. Based on the results, we determined the heating temperature for Allende and Tagish Lake to remove the adsorbed water molecules and avoid alteration.

2.4 Cohesive force measurements of particles

In this study, we used a centrifugal method (Krupp 1967; Lam and Newton, 1991; Salazar-Banda et al., 2007; Nagaashi et al., 2018) to measure the cohesive force between a particle and a circular optical glass of 20 mm in diameter, 26 mm × 35 mm rectangular smooth slide glass, or circular smooth stainless steel plate of 8 mm in diameter (hereinafter referred to as "slide"). Using this method, we can directly, simultaneously, and statistically measure the cohesive forces of irregularly shaped particles of a limited number such as meteorite fragments.

All measurements started with the particles deposited on the slide at open air of a relative humidity of 25–50%, although for some samples, particles were subsequently evacuated (~10 or 10^{-3} Pa) and/or heated to remove the adsorbed water molecules. The heating conditions were determined as described in the previous section 2.3.2. A schematic measurement configuration of the cohesive force at the reduced pressure is shown in Figure 2-3a. The volume enclosed by a mini-vacuum chamber with a valve and a glass slide to which particles were attached was evacuated at room or elevated temperature. We closed the valve and maintained a vacuum during the cohesive force measurement. Heating was conducted using a hot plate as shown in Figure 2-3b. The heating temperature of the particles was calibrated by measuring the surface temperature of the same glass slide at the same temperature setting of the hot plate using a digital thermometer based on a K thermocouple sensor in a separate experiment.

We took the optical microscope images of the particles on the slide, as shown in Figure 2-3c. Next, the slide was placed in a centrifuge, and a centrifugal force was applied to the slide in a direction that the particles were pulled off vertically. The slide was then gently removed from the centrifuge. The optical microscope images were taken from the same location from where the images were taken before the application of the centrifugal force, as shown in Figure 2-3c. The slide was once again placed in the centrifuge and a larger centrifugal force was applied to it. The procedure was repeated as the centrifugal acceleration β was increased in 7–10 steps. We used tabletop centrifuges (Kubota KN-70 and himac CT15E) to apply β of ~10–3 × 10^3 g_E and 20–7 × 10^3 g_E (g_E is the acceleration of the Earth's gravity) to the particles, respectively. For evacuated or heated measurements, a pair of the entire mini-vacuum chambers with valves were placed in the former centrifuge, and microscope images were taken from outside the chamber using the mini-vacuum chamber jig we have developed as shown in Figure 2-3d. We used a floor-standing micro ultracentrifuge (himac CS150FNX) to apply β of ~10^3–6 × 10^5 g_E to the particles. We only used stainless steel slides because the large acceleration leads to fragmentations of glass slides.

If a particle is small and its gravity is small compared to the cohesive force, the particle may stick unsteadily where it comes in contact with a slide. Thus, using the pressing technique of particles onto a slide by centrifugal force prior to cohesive force measurements (Lam and Newton, 1991), we also measured the cohesive force after pressing small Allende against slides with a centrifugal acceleration of approximately 8 × 10^4 g_E. However, press-on may also cause a plastic deformation of the surface asperities of particles (Lam and Newton, 1991). In order to evaluate the effect of plastic deformation,

we also measured the cohesive force after pressing Murchison fragments against slides with a centrifugal acceleration of approximately 5×10^3 g_{E}.

The mass M of each particle used to calculate the centrifugal force was estimated using the a-axis length of each particle measured by the optical microscope images and particle density listed in Table 2-2, as described in section 2.2. The cohesive force between the particle and the slide was then obtained as the geometric mean of the two subsequent centrifugal forces applied to the particle $M\sqrt{\beta_i\beta_{i+1}}$ ($\beta_i < \beta_{i+1}$) where β_i is the maximum centrifugal acceleration at which the particle remained on the slide, and β_{i+1} is the centrifugal acceleration at which the particle no longer remained on the slide.

The number of particles of the meteorite samples and other samples measured in this study were in the ranges of 59–296 and 145–349, respectively. During a previous study by the authors, a significant fraction of the particles remained on the slide even at the maximum permitted centrifugal acceleration, thus their cohesive force could not be determined (Nagaashi et al., 2018). In this study, however, we were able to measure the cohesive force of at least 88% of the particles of each type of sample. Table 3-3 shows the measured number and fraction of the particles.
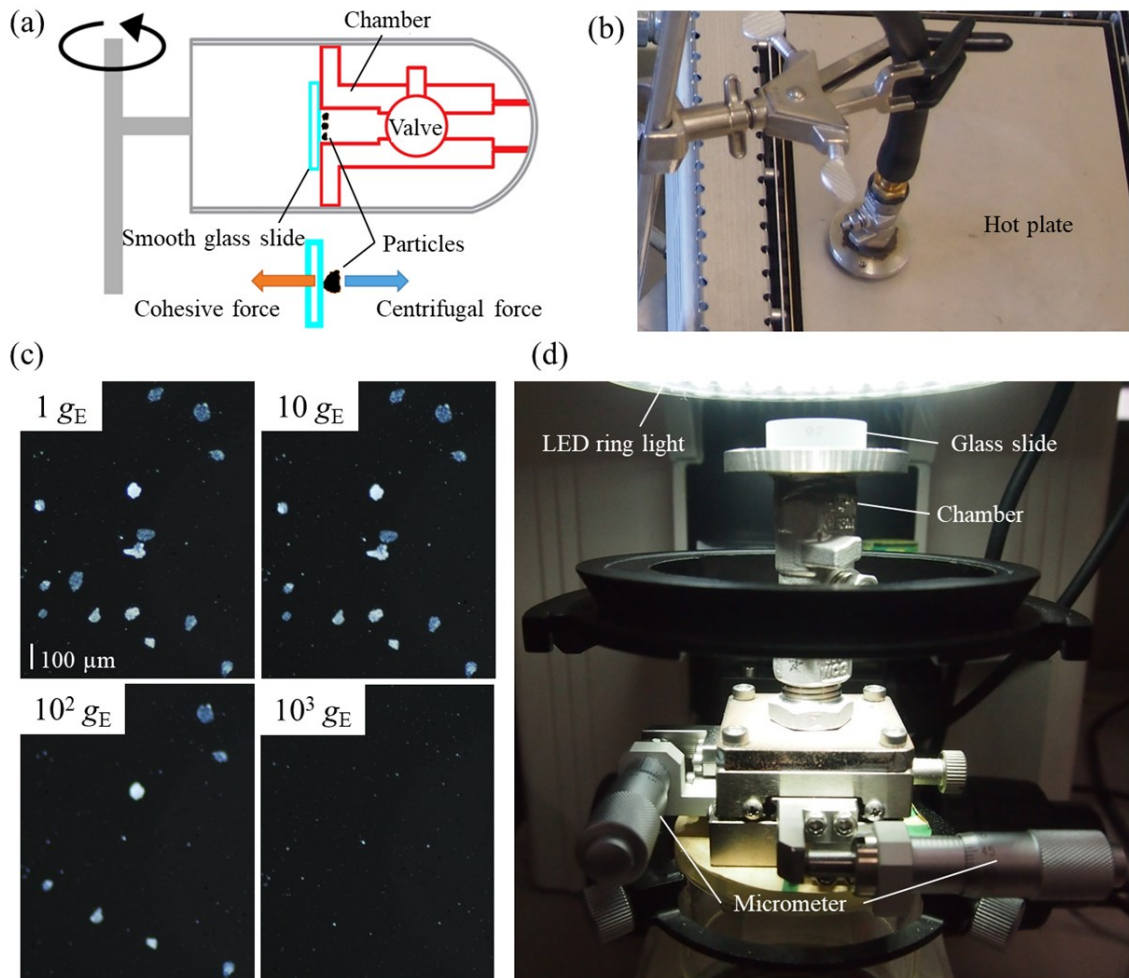
Figure 2-3 Configuration of cohesive force measurements under reduced pressure.
(a) Schematic diagram of an application of a centrifugal force under reduced pressure. The cohesive force of particles can be measured under reduced pressure in a space enclosed by a glass slide and a mini-vacuum chamber with a valve. (b) Heating of particles. Heating is performed by placing the glass slide with particles in contact with a hot plate. (c) The optical microscope images of Allende fragments after heated (250 °C) and evacuated ($\sim 10^{-3}$ Pa) for 48 hours on the slide before and after applying centrifugal accelerations of 10, 10^2, and 10^3 g_E. Scale bar is 100 μm. (d) Configuration of optical microscope image acquisition. Micrometers are used to adjust the glass slide for acquiring images of the same location. The use of an LED ring light allows for the imaging of particles attached to the inner surface of the glass slide.

Chapter 3

Results

Parts of this chapter have been published as Nagaashi, Y., Aoki, T., Nakamura, A. M., 2021, Icarus, 360, 114357, and will be published as Nagaashi, Y. and Nakamura, A. M. (in prep.).

3.1 Shape of particles

The cumulative percentages of the axial ratio and circularity of the two-dimensional projection of each type of particle are shown in Figure 3-1. Because circularity depends on the spatial resolution of the image, we compared the circularity measured at a spatial resolution at which the two-dimensional projected area of the particle corresponds to 10^3–5×10^3 pixels. Table 3-1 presents the average, standard deviation, and median of the axial ratio and circularity of the particles. Because particles are likely to settle on the glass slide with the *c*-axis approximately perpendicular to the slide, the projected axial ratio of the particles may be considered as *b/a*, a zeroth-order approximation. The axial ratios of meteorite fragments, including the ejecta fragments, ranged from 0.71–0.76 on average. This is similar to the *b/a* for basalt impact fragments (~0.73; Fujiwara et al., 1978); Itokawa particles (0.71 ± 0.13; Tsuchiyama et al., 2011); and Itokawa, Eros, and Ryugu boulders (~0.68, 0.71–0.73, and ~0.68, respectively; Michikami et al., 2010, 2018, 2019). The axial ratios of the small glass powders and silica sand were lower, with averages of 0.58 and 0.64, respectively. The axis ratios for the glass beads and aggregates were higher, with averages of 0.97 and 0.79, respectively. The circularity of meteorite fragments, including ejecta fragments, and aggregates ranged from 0.73–0.78 on average. The circularity for the small glass powder and silica sand particles were lower, with averages of 0.69 and 0.72, respectively. The circularity for the glass beads was higher, with averages of 0.90.

The smaller glass powder particles and silica sand particles had smaller axial ratios and circularities than those of the other particles used in this experiment, including the larger glass powder and silica sand particles used for the total mass measurement, although in an ideal ellipse, circularity decreases as the axial ratio (*b/a*) decreases. The smaller axial ratio and circularity of the smaller glass powder and silica sand particles

may be due to the difference in the positions of the particles, i.e., the larger and smaller particles have similar shapes, but the *c*-axis of the smaller particles is not perpendicular to the glass slide. The glass powder and silica sand particles seem to be composed of flat surfaces, as can be seen in Figure 2-2. Thus, when they are small and the cohesive force is relatively large, the particles are more likely to settle on the surface of the glass slide with a non-perpendicular *c*-axis orientation. Alternatively, this may be due to a difference in the shape of differently sized particles, i.e., smaller particles do have shorter intermediate axis and less circularity in projected shape.

The two-dimensional projected image of a particle may correspond to its cross section through the long and intermediate axes of an ellipsoid with an axial ratio typical to impact fragments (Fujiwara et al., 1978). The mass M of the particle was estimated in a previous study (Nagaashi et al., 2018) using the following equation:

$$M = 0.45\rho S^{3/2}, \tag{3 − 1}$$

where S and ρ are the projected area and particle density, respectively. The total $\rho S^{3/2}$ of the 553 large Murchison (CM2) and the 101 large glass powder particles were $\sum \rho S^{3/2} = 8.2 \times 10^{-5}$ kg and 1.1×10^{-4} kg, respectively. We assumed the measured (grain) density of the large Murchison for ρ. However, the total M of the 553 large Murchison particles and the 101 large glass powder particles were $\sum M = 7.7 \times 10^{-5}$ kg and 5.6×10^{-5} kg, respectively. The results suggest that the estimation made on the basis of an ellipsoidal (with $a{:}b{:}c = 2{:}\sqrt{2}{:}1$) assumption overestimates the masses of the glass powder particles by a factor of ~2. In contrast, the ellipsoidal assumption predicts the masses of the meteorite particles, which are 1.1 times the measured masses. If we assume that the bulk density of Murchison is 2.31 g cm^{-3}, as given in the literature (Macke et al., 2011b), the $\sum \rho S^{3/2}$ of the large Murchison particles is 6.4×10^{-5} kg. The estimation based on the ellipsoidal assumption is 0.83 times the measured mass.

The *c*-axis of a small-sized particle may significantly incline from the line of sight. To avoid this possible effect on the projected area, we estimated the mass of the particles using the long diameter of the projected plane, the *a*-axis, rather than the projected area *S*, although the assumption of the previous study (Nagaashi et al., 2018) may produce an appropriate estimation for meteorite fragments. We estimated the mass of small particles using the following equation:

$$M = \pi/6\,\rho a^3 \text{ (glass beads)}, \tag{3 − 2a}$$
$$M = 0.08\rho a^3 \text{(glass powders)}, \tag{3 − 2b}$$
$$M = 0.12\rho a^3 \text{ (meteorite particles)}, \tag{3 − 2c}$$
$$M = 0.09\rho a^3 \text{ (silica sands)}, \tag{3 − 2d}$$
$$M = 0.19\rho a^3 \text{ (aggregates)}. \tag{3 − 2e}$$

Here, the value for glass beads is based on an assumption for an ideal sphere whose diameter is the length of the *a*-axis. For meteorite particles and glass powders, we assumed that the large particles measured their mass and the small particles measured their cohesive force had similar axial ratios. We used $\sum \rho a^3 = 6.2 \times 10^{-4}$ kg and 7.1×10^{-4} kg and $\sum M = 7.7 \times 10^{-5}$ kg and 5.6×10^{-5} kg for the 553 large Murchison particles and the 101 large glass powder particles to obtain $\sum M / \sum \rho a^3 = 0.12$ and 0.08, respectively. Based on these values, we obtained an empirical relationship between axial ratio A_x and the factor, and assumed the factors of 0.09 and 0.19 for the silica sand particles ($A_x \sim 0.64$) and the aggregates ($A_x \sim 0.79$), respectively (Appendix B).

The surface morphologies of the particles of each sample obtained using a confocal laser scanning microscope are depicted in Figure 3-2a, and their one-dimensional profiles extracted along a line perpendicular to the line of sight are depicted in Figure 3-2b. The surface roughness of the glass slide, characterized using the arithmetic mean roughness R_a (Appendix A), is 3–4 nm. The surface asperity of the stainless steel slide is a few nm (manufacturer's information). The R_a values for meteorite fragments and aggregates are submicron while for non-meteorite particles except for aggregates are tens of nanometers. Whereas the other particles and the slides are different in R_a by orders of magnitude, the differences among meteorites and aggregates were not significant. Table 3-2 summarizes the mean value and standard deviation of R_a for each particle type.
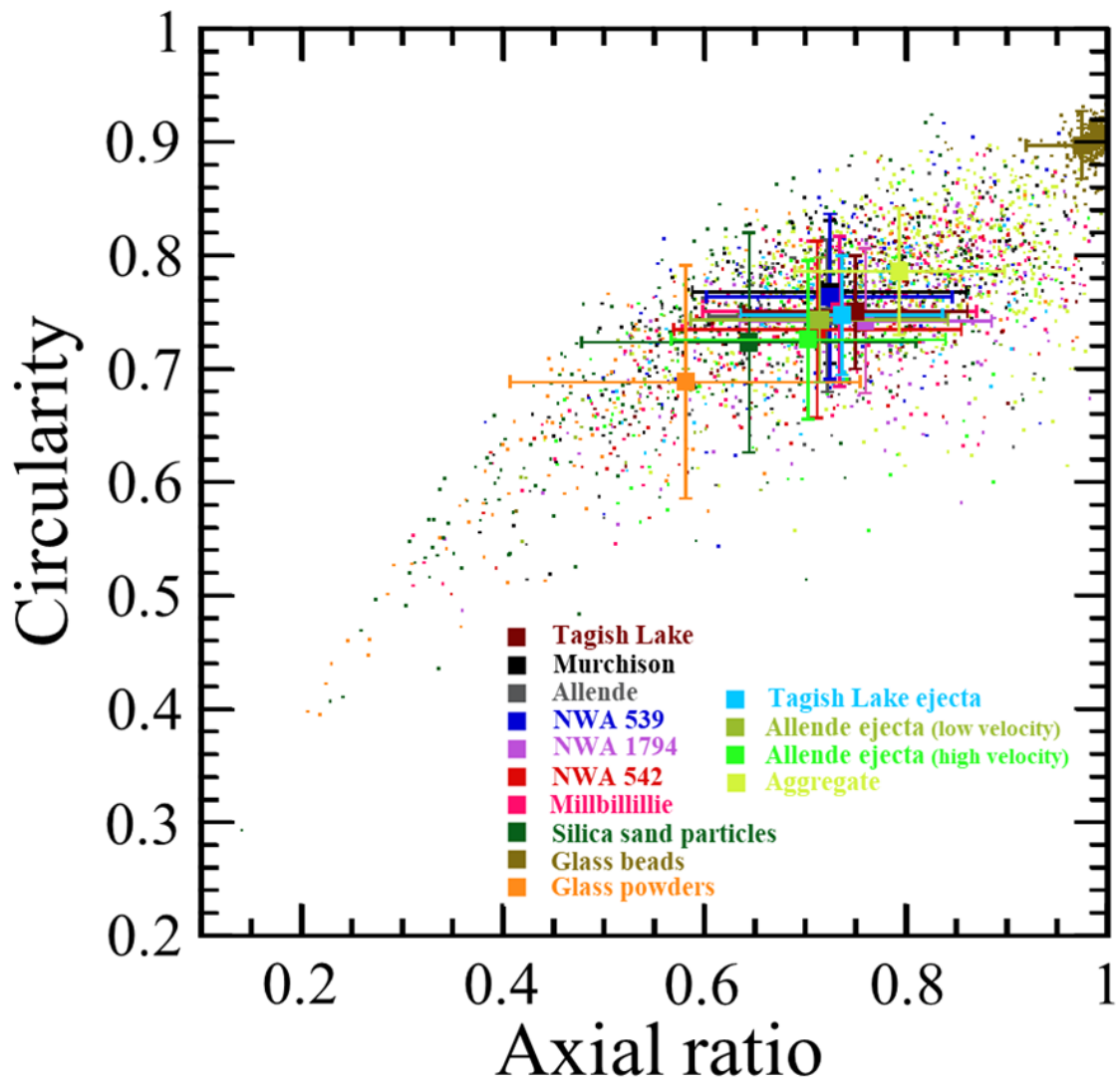
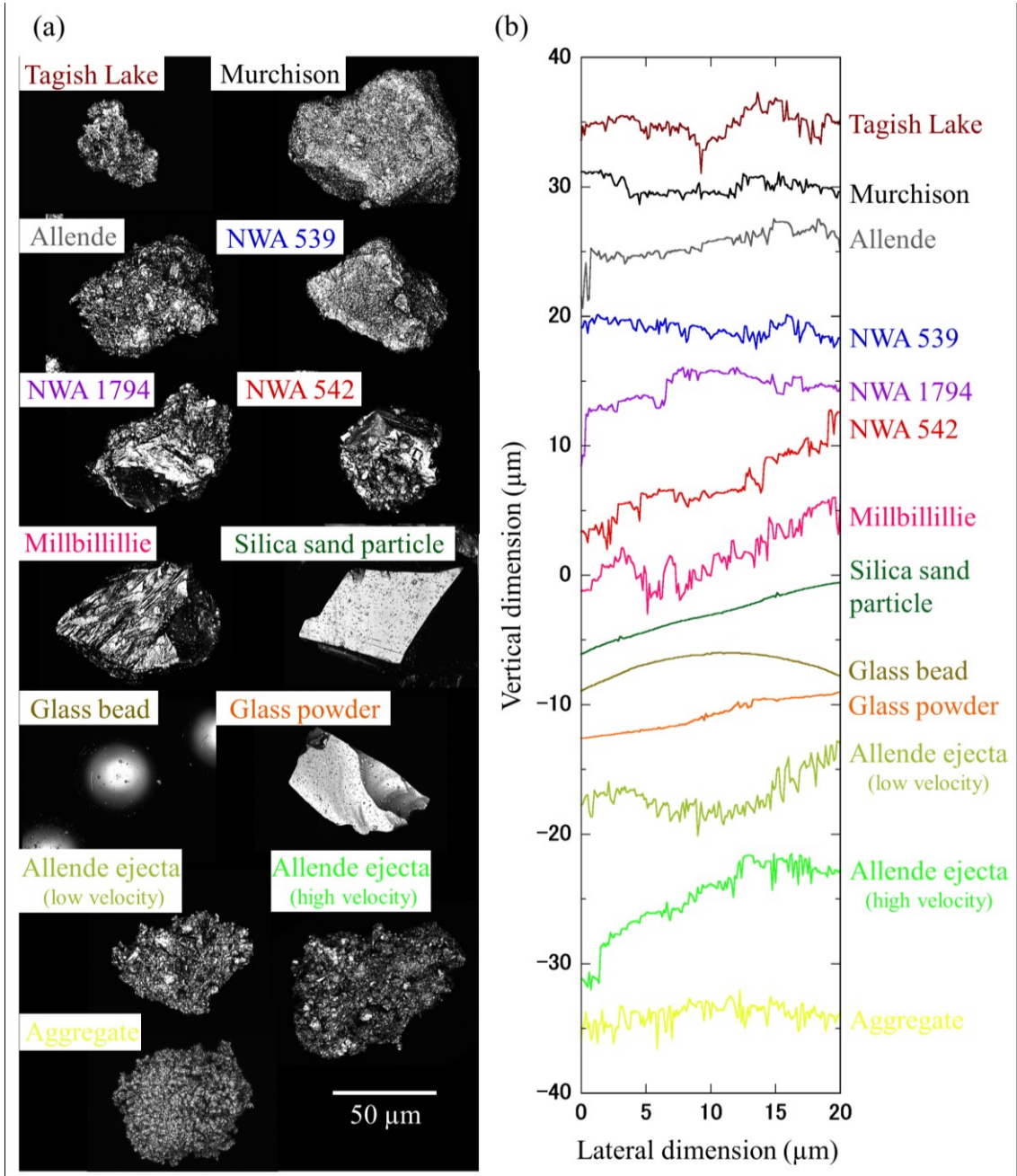**Figure 3-1 Axial ratio and circularity of the particles.**

Figure 3-2 Microscopic morphology of the particle. (a) Surface morphologies of each type of sample particle acquired via confocal laser scanning microscopy and (b) the one-dimensional profile extracted from the data. The horizontal axis shows the location along a line perpendicular to the line of sight, while the vertical axis shows the height.

Table 3-1 Axial ratio and circularity of sample particles

	Axial ratio			Circularity		
	Average	Standard deviation	Median	Average	Standard deviation	Median
Tagish Lake (C2-ung)	0.75	0.11	0.76	0.77	0.05	0.77
Allende (CV3)	0.71	0.13	0.72	0.73	0.07	0.75
Murchison (CM2)	0.72	0.14	0.74	0.77	0.06	0.78
NWA539 (LL5)	0.72	0.12	0.73	0.76	0.07	0.77
NWA1794 (LL5)	0.76	0.12	0.78	0.74	0.06	0.76
NWA542 (LL6)	0.71	0.14	0.73	0.74	0.08	0.74
Millbillillie (eucrite)	0.73	0.14	0.74	0.75	0.07	0.76
Tagish Lake (ejecta)	0.73	0.1	0.73	0.78	0.06	0.79
Allende ejecta (low velocity)	0.71	0.13	0.73	0.77	0.06	0.77
Allende ejecta (high velocity)	0.71	0.14	0.72	0.74	0.08	0.75
Silica sand particles	0.64	0.17	0.67	0.72	0.1	0.74
Glass beads	0.97	0.06	0.99	0.9	0.03	0.9
Glass powders	0.58	0.17	0.58	0.69	0.1	0.7
Silica sphere aggregate	0.79	0.09	0.8	0.73	0.06	0.74
Murchison (large)	0.72	0.13	0.73	0.75	0.07	0.76
Glass powder (large)	0.73	0.12	0.75	0.75	0.07	0.76
Silica sand particles (large)	0.7	0.14	0.71	-	-	-

Table 3-2 R_a values of the samples and the glass slide

	Average (nm)	Standard deviation (nm)
Tagish Lake (C2-ung)	570	170
Allende (CV3)	360	100
Murchison (CM2)	270	30
NWA 539 (LL3.5)	290	50
NMA 1794 (LL5)	360	80
NWA 542 (LL6)	380	120
Millbillillie (eucrite)	390	40
Allende ejecta (low velocity)	460	60
Allende ejecta (high velocity)	380	70
Silica sand particles	25	10
Glass beads	24	8
Glass powder	32	13
Rectangular glass slide	3.9	0.1
Circular glass slide	2.7	0.1
Silica sphere aggregate	550	40

3.2 The amount of water molecule adsorption on particles

The water vapor adsorption isotherms of Allende and NWA 1794 measured using a high-precision gas and vapor physisorption instrument described in section 2.3.1 are depicted in Figure 3-3a. The curves agree with the general adsorption isotherms, such as Type II and IV of the adsorption isotherm classification (Sing et al., 1985). The initial bending of the curve as the relative pressure of the water vapor is increased indicates that the surface of the particles is completely covered with a monolayer, and that multilayer adsorption has begun. In this study, the amount of water vapor adsorbed by the time the monolayer was completely formed was determined based on the excess surface work theory (Adolphs and Setzer, 1996), which is a descriptive theory of adsorption isotherms based on thermodynamics. In this theory, the ratio of the change in the chemical potential of water vapor during the isothermal adsorption, $\Delta\mu$, to its change in the chemical potential at the beginning of adsorption $\Delta\mu_0$ can be written using the volume of water vapor adsorption per gram of sample particles at each relative pressure of water vapor,

n_{ads}, and the volume of water vapor required to completely cover the surface of one gram of sample particles with a monolayer, n_{mono}, as indicated below.

$$\frac{\Delta\mu}{\Delta\mu_0} = \exp\left(-\frac{n_{ads}}{n_{mono}}\right). \qquad (3-3)$$

The chemical potential is expressed as $\Delta\mu = RT\ln(p/p_s)$, where R is the gas constant, T is the temperature, p is the partial water vapor pressure, and p_s is the saturated water vapor pressure. Equation 3-3 can be transformed as follows:

$$n_{ads} = -n_{mono}\ln\left|\ln\left(\frac{p}{p_s}\right)\right| + n_{mono}\ln\left|\frac{\Delta\mu_0}{RT}\right|. \qquad (3-4)$$

The obtained water vapor adsorption isotherms (Figure 3-3a) with the natural logarithm of the absolute value of the natural logarithm of relative pressure plotted on the horizontal axis is shown in Figure 3-3b. According to Equation 3-4, the slope of the fitting curve of the plot is $-n_{mono}$. We refrained from using the data for $p/p_s > 0.6$ for fitting because the nature of adsorption for $p/p_s < 0.6$ and $p/p_s > 0.6$ in Figure 3-3a will be different (Sing et al., 1985). Accordingly, the estimated numbers of particles on the surface, n_{mono}, were 0.58–0.59 cm^3 g^{-1} and 1.23–1.25 cm^3 g^{-1} for Allende and NWA 1794, respectively. From Figure 3-3a, the amounts of adsorbed water vapor in the Allende and NWA 1794 particles at a relative humidity in the range of 30%–40%, $n_{ads(p/p_s=0.3-0.4)}$, are estimated to be 1.11–1.31 cm^3 g^{-1} and 2.71–3.04 cm^3 g^{-1}, respectively. Because the $n_{ads(p/p_s=0.3-0.4)}/n_{mono}$ of the Allende and NWA 1794 particles are 1.9–2.3 and 2.2–2.5, respectively, approximately two water-molecule adsorption layers were estimated to be formed on the surface of the Allende and NWA 1794 particles during the measurements of the cohesive forces of the particles.

The rate of weight change of Allende and Tagish Lake samples measured using a TG-DTA described in section 2.3.2 are depicted in Figure 3-4. As the temperature increased, Allende started to lose mass, reached a minimum mass at 200–300 °C, and then started to gain mass and generated a heat above 400 °C. The initial mass loss would be the removal of adsorbed water molecules, and the lost mass was 0.02 mg. The lost mass corresponds to a volume of ~0.025 cm^3 for water molecules assuming an ideal gas. For each gram of the sample, this is 1.8 cm^3, which is similar to the amount of adsorbed water vapor at humidity of ~60% from Figure 3-3a. The subsequent increase in mass may have been due to oxidation of the sample, as seen in heating of lunar regolith (Dąbrowski et al., 2008). By contrast, Tagish Lake exhibited an endothermic reaction at approximately 60 °C and lost tens of times more mass than Allende before reached at 300 °C. Then, at temperatures above 400 °C, it began to lose more mass along with endotherming. The former mass loss may have included not only removal of adsorbed

water molecules but also dehydration of interlayer water as seen in heating of saponite (Gilmour et al., 2019). The latter mass loss may have corresponded to hydroxy release from layer silicates and CO_2 release from carbonates at 400 °C or more (Gilmour et al., 2019). To avoid the effects of oxidation and thermal decomposition, the heating of the meteorite fragments for cohesive force measurements was limited to below 400 °C. However, it should be noted that dehydration of interlayer water may occur for Tagish Lake at 60 °C and more. We did not conduct TG-DTA for aggregates consisting of silica spheres, but we heated them at 350 °C for 24 hours for cohesive force measurement. This is the same duration and higher temperature comparing with a previous study, which investigated the effect of adsorbed water molecules on tensile strength of aggregates consisting of silica spheres (Steinpilz et al., 2019).
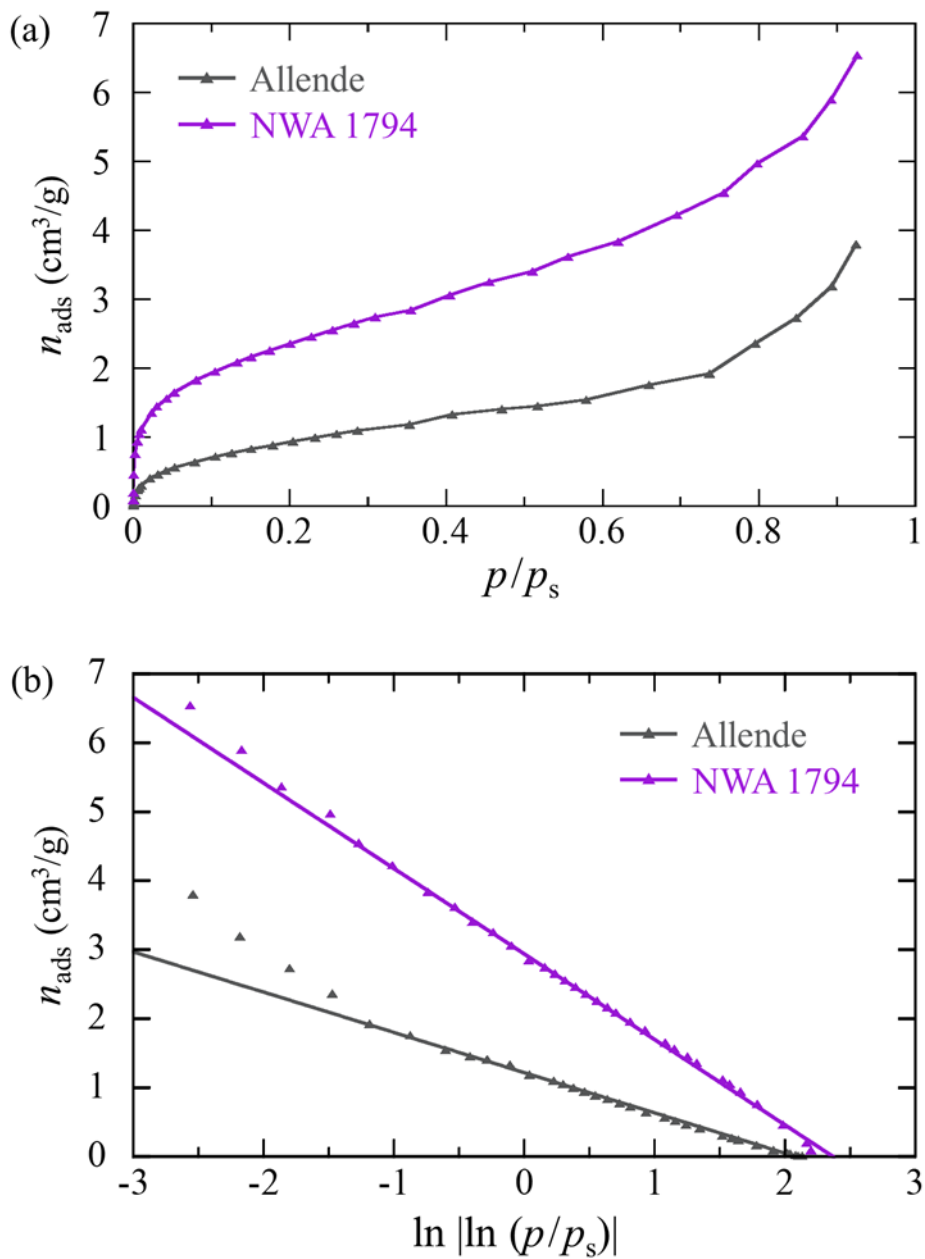
Figure 3-3 Amount of water vapor adsorption onto particle surfaces. (a) Water vapor adsorption isotherms. (b) Plotted (a) on the horizontal axis as the natural logarithm of the absolute value of the natural logarithm of relative pressure. The slopes of the solid fitting lines represent $-n_{mono}$.
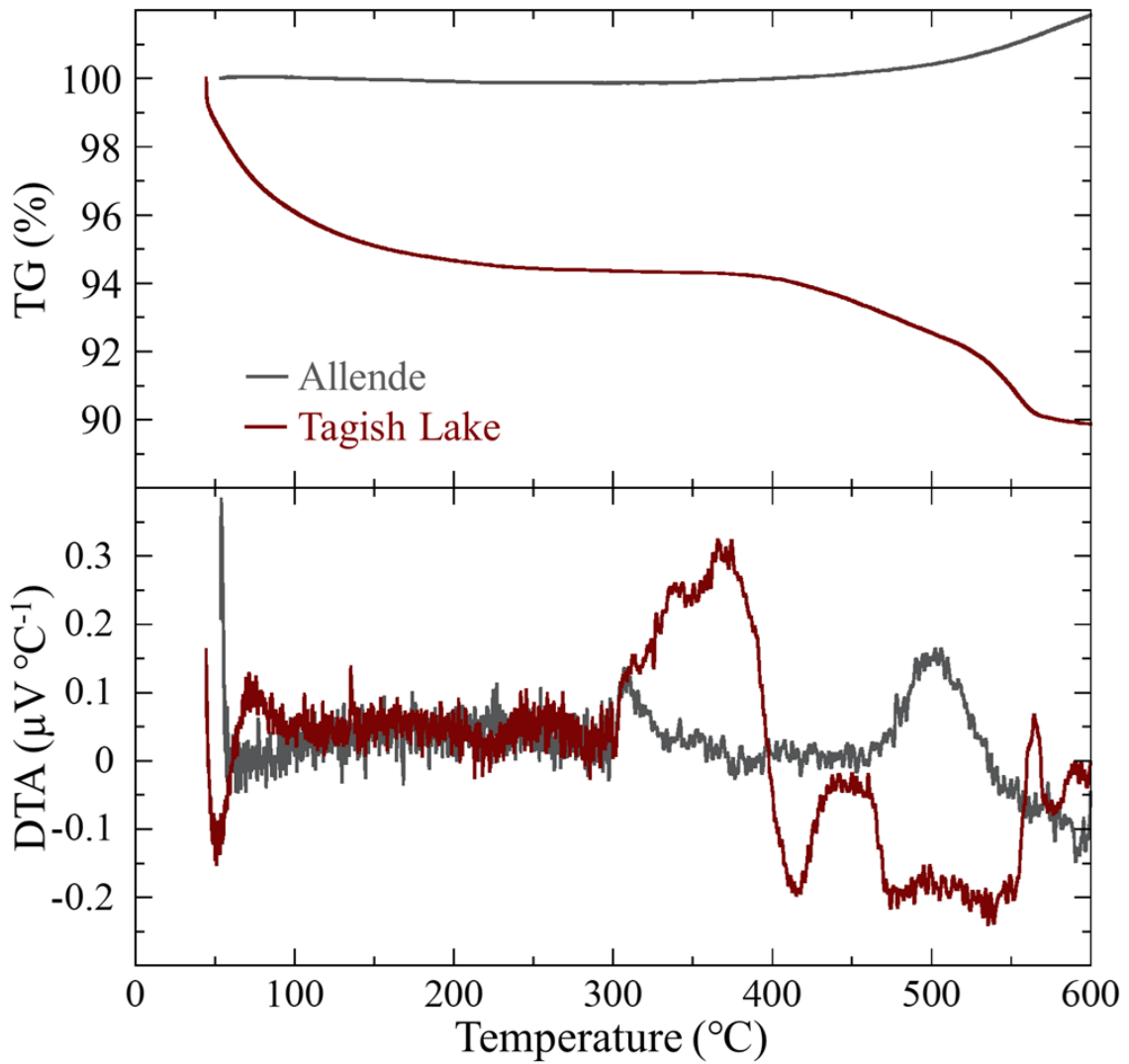
Figure 3-4 TG-DTA of Allende and Tagish Lake. Top is the change from the original mass. Bottom is the change in the temperature derivative of the differential heat signal, where the upward change represents heat generation and the downward change represents heat absorption.

3.3 Cohesive force of particles

3.3.1 Cohesive force at ambient condition

Figure 3-5 shows the cumulative number fractions of the measured cohesive force against a glass slide at ambient temperature and pressure. For comparison, a model distribution of cohesive forces, based on the JKR theory (Johnson et al., 1971), is also shown in Figure 3-5. Here, the model distributions are those expected by the theory in the case of silica spheres with a size distribution of carbonaceous chondrite particles. As the size distribution for the model, a synthesized distribution composed of all the Murchison and Allende particles was used in this study. In the estimation of force required to separate a sphere and a plate in contact in the JKR theory, expressed in Equation 1-28, we used the surface energy of silica particles γ = 0.025 J m^{-2}, which was obtained through a measurement in the atmosphere (Kendall et al., 1987), for both the particles and glass slide. In the calculation of the model cohesive forces, we used the equivalent circular radius as the radius R of each particle. The particle masses were estimated using Equations 3-2a–e and the particle densities listed in Table 2-2.

The cumulative number fraction, f, of the cohesive force measurements, F_{meas} are fitted by a Weibull distribution using three parameters as indicated below:

$$f_{F_{\mathrm{meas}}}(< F_{\mathrm{meas}}) = 1 - \exp\left\{-\left(\frac{F_{\mathrm{meas}} - F_{\mathrm{meas0}}}{\overline{F_{\mathrm{meas}}}}\right)^{\phi_{F_{\mathrm{meas}}}}\right\}, \qquad (3-5)$$

where $\overline{F_{\mathrm{meas}}}$ is a typical F_{meas}, $\phi_{F_{\mathrm{meas}}}$ is a parameter that characterizes the width of the distribution, and F_{meas0} is a threshold parameter and here set to the minimum value of the measurements. The values obtained for each parameter are summarized in Table 3-3.

Figure 3-5 shows that the range of the measured cohesive forces of the Murchison and the Allende particles is approximately two orders of magnitude wider than the range of the model cohesive forces estimated by assuming a perfect sphere with a synthesized size distribution. A similar tendency is observed for the other irregular particles. This suggests that the particles of several tens of micrometers in size have a cohesive force whose distribution and values are approximately two orders of magnitude wider and more than one order of magnitude smaller than that of particles estimated on the basis of the perfect sphere assumption, respectively. These results are consistent with the results of a previous study (Nagaashi et al., 2018). The irregular particles have cohesive forces, which are several to a few tens of times lower than those of spherical particles. Among the irregular particles, LL6 and aggregates (the largest) have approximately six times larger

cohesive forces than that of Tagish Lake particles (the smallest) in $\overline{F_{\mathrm{meas}}}$. If the microporosity of the particles are considered, the tendency will be more prominent: The bulk porosity of Murchison used to estimate the mass of the meteorite fragments is smaller than Tagish Lake and larger than LL chondrites and Millbillillie.

Figure 3-6 shows the cumulative number fractions of the cohesive force at ambient temperature and pressure against a glass slide for 40–80 μm-sized Allende and Tagish Lake meteorite fragments prepared with a mortar and pestle or by a projectile impact. Figure 3-7 shows those against a stainless steel slide for 40–80 μm- and 4–8 μm-sized Allende meteorite fragments prepared with a mortar and pestle. The result of the 4–8 μm-sized fragments pressed on the slide at a centrifugal acceleration of $8 \times 10^4\, g_{\mathrm{E}}$ before the measurements is also shown. Figure 3-8 shows the cumulative number fractions of the cohesive force at ambient temperature and pressure against a glass slide for Murchison meteorite fragments, which were pressed on the slide at a centrifugal acceleration of $5 \times 10^3\, g_{\mathrm{E}}$ before the measurements. The results of Murchison without press-on are also shown. Table 3-3 summarizes the values of each parameter when fitting the data with Equation 3-5.

Figure 3-6 shows there is no significant difference between fragments prepared with a mortar and pestle and by a projectile impact, both for Allende and Tagish Lake, and this is confirmed by the Mann-Whitney U test (Mann and Whitney, 1947) (probability $P = 0.28$ and 0.47 for Allende and Tagish Lake, respectively). By contrast, the measured cohesive force of Allende fragments is approximately two to three times larger in $\overline{F_{\mathrm{meas}}}$ than that of Tagish Lake fragments.

Table 3-3 shows the measured cohesive force of 40–80 μm sized fragments of Allende meteorite against a stainless steel plate is approximately two times larger in $\overline{F_{\mathrm{meas}}}$ than that against a glass slide. This is consistent with the fact that the Hamaker constant in Equation 1-13 for metals is 4–6 times larger than that for silica, and the constant between material 1 and material 2, A_{12}, is represented as $A_{12} \sim \sqrt{A_{11}A_{22}}$ where those between materials 1 and between materials 2 are A_{11} and A_{22}, respectively (Israelachvili 2011). Figure 3-7 shows the measured cohesive force against the stainless steel slide of 40–80 μm sized Allende fragments is roughly three times larger in $\overline{F_{\mathrm{meas}}}$ than that of 4–8 μm-sized fragments without press-on. In contrast, it is not significantly different from those with press-on ($P = 0.12$). Figure 3-8 shows that the press-on at 5×10^3 g_{E} has no significant effect on the measured cohesive force against a glass slide for Murchison ($P = 0.71$).

If any increase in cohesive force after press-on was observed, it may be due to a plastic deformation when the force of the press-on exceeds the elastic limit of the surface

asperities (Lam and Newton, 1991) or due to an increase in the number of points of contact with the slide. According to Hertz theory (Hertz, 1896), when two contacting elastic bodies with surface asperity radii R_{asp1} and R_{asp2}, Young's moduli E_1 and E_2, and Poisson's ratios v_1 and v_2 are compressed against each other by a force F, the resulting maximum contact pressure, P_{max}, is given by

$$P_{\text{max}} = \left(\frac{6FE^{*2}}{\pi^3 R_{\text{asp}}^2}\right)^{1/3} , \qquad (3-6)$$

where E^* is expressed in Equation 1-16 and R_{asp} is the reduced radius of the surface asperity expressed in Equation 1-11. Here we assume that R_{asp} is 0.1 μm and equivalent for the small Allende fragments with the a-axis length of 6 μm and Murchison fragments with the a-axis length of 60 μm. We also assume that the number of points of contact with the slide is the same. We use 54 GPa and 0.17 for silica (Wada et al., 2009) as the Young's modulus and Poisson's ratio for the particles and the glass slide, respectively, and 191 GPa and 0.3 (Xie et al., 2021) as those for stainless steel slides, respectively. Substituting $F = M\beta$, where M is one particle mass expressed in Equation 3-2c, P_{max} experienced by Murchison pressed on the glass slide at β of 5×10^3 g_E is estimated to be ~4 GPa and about three times larger than that experienced by small Allende pressed on the stainless steel slide at β of 8×10^4 g_E. Since Murchison, which would experience larger pressure, has no increase in cohesive force, the increase in cohesive force due to press-on for small Allende would be due to the increase in contact points rather than plastic deformation.

Considering that the increase in contact points due to the press-on results in an increase in the cohesive force of small Allende, Figure 3-7 gives the following two key considerations. The first is that the cohesive force is likely to be independent of particle size in the few to tens of micron size range. The second is that particles of tens of microns are likely to contact with a slide at multiple points, typically at three points, under the Earth's gravity, while particles of a few microns, with a mass of about 10^{-3} of those, are likely to contact with a slide at a single point under the Earth's gravity and come into contact with a slide at multiple points under the centrifugal acceleration of 8×10^4 g_E. This may also explain that the cohesive force of spherical glass particles with a diameter of 50 μm measured using atomic force microscope cantilevers (LaMarche et al., 2017) is a fraction of the value determined in this study. In the case of the cantilever method, the contact between the plate and particles is unstable at one point, but in the case of this study, the contact between the slide and particles under the Earth's gravity may be stable at multiple points even for spherical particles due to the surface roughness.
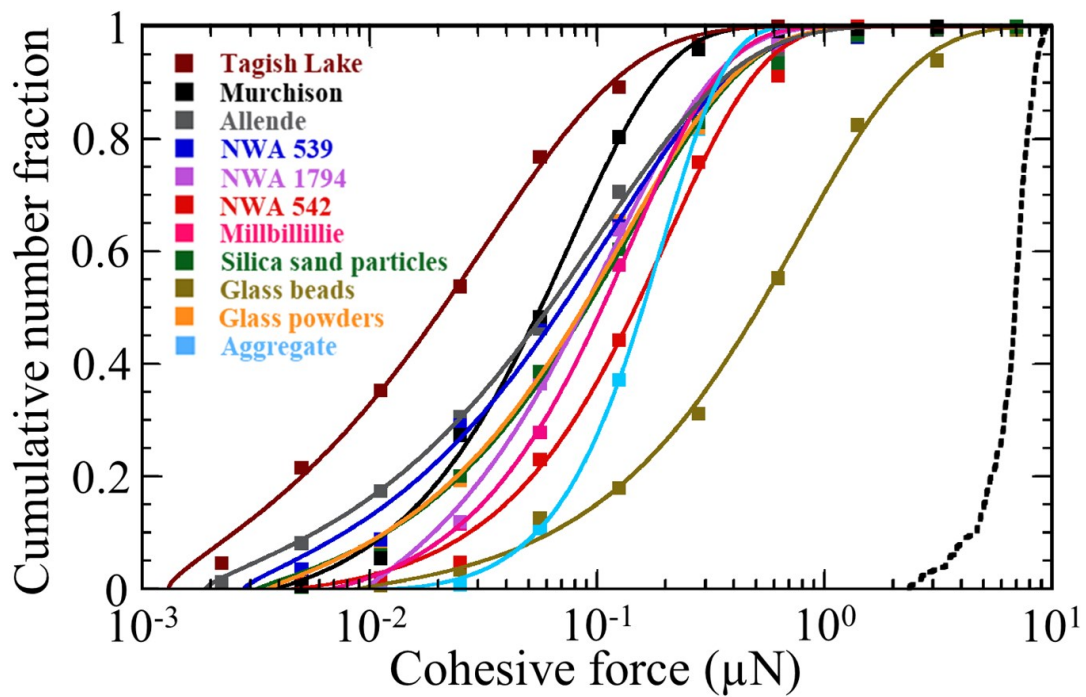
Figure 3-5 Measured cohesive force of meteorite fragments prepared with a mortar and pestle, glass particles, silica sand particles, and aggregates at ambient condition.
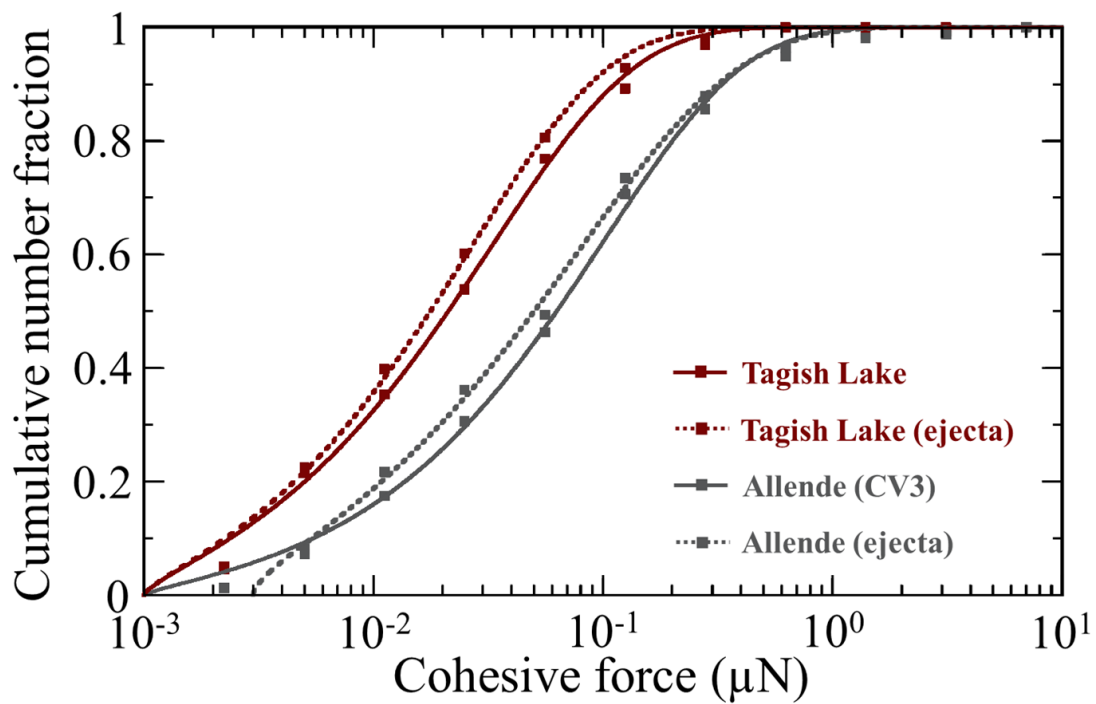

Figure 3-6 Measured cohesive force of meteorite fragments prepared with different crushing methods.
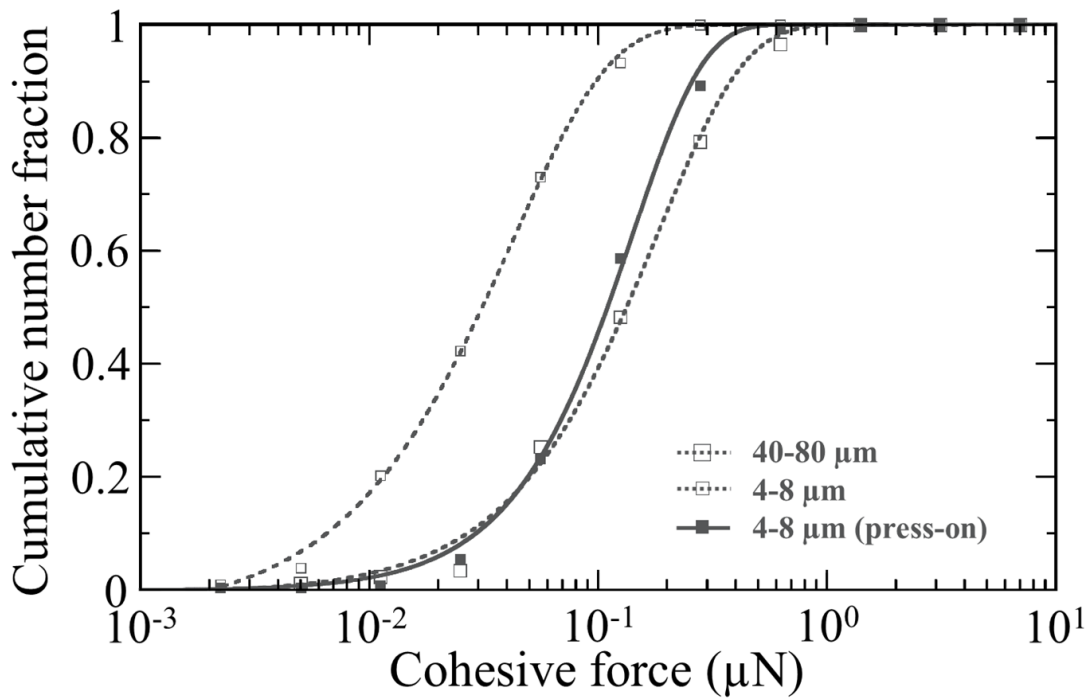
Figure 3-7 Measured cohesive force of Allende with different sizes and of small Allende with press-on.
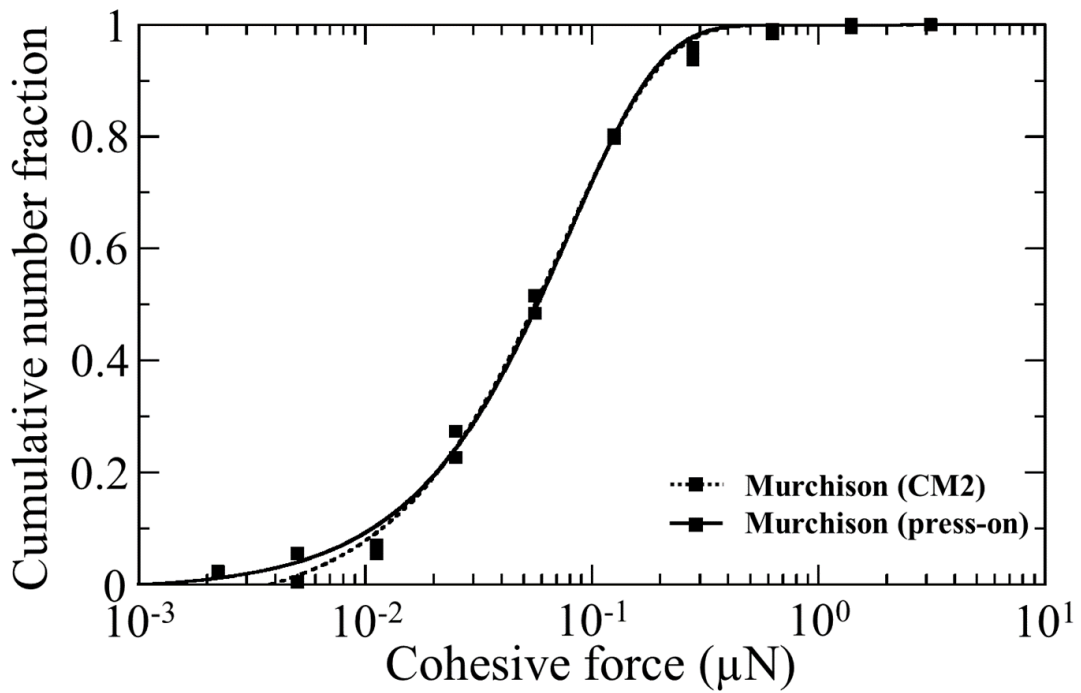

Figure 3-8 Measured cohesive force of Murchison with and without press-on.

Table 3-3 $\overline{F_{\text{meas}}}$, $\phi_{F_{\text{meas}}}$, F_{meas0}, **and the numbers and fraction of the samples in the cohesive force measurement**

At ambient condition against a glass slide

Sample	$\overline{F_{\text{meas}}}$ (μN)	$\phi_{F_{\text{meas}}}$	F_{meas0} (μN)	Number of particles	Measured number fraction
Allende (CV3)	0.10	0.69	0.0019	170	0.94
Allende (ejecta)	0.085	0.63	0.0030	84	0.99
Tagish Lake (C2-ung)	0.034	0.68	0.0013	66	0.99
Tagish Lake (ejecta)	0.027	0.70	0.0013	99	0.99
Murchison (CM2)	0.076	1.0	0.0038	219	0.98
Murchison (press-on)	0.080	1.1	0.0010	128	1.0
NWA 539 (LL3.5)	0.11	0.72	0.0028	113	0.98
NWA 1794 (LL5)	0.12	0.89	0.0096	175	1.0
NWA 542 (LL6)	0.20	1.0	0.0046	104	0.98
Millbillillie (eucrite)	0.14	1.0	0.0067	276	0.99
Silica sand particles	0.14	0.82	0.0032	328	0.94
Glass beads	0.79	0.84	0.0087	349	0.97
Glass powders	0.13	0.81	0.0036	145	0.99
Silica sphere aggregate	0.19	1.5	0.011	121	1.00
Silica sphere monomer (predicted)	0.053	1.9	0.0095	186	-

At ambient condition against a stainless steel slide

Sample	$\overline{F_{\text{meas}}}$ (μN)	$\phi_{F_{\text{meas}}}$	F_{meas0} (μN)	Number of particles	Measured number fraction
Allende (small)	0.042	1.0	0.0022	104	1.0
Allende (small, press-on)	0.14	1.4	0.0012	286	0.98
Allende	0.18	1.1	0.0027	87	1.0

At heated and/or evacuated condition against a glass slide

| Sample	Conditions	$\overline{F_{\mathrm{meas}}}$ (μN)	$\phi_{F_{\mathrm{meas}}}$	F_{meas0} (μN)	Number of particles	Measured fraction
Allende	110 ℃, 1 hour	0.23	1.2	0.0048	89	1.0
	250 ℃, 1 hour	0.47	0.83	0.0025	236	0.99
	350 ℃, 1 hour	0.30	0.87	0.0030	139	0.97
	350 ℃, 24 hours	0.32	0.91	0.018	125	0.90
	20 ℃ and 10 Pa, 1 hour	0.058	0.74	0.0021	73	0.99
	110 ℃ and 10 Pa, 1 hour	0.44	0.62	0.0023	59	0.88
	250 ℃ and 10^{-3} Pa, 48 hours	0.19	0.84	0.0023	253	0.96
Tagish Lake	110 ℃, 1 hour	0.092	1.1	0.0020	81	0.98
	250 ℃, 1 hour	0.17	0.99	0.0014	98	0.97
	250 ℃, 1 hour → 20 ℃	0.022	0.57	0.00092	296	0.99
	250 ℃, 1 hour → 20 ℃ → 250 ℃, 1 hour	0.086	1.0	0.0014	141	1.0
Silica sphere aggregate	350 ℃, 24 hours	0.66	1.4	0.041	149	0.91

3.3.2 Cohesive force at heated and evacuated conditions

Figures 3-9 and 3-10 show the cumulative number fraction of measured cohesive force at various conditions for Allende, Tagish Lake, and aggregates, and the cumulative number fraction of equivalent circular diameter of the particles used in the measurements, respectively. The values of each parameter when fitting these measurements with Equation 3-5 are summarized in Table 3-3. The cohesive force is affected by heating before measurements. The measured cohesive force of Allende fragments and aggregates after they were heated are approximately three to four times larger in $\overline{F_{\mathrm{meas}}}$ than those at ambient temperature. This increase is probably due to the removal of adsorbed water molecules (Kimura et al., 2015, Steinpilz et al., 2019, Pillich et al., 2021) rather than thermal alteration. This increase is consistent with 2–3 fold increase in cohesion obtained from direct shear tests at heating and evacuating conditions for sand and silica (Vey and Nelson, 1965, Bromwell 1966, Nelson and Vey, 1968), and is consistent with a little to 7 fold increase in surface energy of silica obtained by the same technique in the same study,

as shown in Figure 1-3. However, this increase is smaller than the previously estimated up to 10 fold increase of surface energy based on tensile strength measurements of aggregates consisting of silica spheres (Steinpilz et al., 2019) and ordinary chondrite fragments (Pillich et al., 2021) even if heating at similar duration and temperature. The large increase of the previous studies, which are based on an indirect method, could be attributed to the uncertainty of the relationship between tensile strength and cohesive force.

The measured cohesive force of Tagish Lake meteorite fragments after they were heated is also approximately three to four times larger in $\overline{F_{meas}}$ than those at ambient temperature. In order to examine the possibility that the removal of interlayer water at these temperatures, which is described in section 3.2, affected the cohesive force of Tagish Lake fragments, we conducted additional two heating measurements. The first measurement was performed on the Tagish Lake fragments that were heated at 250°C for one hour, cooled to ambient temperature, and then deposited on a glass slide. The second measurement was performed after the fragments used for the first measurement were heated again at 250°C for one hour. As shown in Figure 3-9, for the former, the measured cohesive force was not significantly different from those without heating ($P = 0.13$), which suggests the presence of adsorbed water molecules between the slide and the fragments, caused by the adsorption on the surfaces during the cooling. For the latter, the measured cohesive force became greater, which suggests the removal of the adsorbed water molecules again. Therefore, even if the interlayer water is lost by heating, there is no significant effect on the cohesive force, and the removal of adsorbed water molecules results in the increase of cohesive force even for Tagish Lake fragments.
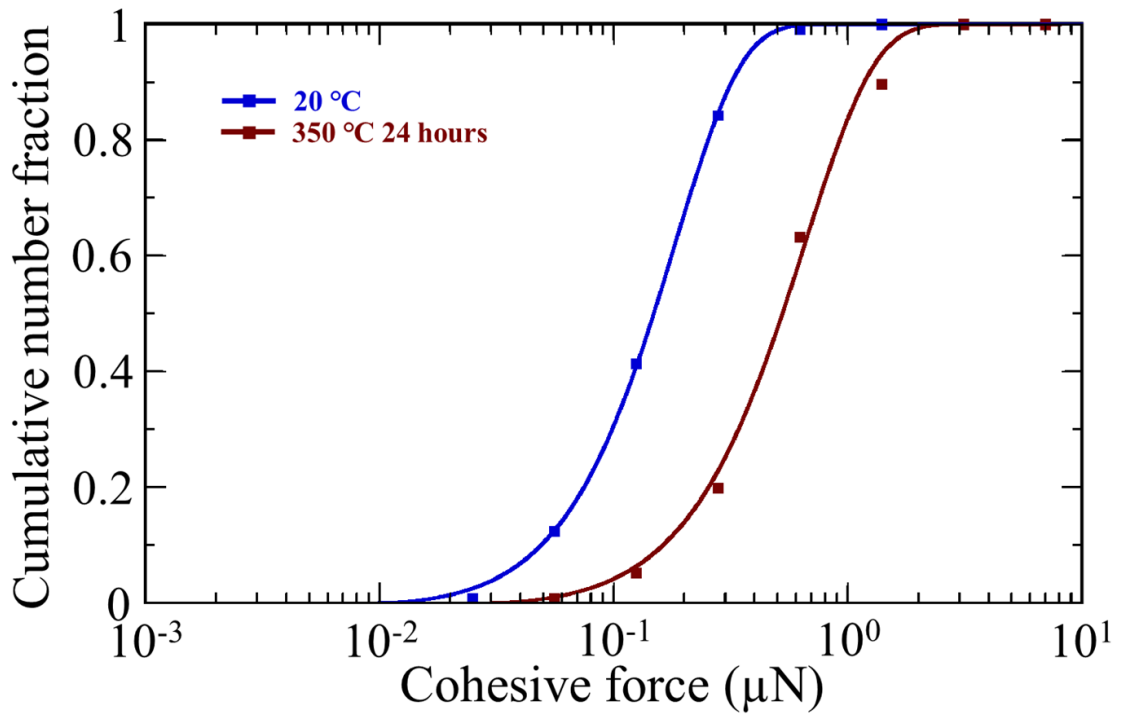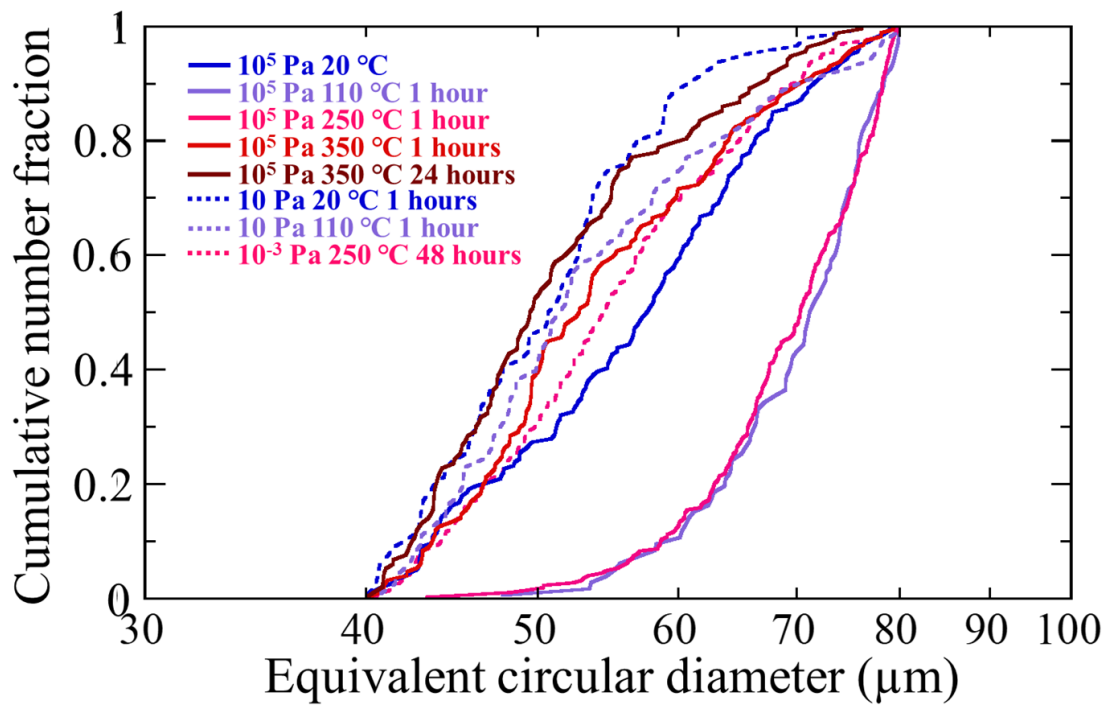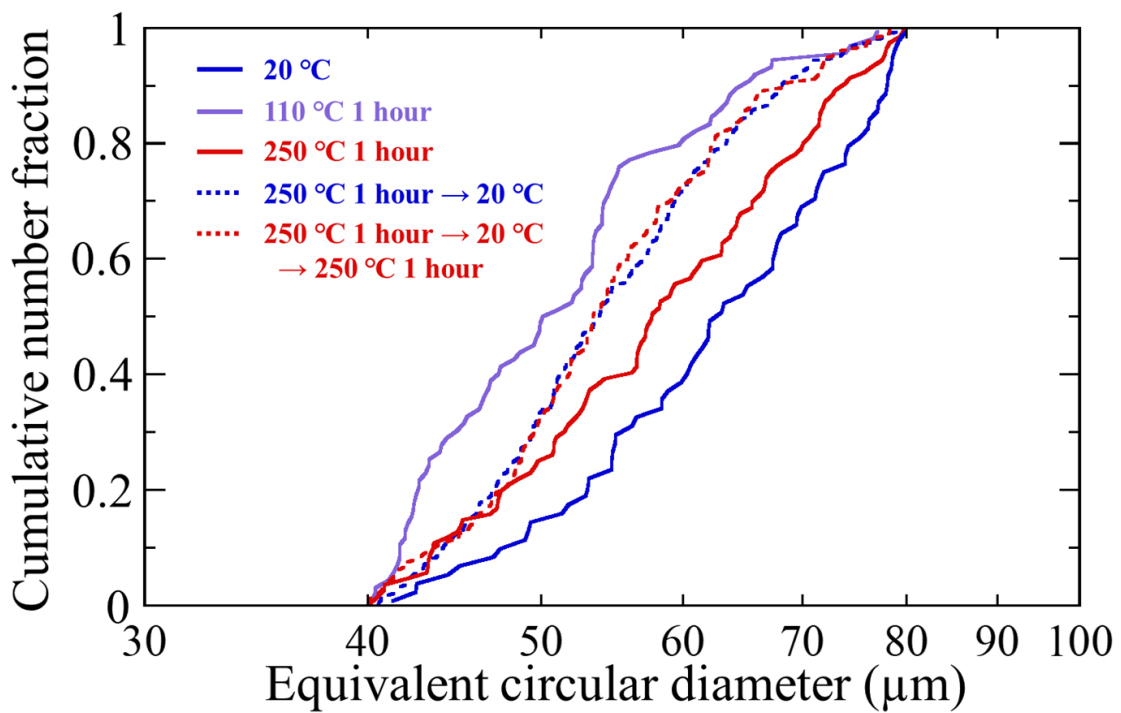
(a)

(b)

52
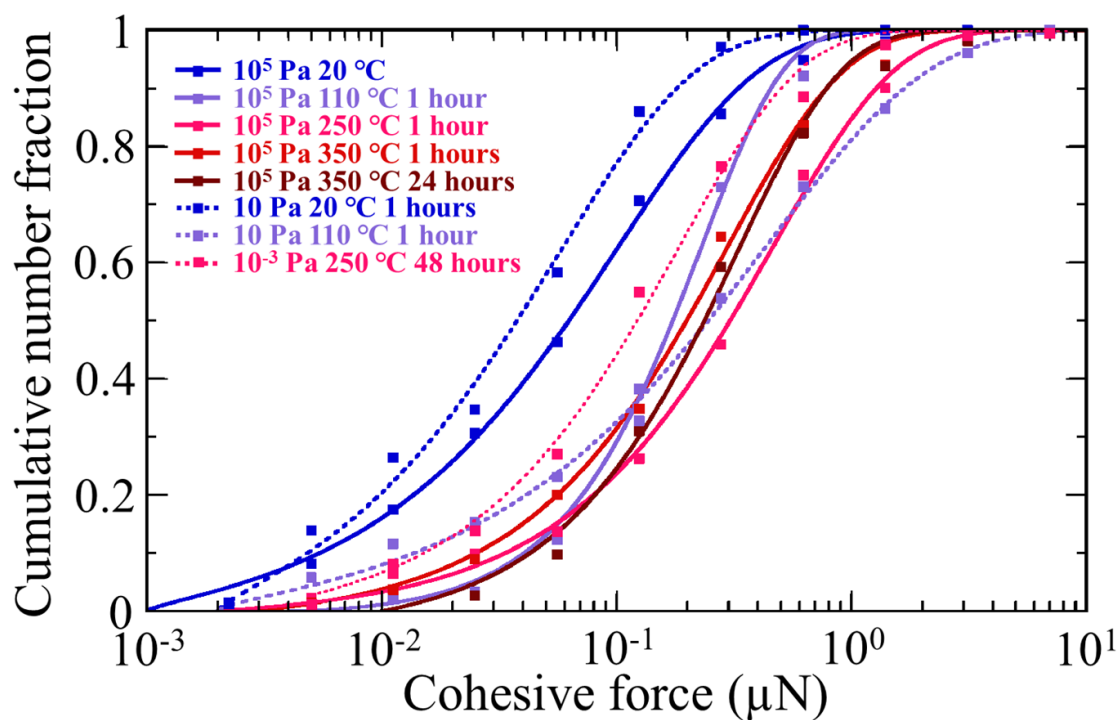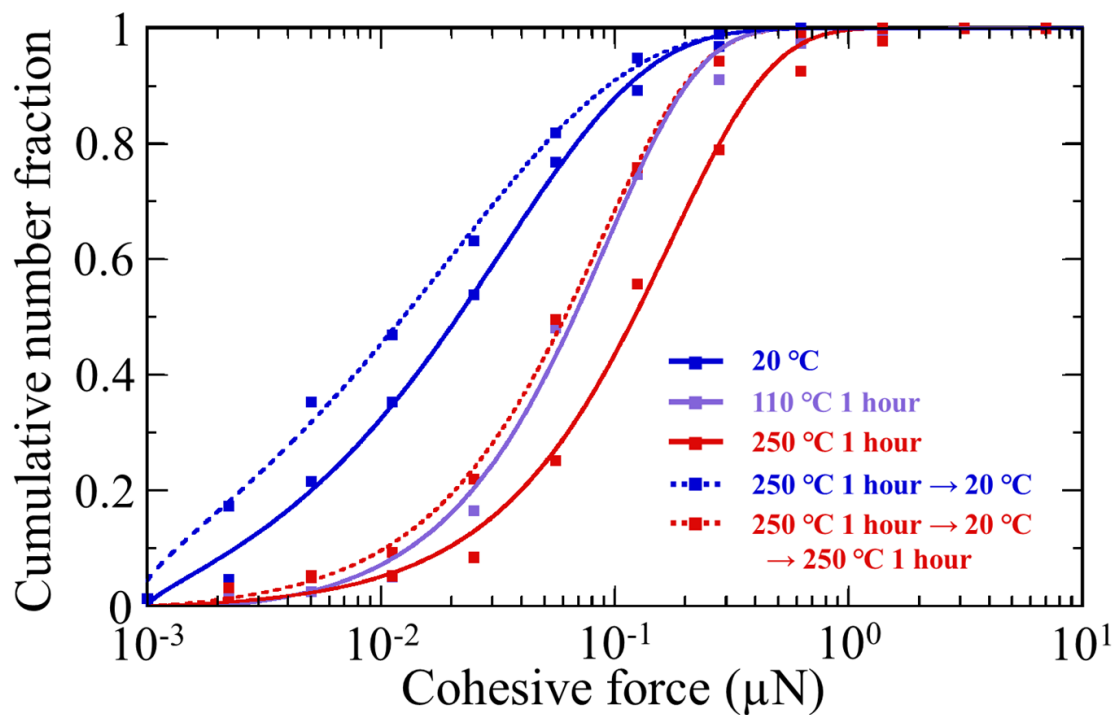
Figure 3-9 Measured cohesive force of meteorite fragments, prepared with a mortar and pestle, and aggregates after heating and evacuating. (a) Allende. (b) Tagish Lake. (c) Silica sphere aggregates.

(a)

Legend for (a):
- 10^5 Pa 20 °C
- 10^5 Pa 110 °C 1 hour
- 10^5 Pa 250 °C 1 hour
- 10^5 Pa 350 °C 1 hours
- 10^5 Pa 350 °C 24 hours
- 10 Pa 20 °C 1 hours
- 10 Pa 110 °C 1 hour
- 10^{-3} Pa 250 °C 48 hours

(b)

Legend for (b):
- 20 °C
- 110 °C 1 hour
- 250 °C 1 hour
- 250 °C 1 hour → 20 °C
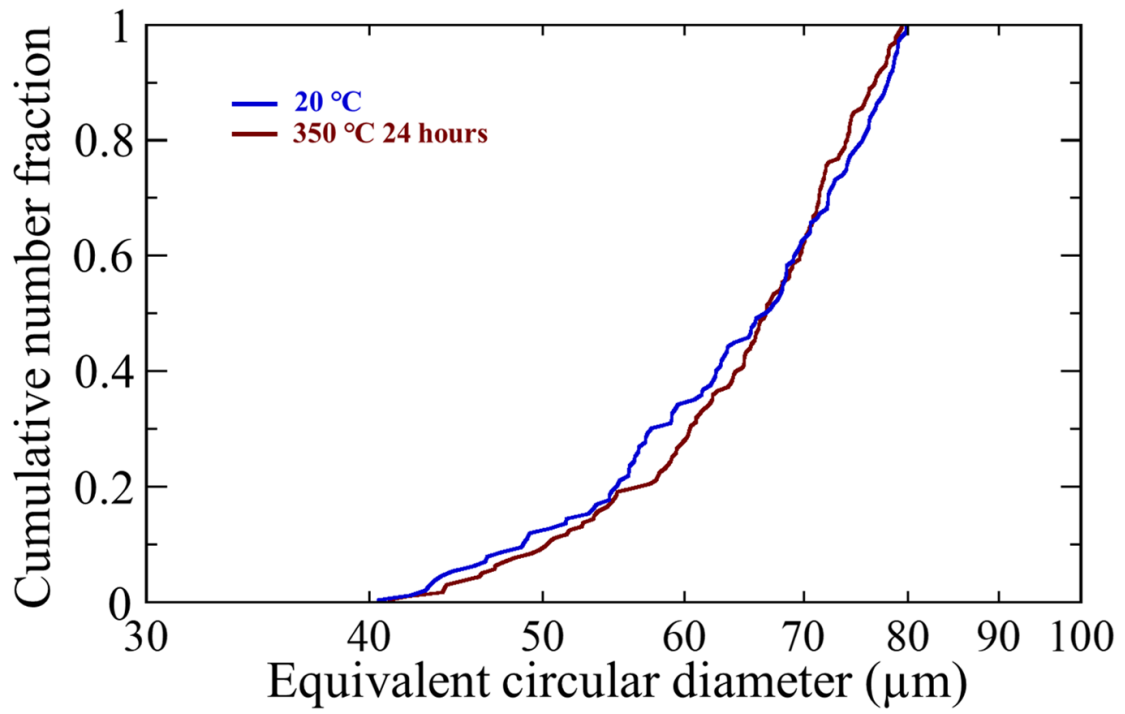- 250 °C 1 hour → 20 °C → 250 °C 1 hour

54

(c)

Figure 3-10 Size distribution of particles used in Figure 3-8. (a) Allende. (b) Tagish Lake. (c) Silica sphere aggregates.

Chapter 4

Discussion

Parts of this chapter have been published as Nagaashi, Y., Aoki, T., Nakamura, A. M., 2021, Icarus, 360, 114357, and will be published as Nagaashi, Y. and Nakamura, A. M. (in prep.).

4.1 Effect of water molecule adsorption on cohesive force

An application of the results obtained in this study to airless environments, such as small bodies, requires the consideration of the effect of the measurements being conducted in the atmosphere. A previous study introduced surface cleanliness $S = \Omega/t$, where Ω is the radius of mineral molecule and t is the adsorbate thickness, and modified the van der Waals force between two macroscopic spheres in Equation 1-12 to Equation 1-32 (Perko et al., 2001). In the absence of adsorbed water molecules, t can be written as Ω. When there are n ($n \geq 1$) layers of water molecules on the surfaces, t can be written as $\Omega + r_w + (n\text{-}1) \times 2r_w$, where r_w is the radius of water molecule. Here, we refer to the cohesive force and surface energy in the former condition as F_{vac} and γ_{vac}, respectively, and refer to those in the latter condition as F_{air} and γ_{air}, respectively. From Equation 1-32,

$$\frac{F_{vac}}{F_{air}} = \frac{\gamma_{vac}}{\gamma_{air}} = \left\{\frac{\Omega + r_w + (n-1) \times 2r_w}{\Omega}\right\}^2 . \qquad (4-1)$$

Here we assumed $r_w = 0.125$ nm (Israelachvili & Wennerström, 1996) and $\Omega = 0.132$ nm (Perko et al., 2001). In this study, it was estimated that ~2 layers of water molecules were adsorbed on the particle surface during the measurements at a relative humidity of 30%–40% as described in section 3.2. We can estimate that $\gamma_{vac} = 15 \, \gamma_{air}$. Previous studies, which were based on tensile strength measurements, suggested that the surface energy of silica particles and ordinary chondrite fragments may be up to 10 times greater in a vacuum than in the atmosphere (Steinpilz et al., 2019, Pillich et al., 2021). At first glance, the estimate by this simple model is comparable to the estimations of the previous studies. However, the range of increase in cohesive force from ambient temperature to an elevated temperature at 110–350 °C for removing adsorbed water molecules measured in this study is 3–4 times, which is smaller than those estimates, even though aggregates consisting of amorphous silica spheres in this study were heated to higher temperatures and for the

same duration than was done in the previous study testing the tensile strength of the silica sphere aggregates (Steinpilz et al., 2019). The previous study to assess the effect of adsorbed water on cohesive force was based on tensile strength measurements, i.e., an indirect method, and there is uncertainty in the relationship between the tensile strength of the aggregates and the cohesive force between the constituent particles. In addition, the model estimation according to Equation 4-1 is considered to be an overestimation because it neglects the attraction between adsorbed water molecules. Thus, in the following discussions on a protoplanetary disk and an asteroid environment, we assume that the cohesive forces in those environments are 3.5 times larger than in ambient condition, based on the direct measurement of cohesive force in this study.

4.2 Effect of particle shape on cohesive force

4.2.1 Circularity and roughness

In Figure 4-1a, we plot the measured cohesive force normalized by the JKR theory prediction for spherical particles in Equation 1-28, against the mean circularity of the particles. For the JKR theory prediction we considered the surface energy of silica in open air to be 0.025 J m^{-2} (Kendall et al., 1987). The cohesive forces between spherical glass beads (circularity of 0.933) and irregularly shaped crushed glass particles (circularity of 0.718), ~40 μm in size, and glass substrates of different surface roughness values measured by the impact separation method (Iida et al., 1993) are also shown in Figure 4-1a. Since particles of several tens of microns in size are likely to contact with a slide at approximately three points, as described in section 3.3.1, here 1/3 of the typical cohesive force in Table 3-3 and of the previous measurement results were used. In the previous study (Iida et al., 1993), for a smooth substrate with R_a of a few nm, spherical glass beads exhibited cohesive forces ~4 times greater than that of irregularly shaped crushed glass. This decrease of the cohesive force with decreasing circularity of the particles has been generally observed (Iida et al., 1993; Salazar-Banda et al., 2007). The microscopic surface geometry of the substrates significantly affects the magnitude of the cohesive force. In the previous study (Iida et al., 1993), spherical glass beads for the rough substrates with R_a of ~40 nm and ~350 nm exhibited ~4 and ~24 times smaller cohesive forces than for the smooth substrates with R_a of a few nanometers. The surface roughness of the spherical glass beads used in this study is ~24 nm, which may explain why the cohesive force of the beads is several times smaller than the force predicted using the JKR theory. The

smaller cohesive forces of the irregular particles, that is, the glass powder and silica sand particles, whose R_a are comparable to those of glass beads, could be due to the macroscopic shape effects, as revealed in previous studies (Iida et al., 1993; Salazar-Banda et al., 2007). Another study (LaMarche et al., 2017) explained the measured cohesive force of spherical glass beads using two scales of surface roughness rms (nanometers and tens of nanometers) determined for local surface profiles of the particles (15 μm × 15 μm) at one order of magnitude finer resolution than our measurements.

To characterize the effect of circularity C and surface roughness R_a, we assumed a power-law relationship for the effect of the circularity of the particles on the cohesive force. We also assumed that the effect of the nanometer-sized roughness of the glass slide used in this study and the smooth substrate used in the previous study (Iida et al., 1993) can be negligible. Using the three data points of the glass particles and silica sand particles with similar R_a of tens nm in this study, we derived the following circularity-dependent empirical relationship:

$$\frac{\overline{F_{\text{meas}}}}{3F_{\text{JKR}}} = AC^{7.5\pm0.6}. \qquad (4-2)$$

In Table 4-1, we summarize the values of constant A derived using the median C and $\overline{F_{\text{meas}}}$ obtained at ambient condition as well as Equation 1-28 using the median radius for each particle type. Here we assumed that the circularity dependence of the cohesive forces of any particles is represented by the same slope. In Figure 4-1b, A of each particle type is plotted against its R_a. We applied Equation 4-2 to the data obtained in a previous study by Iida et al. (1993) and plotted the results in Figure 4-1b, where we used the R_a of the substrates. As the figure shows, A decreases with increasing R_a. The meteorite particles have small cohesive forces compared with those of glass powders and silica sand, which can be explained using the size of R_a. However, among the meteorite particles, a seven-fold difference in A is present between Tagish Lake and LL6. The SEM images of the surfaces of meteorite fragments in Figure 2-2 shows that Tagish Lake has finer structure than Allende. The abundance of fine surface asperities close to the resolution of the confocal microscope may have influenced the cohesive forces.

The empirical relationship in Equation 4-2 considers the surface roughness of the particles, as in the previous model, which uses two scales of surface roughness to account for the measured cohesive force (LaMarche et al., 2017). However, in the previous model, the small-scale roughness of nanometers dominates the reducing effect on the cohesive force, which differs from the empirical relationship shown in Equation 4-2, wherein only a roughness exceeding tens of nanometers is considered.
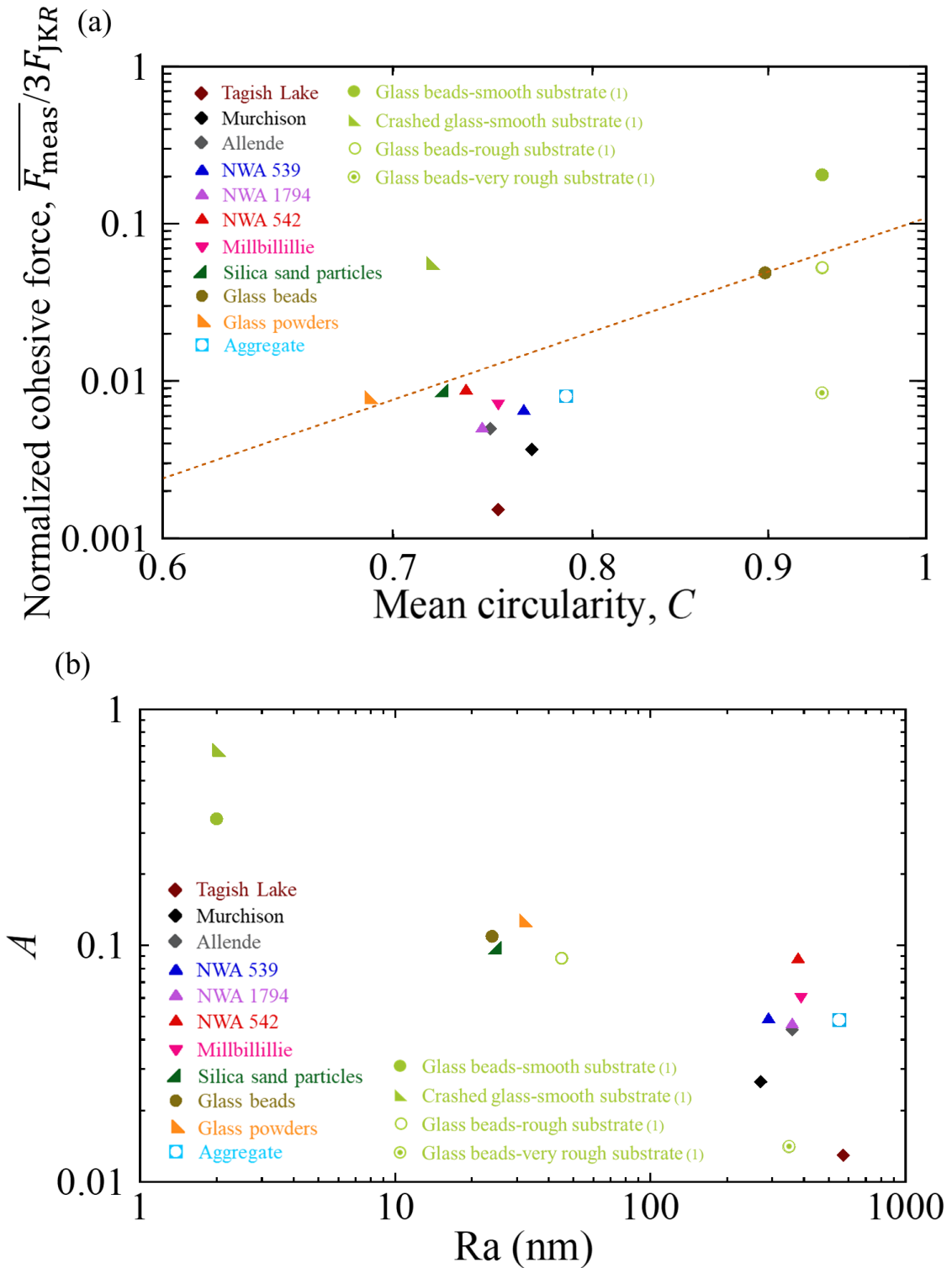
Figure 4-1 Effects of circularity and surface roughness on cohesive force. (a) Normalized cohesive force plotted against the mean circularity. The dashed line is the fitting line of Equation 4-2. (b) The A plotted against the R_a of the particles in this study and of the substrates in a previous study (Iida et al., 1993; 1).

Table 4-1 Results for the values of A and R_{eff}.

Sample	A	R_{eff} (µm)
Tagish Lake	0.013	0.048
Allende (CV3)	0.044	0.14
Murchison (CM2)	0.027	0.11
NWA 539 (LL3.5)	0.050	0.16
NWA 1794 (LL5)	0.047	0.17
NWA 542 (LL6)	0.089	0.29
Millbillillie (eucrite)	0.060	0.20
Silica sand particles	0.098	-
Glass beads	0.11	-
Glass powders	0.13	-
Silica sphere aggregates	0.049	-

4.2.2 Grains making up particle surfaces

In section 4.2.1, we attempted to explain the differences in measured cohesive force of glass, silica sand, aggregates, and meteorite fragments using the circularity C and arithmetic mean roughness R_a. The differences between the simulated particles, i.e., the glass and silica sand particles, and the meteorite fragments are affected by the roughness parameters. However, even though there are no significant differences in C and R_a, the measured cohesive force among the meteorites and the aggregates varies by a factor of several. To more fully discuss the effect of a surface structure of a particle on the cohesive force, in Figure 4-2 we show the distribution of cohesive force of amorphous silica sphere monomers predicted from the size distribution shown in Figure 2-1 based on the pull-off force in the JKR theory defined as Equation 1-28. Table 3-3 summarizes the values of each parameter fitted with Equation 3-5 for this predicted distribution. Here, we used the surface energy of silica at open air, $\gamma = 0.025$ J m^{-2} (Kendall et al., 1987), for both the silica spheres and the glass slide. As comparison, we show again the measurement results of aggregates consisting of the spheres in Figure 4-2. The typical cohesive force of the aggregates is several times larger than predicted for silica sphere monomers. Similar to the results of cohesive force measurements of Allende meteorite fragments with different sizes in Figure 3-7, this suggests that several of the silica spheres that make up the aggregate are in contact with the glass slide due to the Earth's gravity, as well as the cohesive force is not dependent on the bulk size. Two models have been proposed to

explain the cohesive force between aggregates, one introducing effective surface energy (Weidling et al., 2012) and the other assuming the number of contacts between monomers determines the cohesive force (Arakawa, 2020). In the former model, the geometric effect due to the porosity of the aggregate and the monomer size is included in the effective surface energy and the cohesive force increases in proportion to the aggregate size. In the latter model, the cohesive force is simply expressed by multiplying the cohesive force between monomers and the number of contacts between monomers, and is independent of the aggregate size. The results of this work support the latter.

As shown in Figure 3-7, the fragment size of Allende also doesn't affect the cohesive force. Thus, the latter model is also applied to the other meteorite fragments, i.e., the constituent grains of meteorites determine the cohesive force, not the bulk size of the particles. The SEM images in Figure 2-2 show that Tagish Lake fragments have fine surface structures which cannot be captured by the confocal laser scanning microscope used to acquire R_a. This is consistent with the low measured cohesive force of Tagish Lake.

The fine surface structure of Tagish Lake meteorite fragments may be attributed to the matrix grains they contain. Tagish Lake meteorite includes fine-grained matrix of >80 vol.% (Takayama and Tomeoka, 2012) and has undergone extensive aqueous alteration (Brown et al., 2000). In general, matrix grains tend to be finer in meteorites that have undergone aqueous alteration and coarser in meteorites that have undergone thermal metamorphism (Weisberg et al., 2006), which may account for the differences in surface structure and cohesive force among the meteorite fragments. Figure 4-3 depicts the cohesive force of the meteorite fragments, which are prepared using a mortar and pestle, measured at ambient temperature and pressure versus the abundance of matrix contained in the meteorites (Weisberg et al., 2006, Takayama and Tomeoka, 2012). Here, considering that the measured cohesive force is the value between a particle and slide (2-fold effect; Equation 1-28) and the value for multiple contact points (roughly 3-fold effect; Figures 3-7 and 4-2), each typical cohesive force is corrected to be 1/6 of the measured value and the values for a single point contact between particles are plotted in the figure. The cohesive forces of the matrix-rich meteorites tend to be lower than those of meteorites rich in chondrules, which have undergone melting, and those of eucrite and terrestrial silica sand, which also have undergone melting. In addition, meteorites with a high degree of thermal metamorphism tend to have greater cohesive forces. Therefore, the cohesive force of meteorite fragments, or asteroidal particles, is affected by the size and shape of the constituent grains, which reflect their formation and evolution process, and would be constant regardless of the bulk size, as suggested in Figure 3-7. If we ignore

the effect of the shape of the grains, using Equation 1-28, the size of the constituent grains R_{eff} could be calculated as follows:

$$3\pi\gamma R_{\text{eff}} = \frac{\overline{F_{\text{meas}}}}{3},\qquad(4-3)$$

In Table 4-1, we summarize the values of R_{eff} derived using $\overline{F_{\text{meas}}}$ at ambient condition and the surface energy of silica at open air, $\gamma = 0.025$ J m^{-2} (Kendall et al., 1987). The R_{eff} ranges from 0.05 to 0.3 μm. The typical size of silicate matrix grains found in carbonaceous chondrites ALHA 77307 (CO3.0), QUE 99177 (CR2), MIL07687 (unclassified), and Acfer 094 (unclassified) is 0.1–0.2 μm (Vaccaro 2017). The vast majority size of the individual grains found in chondritic porous interplanetary dust particles is ~0.050–0.2 μm (Wozniakiewicz et al., 2013). The R_{eff} and the sizes of those grains are comparable. It should be noted, however, that the fragments for which cohesive force measurements were conducted include components other than matrix.
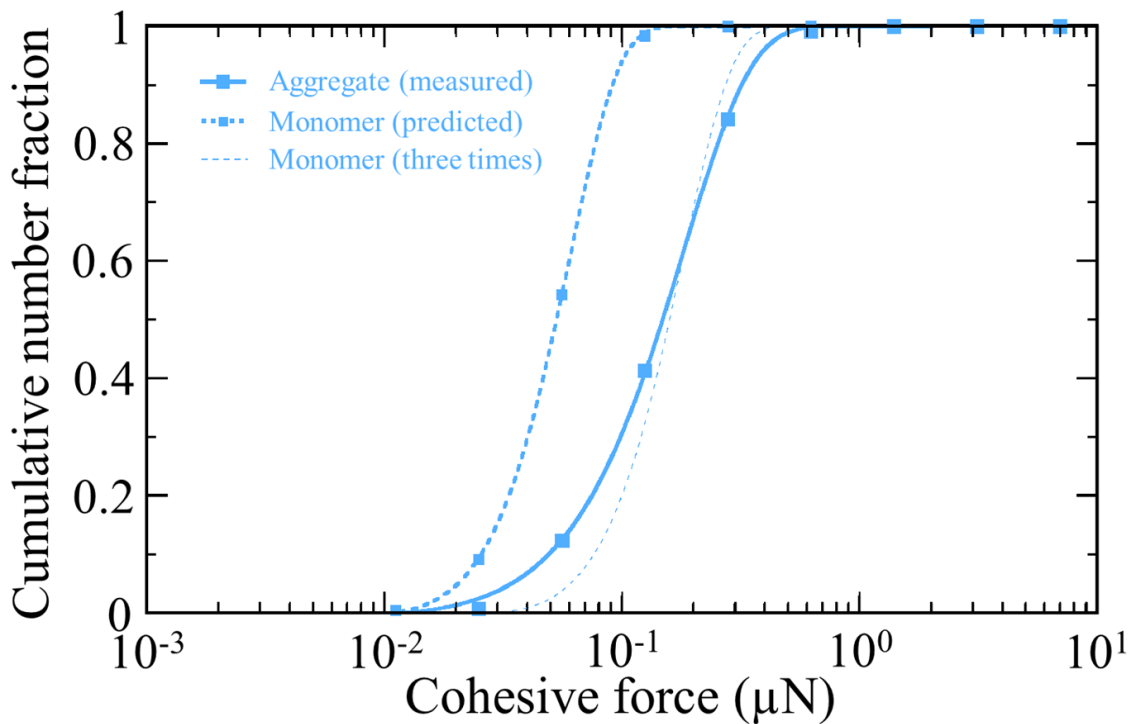

Figure 4-2 Theoretically predicted cohesive force of silica spheres and measured cohesive force of aggregates composed of them.
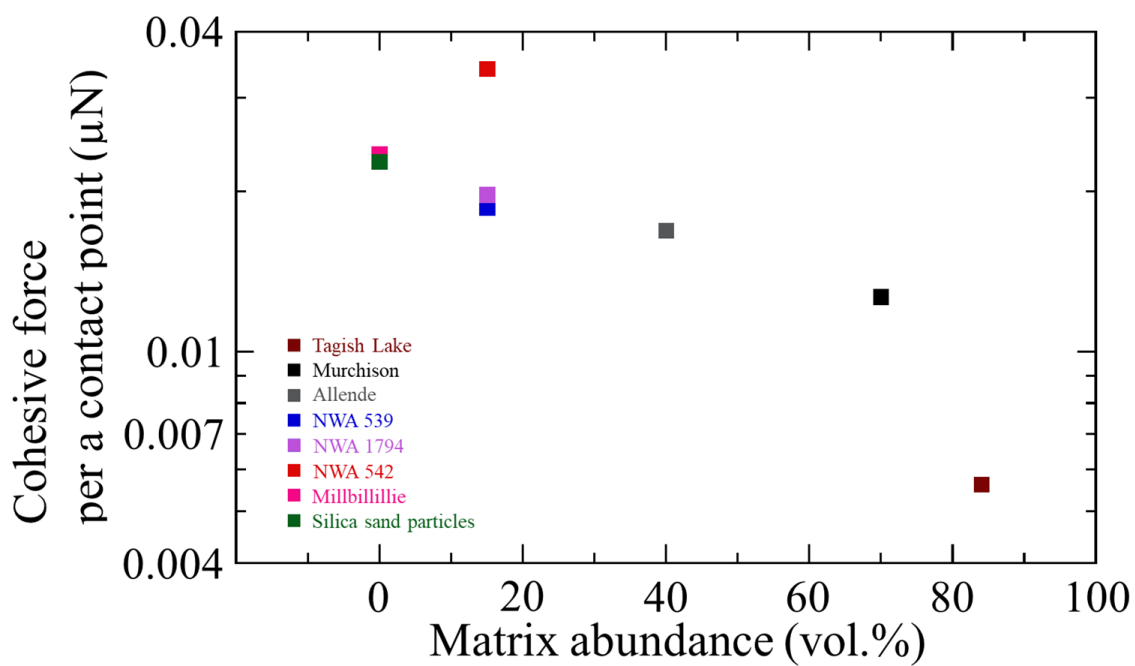
Figure 4-3 Measured cohesive force of meteorite fragments prepared with a mortar and pestle at ambient condition and their matrix abundance.

Chapter 5

Applications

Parts of this chapter have been published as Nagaashi, Y., Aoki, T., Nakamura, A. M., 2021, Icarus, 360, 114357, and will be published as Nagaashi, Y. and Nakamura, A. M. (in prep.).

5.1 Coagulation growth of dust particles

From the cohesive force measurements of Allende and Tagish Lake meteorites, and aggregates consisting of silica spheres, the cohesive force, i.e. surface energy, of silicate particles in an airless environment would be approximately 3–4 times greater than that in the Earth's atmosphere. The surface energy γ of amorphous silica spheres of 0.025 J m^{-2}, which is often used in discussions of growth conditions of silicate dust particles in protoplanetary disks, is a value at ambient condition (Kendall et al., 1987).

The critical velocity for collisional growth between dust aggregates with the same size was derived based on numerical experiments (Wada et al., 2009) as

$$\Delta v_{\text{crit}} \sim 15 \sqrt{\frac{E_{\text{break}}}{m}}, \tag{5-1}$$

where E_{break} is the energy required to pull apart two contacting spheres, as expressed in Equation 1-29, and m is the mass of one particle that makes up the aggregates. For aggregates consisting of 0.1 μm radius silica spheres of $E = 54$ GPa, $v = 0.17$, and particle density $\rho_{\text{P}} = 2.6$ g cm^{-3},

$$\Delta v_{\text{crit}} \sim 6 \left(\frac{\gamma}{0.025 \text{ J m}^{-2}} \right)^{5/6} \text{ m s}^{-1}. \tag{5-2}$$

The 3–4 fold increase in cohesive force, i.e., surface energy, due to the removal of adsorbed water found in this study may result in a critical velocity of ~15–19 m s^{-1}. This is lower than estimation of ~54 m s^{-1} by a previous study, which assumed larger surface energy of 0.25 J m^{-2} (Kimura et al., 2015). However, note that as described in section 1.2.3, the literature values for the surface energy of amorphous silica range by a factor of several at ambient condition. Also, note that the measured surface energies at elevated temperatures of 400 °C or less, which are considered equivalent to values at vacuum

conditions in a previous study (Kimura et al., 2015), was up to seven times higher than measured at ambient temperature by the same method and study, as shown in Figure 1-3.

In addition, the particle shape would be important in the discussion of the aggregation process. The critical velocity and the literature values of surface energy is for amorphous silica spheres. The differences in surface energy and particle shape from the actual dust particles may affect the growth process. From the results of cohesive force measurements in this study, the cohesive force of irregularly shaped particles would be lower than that of spherical particles. However, it has been confirmed that irregularly shaped particles tend to aggregate more easily than spherical particles. Irregularly shaped particles may stick to a plate at a higher impact velocity than spherical particles (Poppe et al., 2000). Free-falling streams consisting of irregularly shaped particles more rapidly form larger clusters than those of spherical particles (Nagaashi et al., 2018, 2021). As an interpretation, the possibility of more energy loss due to multiple contacts in a single encounter has been suggested. The particle shape may also affect the discussion of the accretion and disruption process of planetary ring particles, although the material of the particles is mainly water ice and is different from the particles studied here.

5.2 High mobility of surface particles

5.2.1 Cohesive strength of rubble-pile asteroids

The measured cohesive forces in Figure 4-3 were at ambient condition. Considering that the cohesive force of particles whose surfaces are cleared from water molecules is 3–4 times greater than that of unmodified particles, we estimated the cohesive forces of meteorite fragments in an asteroidal environment would be 3.5 times greater than measured at an ambient condition. We calculated the interparticle cohesive force per a contact point at asteroid condition, F_{as}, by multiplying $\overline{F_{meas}}/3$ by 3.5 for each meteorite. The F_{as} of each meteorite is summarized in Table 5-1. The F_{as} of fragments of carbonaceous chondrites, or C-type asteroids, and ordinary chondrites, or S-type asteroids, may be ~0.020–0.059 μN and 0.065–0.12 μN, respectively. As discussed in section 4.2.2, since the cohesive force of meteorite fragments is determined by the size and shape of their constituent grains, F_{as} would be constant with respect to the particle size, as long as plastic deformation does not occur.

According to a SPH study of rubble piles (Sugiura et al., 2021), a cohesive strength of ~100 Pa may be necessary for the transformation of asteroid Ryugu into a top-

shape (section 1.1.3). A breakup event by rotational disruption of C-type, main belt comet P/2013 R3 provides the estimated cohesive strength of the proto-body of 40–210 Pa (Hirabayashi et al., 2014). A fast rotation (1.9529 h) of an S-complex, inner-main belt asteroid (60716) 2000 GD65 requires a cohesive strength of 150–450 Pa (Polishook et al., 2016). As the equation of tensile strength of a powder layer in Equation 1-31, the cohesive strength is expected to be related to the inter-particle cohesive force per a contact point F_{as} in some form. However, there is uncertainty in the relationship. If a better formula is established, it may be possible to evaluate the typical particle sizes binding the objects based on the cohesive strength, as attempted in a previous study (Sánchez & Scheeres, 2014).

Table 5-1 Results for the values of F_{as}.

	F_{as} (µN)
Tagish Lake	0.020
Allende	0.059
Murchison	0.044
NWA 539	0.065
NWA 1794	0.069
NWA 542	0.12
Millbillillie	0.082

5.2.2 High mobility of surface particles

A previous study discussed the mobility of particles on Bennu by comparing cohesive and gravitational forces acting on particles resting on the surface (Bierhaus et al., 2021). The previous study assumed a van der Waals force between two macroscopic spheres as the cohesive force. The Hamaker constant of the lunar regolith $A = 4.3 \times 10^{-20}$ J and no adsorbed gas $t = \Omega = 1.32 \times 10^{-10}$ m (Perko et al., 2001, Scheeres et al., 2010) in Equation 1-32 were assumed, and a single contact point between particles was assumed. Figure 5-1a shows the van der Waals force and gravity,

$$F_g = \frac{\pi \rho_p d_p^{\,3}}{6} \left(\frac{4\pi G \rho_a}{3} - \omega^2 \cos^2 \Delta \right) \frac{d_a}{2},$$

acting on a spherical particle with a diameter d_p on a spherical C-type and S-type asteroid with diameter $d_a = 0.5$ km. Here, ω is the asteroid angular velocity, G is the gravitational constant, $\varDelta$ is the latitude of the particle, ρ_a is the bulk density of the asteroid, and ρ_p is the bulk density of the particle. We assume that ρ_a of C- and S-type asteroids are 1190 kg m^{-3} (Watanabe et al., 2019, Lauretta et al., 2019) and 1900 kg m^{-3} (Fujiwara et al., 2006), respectively. We assume that ρ_p of the particles of C- and S-type asteroids are 1640 kg m^{-3} (Tagish Lake: Hildebrand et al., 2006) and 3220 kg m^{-3} (the average of LL chondrites: Consolmagno et al., 2008). For simplicity, the effect of the asteroid's rotation was ignored. According to Equation 1-2, the total force of the gravity and cohesive force in pressure units is shown in Figure 5-1b. The previous study estimated that particles with tens of centimeters in size where the pressure is minimized on Bennu surface are the most mobile.

Meanwhile, the number of contact points between the particles on the surfaces affect the net cohesive force. The state of contact may be discussed using the Bond number B_o (e.g., Scheeres et al., 2010), which is represented by

$$B_o = \frac{mg}{F_{co}} \qquad (5-3)$$

where F_{co} is the cohesive force per a contact point. From the results shown in Figures 3-7 and 4-2, it is likely that under the Earth's gravity ~60 μm-sized Allende meteorite fragments and the aggregates are in contact with the slides at roughly three points, and ~6 μm Allende meteorite fragments with the slide at one point. The median masses of these particles are about 1×10^{-10}, 0.6×10^{-10}, and 1×10^{-13} kg, respectively, and B_o is calculated to be about 0.02, 0.01, and 2×10^{-5}, respectively, assuming F_{co} of Allende meteorite and aggregates is $\overline{F_{meas}}$ of ~6 μm-sized fragments and submicron-sized silica spheres, respectively. This suggests that B_o of at least 0.01 or greater would result in having about three contact points on a surface. B_o of at least 2×10^{-5} or less would result in having a single contact point. The former situation corresponds to particles with millimeter or more in size on sub-km-sized airless asteroids, and they would be held on the surfaces by the net cohesive force of about $3F_{as}$. Therefore, we assume a constant net cohesive force of 0.12 μN and 0.25 μN on the surface of a C-type asteroid and S-type asteroid, respectively.

However, as described in section 3.3.1, plastic deformation of particles may lead to greater cohesive force. Using the size of the constituent grains R_{eff} as expressed in Equation 4-3, we discuss the possibility of plastic deformation on asteroids. Replacing R_{as} in Equation 3-6 by $R_{eff} \sim 0.2$ μm, and assuming for simplicity that $F = \pi/6 \, \rho d^3 g$ where d is the particle diameter and g is the gravitational acceleration on the surface of an asteroid, and that particles are held to the surface at N contact points, Equation 3-6 can be rewritten as follows:

$$P_{max} \sim \frac{12}{N}\left(\frac{d}{10\text{ cm}}\right)\left(\frac{\rho_p}{2500\text{ kgm}^{-3}}\right)^{1/3}\left(\frac{g}{10^{-4}\text{ ms}^{-2}}\right)^{1/3}\text{ GPa}. \qquad (5-4)$$

Here, the Young's modulus and Poisson's ratio of the particles were assumed to be 54 GPa and 0.17 for silica (Wada et al., 2009). This suggests that the gravitational press-on for particles smaller than several tens of centimeters on a surface of 0.5 km-sized asteroid does not exceed the theoretical strength of silica glass of 24 GPa (Naray-Szabo and Ladik, 1960). However, for larger particles, the plastic deformation may occur. If we assume that particles break to increase the number of contact point N in order to reduce the maximum contact pressure P_{max}, N could increase in proportion to the applied force F, and thus the cohesive force could increase in proportion to F. This is supported by a previous study, which has shown that the measured cohesive force of particles increases linearly with the preliminary applied force due to plastic deformation (Lam and Newton, 1991).

We show the net cohesive forces $3F_{as}$ in Figure 5-1a. As the cohesive force for larger particles may show a linear increase with gravity due to plastic deformation, Figure 5-1a also show the cohesive force assumed to be proportional to the third power of particle size above ~60 cm, which is the diameter when $N = 3$ and $P_{max} = 24$ GPa. Figure 5-1a shows that assumption of cohesive force being proportional to the particle size overestimates binding on the surfaces from cohesive force by orders of magnitude in this size range. Figure 5-1b also shows the pressure from gravity and the net cohesive forces instead of the cohesive force proportional to the particle size. The pressure is lower than that obtained by assumption of cohesive force being proportional to the particle size, which suggests that the particles move more easily across the surface than previously expected. The size of particles preferentially moving on the surfaces is estimated to be ~1 cm, which is considerably smaller than the tens of centimeters in size of the previous study (Bierhaus et al., 2021). Indeed, there are some evidence of particle migration on asteroids. The low areas of Itokawa are filled with millimeter- to centimeter-sized particles (Miyamoto et al., 2007). Some craters on Ryugu and Bennu show evidence for material movements on the inner walls (Sugita et al., 2019, Walsh et al., 2019). A boulder migration and large amounts of debris have been observed during the touchdown on Ryugu (Morota et al., 2020). The deficit of small craters is found on the three asteroids, which may have been erased by material movements (Michel et al., 2009, Sugita et al., 2019, Walsh et al., 2019). The particle size suitable for migration estimated in this study is consistent with the size of particles which have been found to be ejected from Bennu (Lauretta et al., 2019) and covering the low areas of Itokawa (Miyamoto et al., 2007).
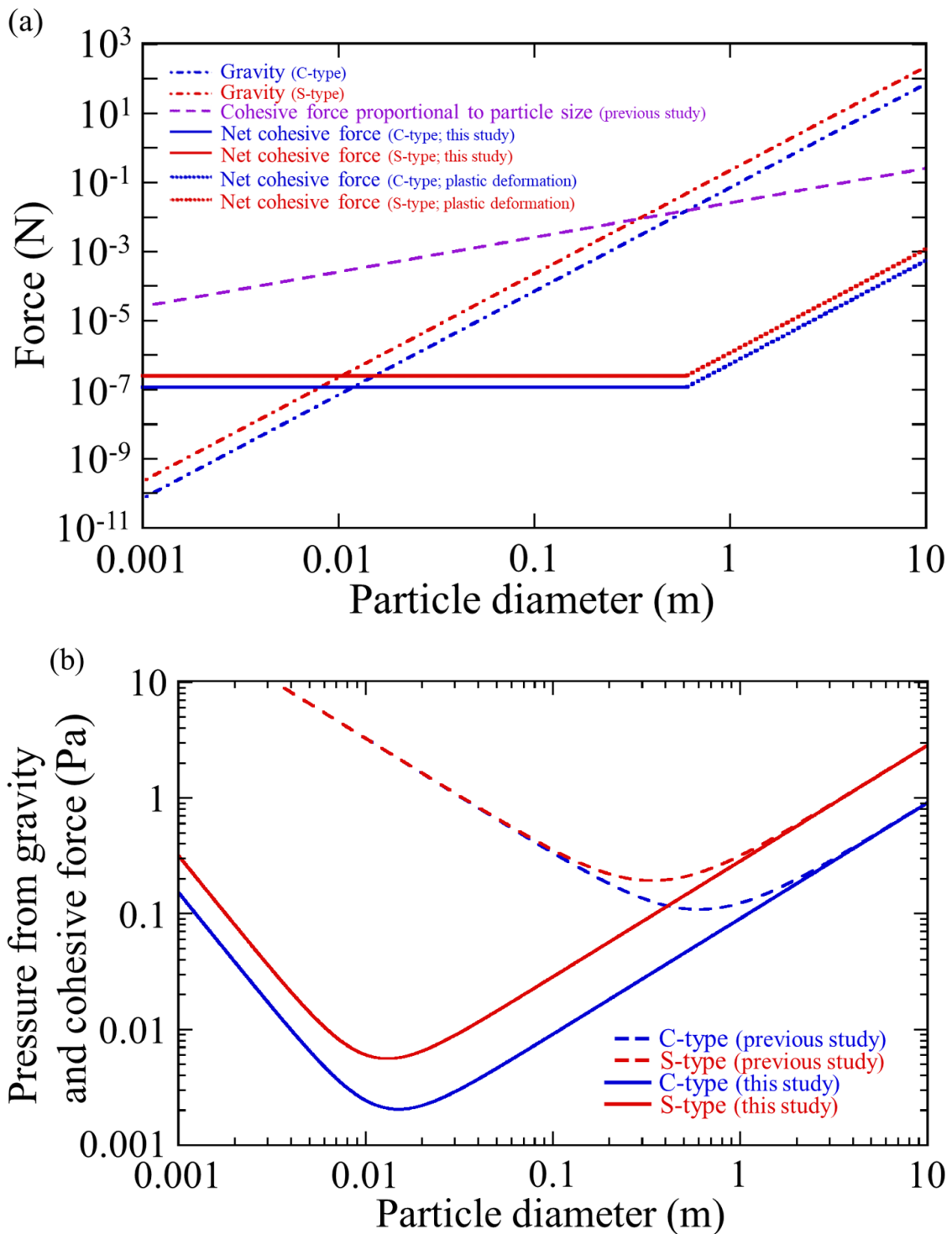
Figure 5-1 Cohesive force and gravity acting to particles on the surface of sub-km-sized C-type and S-type asteroid. (a) Comparison among gravity, previous cohesive force proportional to particle size, and the net cohesive force of this study. (b) Pressure from gravity and previous cohesive force proportional to particle size or the net cohesive force of this study.

Chapter 6

Conclusions

The centrifugal method was used to measure the cohesive force of meteorite fragments against smooth slides at ambient condition, and under ambient and/or reduced pressure after heating in order to remove adsorbed water molecules. The amount of water molecules adsorbed on the particle surface at ambient condition and the elevated temperature at which the adsorbed water molecules can be removed but no thermal alteration occurs were investigated. To characterize the particle shape, we obtained the axial ratio and circularity based on optical microscope images with a resolution of 1.3 or 0.66 μm pixel^{-1}, and the arithmetic mean roughness using a confocal laser microscope with a horizontal resolution of 0.125 μm pixel^{-1} and vertical resolution of 0.01 μm pixel^{-1}. The meteorites were carbonaceous chondrites (Tagish Lake, CM2, CV3), ordinary chondrites (LL3.5, LL5, LL6), and eucrite, which were prepared with a mortar and pestle or with projectile impacts. The fragments with equivalent circular diameters of several tens of microns and several microns were used. For comparison, several tens micron-sized spherical glass beads and irregularly shaped glass powders, silica sand particles, and aggregates produced by sieving sub-micron-sized amorphous silica spheres were also used.

The axial ratio, circularity, and arithmetic mean roughness of the meteorite fragments did not differ significantly depending on the preparation methods or meteorite types. The axial ratio of the meteorite fragments was similar to those of basalt impact fragments, particles recovered from asteroid Itokawa, and asteroidal boulders, was larger than those of silica sand particles and glass powders, and was smaller than those of aggregates and glass beads. The circularity of the meteorite fragments was similar to that of aggregates, was larger than those of silica sand particles and glass powders, and was smaller than that of glass beads. The arithmetic mean roughness of slides, glass particles and silica sand particles, and meteorite fragments and aggregates were nm-sized, tens of nm-sized, and hundreds of nm-sized, respectively.

The cohesive forces between a slide and the particles measured at ambient condition were one to two orders of magnitude lower than those estimated for perfect spheres with each particle size distribution using the JKR theory. We demonstrated that the effect of circularity (corresponding to a roughness of more than microns in this study) affects the differences in cohesive force among glass particles and silica sand particles,

70

and a finer-scale roughness affects the differences in cohesive force between them and meteorite fragments. Although there is no significant difference in arithmetic mean roughness (sub-microns in this study) among the meteorite types, the electron microscope images exhibited finer structures on the fragment surface of Tagish Lake than the resolutions of the above shape measurements. The measured cohesive force of Tagish Lake fragments was the lowest among the particles measured in this study.

The cohesive force of several micron-sized Allende fragments, which were pressed on a stainless steel slide by a centrifugal acceleration of 8×10^4 g_E (g_E is the Earth's gravitational acceleration) before the measurement, was several times larger than that without press-on, and was similar to that of several tens micron-sized. In contrast, the cohesive force of several tens of micron-sized Murchison fragments, which were pressed on a glass slide by a centrifugal acceleration of 5×10^3 g_E before the measurement did not increase, even though the experienced pressure at contact points due to the press-on was equivalent to that of small Allende fragments according to the elastic contact theory. The increase in cohesive force of the small particles due to the press-on would result from increase of the number of points of contact with the slide, rather than plastic deformation. This suggests that the smaller fragments at 8×10^4 g_E and the larger fragments at 1 g_E contact the slide at multiple points whereas the small fragments at 1 g_E contact the slide at a single point, and the cohesive force is not dependent on the fragment size. The cohesive force distribution measured for aggregates has a narrow width, as with that predicted from the size distribution of the constituent silica sphere monomers, and the typical cohesive force of the former was several times higher than that of the latter. This also suggests that the cohesive force of the aggregates was measured with several of the constituent spheres of the aggregates of the surface were in contact with the slide. Therefore, the cohesive force of particles would be determined by the surface structures, i.e., surface constituent grains, and not by the bulk size of fragments or aggregates. In fact, meteorites including more fine-grained matrix tend to have low cohesive force, while meteorites including more molten materials, meteorites that have undergone melting or higher degrees of thermal metamorphism, and terrestrial silica sands particles tend to have high cohesive force.

The cohesive force of particles increased by a factor of 3 to 4 by removing the adsorbed water molecules. This increase is consistent with those found at similar heating temperatures with respect to the surface energy of amorphous silica and cohesion from direct shear tests of sand and silica layers in previous studies. In contrast, this is smaller than the increase in surface energy estimated from tensile strength measurements of aggregates in previous studies and estimated by a simple model ignoring the attractions

between adsorbed molecules, which have been used in the discussion of cohesive force estimation in airless conditions.

Based on the increased cohesive force found in this study, protoplanetary silicate dust may be able to grow at higher collision velocity than predicted by the surface energy at ambient condition, although not to the velocity suggested by the previous study, which assumed a ten-fold increase. It should be noted, however, that the value of surface energy and critical collision velocity for growth used in the predictions are for spheres, and the effect of particle shape is not discussed.

Taking into account the number of contact points between the slide and the particles and the effect of removal of adsorbed water molecules, the typical cohesive forces per a contact point between the constituent particles of C- and S-type asteroids are estimated to be ~0.020–0.059 μN and ~0.065–0.12 μN, respectively. These do not depend on the particle size as long as plastic deformation does not occur. A previous study, based on the cohesive force proportional to the particle size, has shown that the pressure from gravity and cohesive force on the surfaces of sub-km-sized asteroids is minimum for particles of a several tens of centimeters. However, the cohesive force estimates in this study suggest that even if the increase in the number of contact points with increasing particle size is taken into account, the pressure for particles of tens of centimeters or smaller is lower than previously predicted, and is minimized for particles of ~1 cm. The explorations of asteroids have shown that the size of particles ejected from asteroid Bennu is <1-10 cm and the size of particles covering the low areas of asteroid Itokawa is millimeter to centimeter. The estimate of this study is consistent with these observations.

Appendix A

Arithmetic mean roughness

The arithmetic mean roughness, R_a, is defined as follows:

$$R_a = \frac{1}{l} \int_0^l |h(x) - f(x)| \, dx, \tag{A1}$$

where $h(x)$ is the measured height, $f(x)$ is the average curve of the surface, and l is the evaluation length (Gadelmawla et al., 2002). We set the evaluation length, l, to 20 µm, and randomly selected three or four one-dimensional profiles (such as shown in Figure 3-2b) for each particle type. The average curve, $f(x)$, is obtained by m-order polynomial fitting to the selected data sets. The values of m are determined by calculating the Akaike information criterion (AIC; Akaike, 1974) given as follows:

$$\text{AIC} = n \left\{ \ln\left(\frac{2\pi S_e}{n}\right) + 1 \right\} + 2(m + 2), \tag{A2}$$

where n is the number of data points and S_e is the residual sum of squares. The lower the AIC value, the better the fit. Figure A1 shows an example of the data set used and the fitting curves.
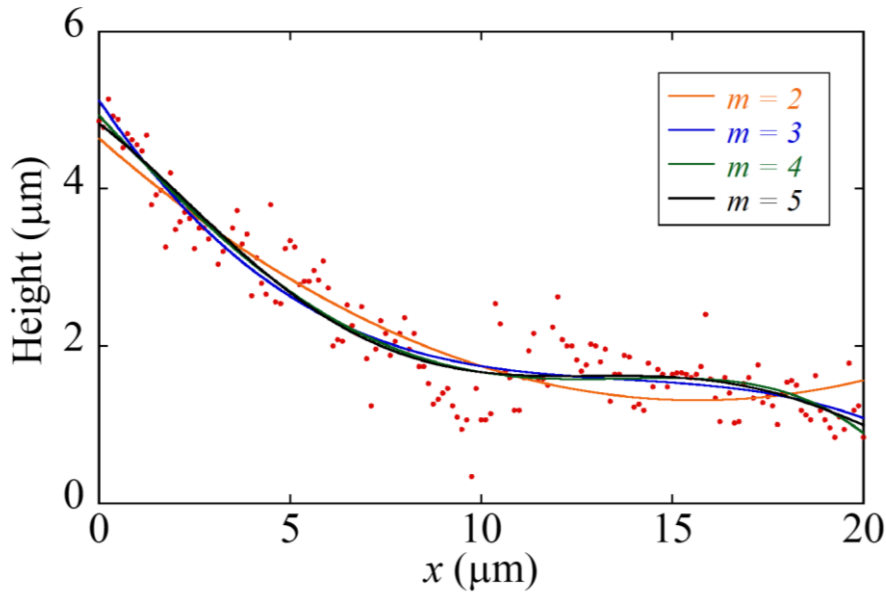

Figure A1 Example of fitting curves for calculating the Ra of particles. In this case, the AIC value became minimal at $m = 4$.

Appendix B

Axial ratio and volume of particles

To estimate the volume of silica sand particles and aggregate from the two-dimensional projection images, we derive an empirical relationship of the shape-dependent coefficient φ_v. In this study, the obtained typical φ_v was 0.12 and 0.08 for Murchison (A_x of 0.72 in average) and glass (A_x of 0.58 in average), respectively, as shown in Figure B1. Using the two data points and $(A_x, \varphi_v) = (1, \pi/6)$, we derived the following empirical relationship:

$$\varphi_v = \frac{\pi}{6} e^{(-4.76 \pm 0.32)(1 - A_x)}. \tag{B1}$$

From this relationship, we assume φ_v = 0.09 and 0.19 for silica sand particles and aggregates with A_x of 0.64 and 0.79 in average, respectively.
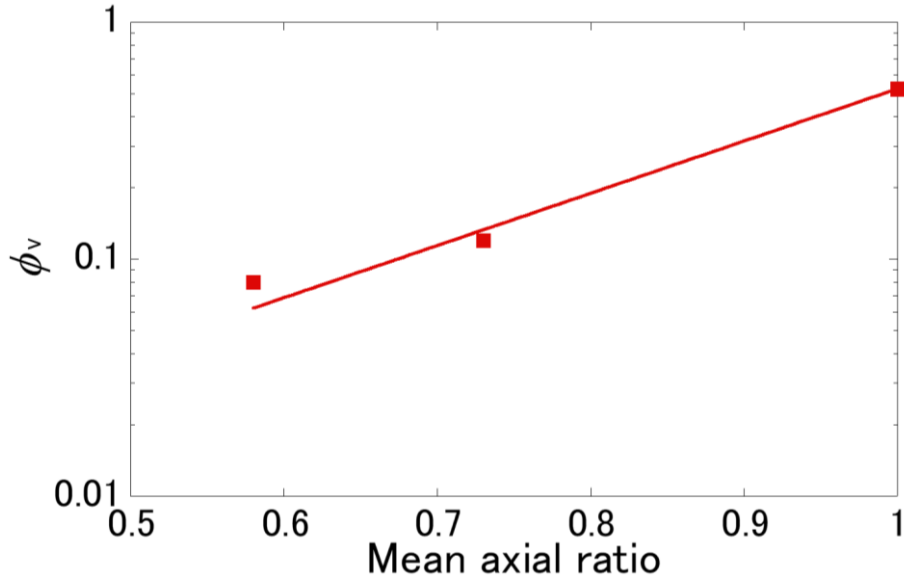

Figure B1 φ_v vs mean axial ratio.

Acknowledgements

References

Adachi, I., Hayashi, C., & Nakazawa, K. The gas drag effect on the elliptic motion of a solid body in the primordial solar nebula. *Progress of Theoretical Physics* **56**, 1756-1771 (1976).

Adolphs, J. & Setzer, M. J. A model to describe adsorption isotherms. *Journal of Colloid and interface science* **180**, 70-76 (1996).

Akaike, H. A new look at the statistical model identification. *IEEE transactions on automatic control* **19**, 716-723 (1974).

Arakawa, S. Revisiting sticking property of submillimetre-sized aggregates. *Monthly Notices of the Royal Astronomical Society* **496**, 2786-2789 (2020).

Bierhaus, E. B., Songer, J. T., Clark, B. C., *et al*. Bennu regolith mobilized by TAGSAM: Expectations for the OSIRIS-REx sample collection event and application to understanding naturally ejected particles. *Icarus* **355**, 114142 (2021).

Bischoff, D., Kreuzig, C., Haack, D., Gundlach, B., & Blum, J. Sticky or not sticky? Measurements of the tensile strength of microgranular organic materials. *Monthly Notices of the Royal Astronomical Society* **497**, 2517-2528 (2020).

Blum, J. & Wurm, G. The growth mechanisms of macroscopic bodies in protoplanetary disks. *Annu Rev Astron Astrophys* **46**, 21-56 (2008).

Bogdan, T., Pillich, C., Landers, J., Wende, H., & Wurm, G. Drifting inwards in protoplanetary discs I Sticking of chondritic dust at increasing temperatures. *Astronomy & Astrophysics* **638**, A151 (2020).

Brilliantov, N., Krapivsky, P. L., Bodrova, A., et al. Size distribution of particles in Saturn's rings from aggregation and fragmentation. *Proceedings of the National Academy of Sciences* **112**, 9536-9541 (2015).

Bromwell L. G. The friction of quartz in high vacuum. Massachusetts Inst. Tech. Res. Rept. R66-18 (1966).

Brown, P. G., Hildebrand, A. R., Zolensky, M. E., *et al*. The fall, recovery, orbit, and composition of the Tagish Lake meteorite: A new type of carbonaceous chondrite. *Science* **290**, 320-325 (2000).

Chokshi, A., Tielens, A. G. G. M., & Hollenbach, D. Dust coagulation. *The Astrophysical Journal* **407**, 806-819 (1993).

Consolmagno, G. J., Britt, D. T., & Macke, R. J. The significance of meteorite density and porosity. *Chemie der Erde – Geochemistry* **68**, 1-29 (2008).

Cuzzi, J. N., Burns, J. A., Charnoz, S., et al. An evolving view of Saturn's dynamic rings.

Science **327**, 1470-1475 (2010).

Dąbrowski, A., Mendyk, E., Robens, E., et al. Investigation of surface properties of lunar regolith part III. *Journal of thermal analysis and calorimetry* **94**, 633-639 (2008).

Delbo, M., Libourel, G., Wilkerson, J., *et al.* Thermal fatigue as the origin of regolith on small asteroids. *Nature* **508**, 233-236 (2014).

Dominik, C., & Tielens, A. G. G. M. The physics of dust coagulation and the structure of dust aggregates in space. *The Astrophysical Journal* **480**, 647 (1997).

Epstein, S., & Taylor Jr, H. P. D/H and O-18/O-16 ratios of H_2O in the 'rusty' breccia 66095 and the origin of 'lunar water'. Lunar and Planetary Science Conference Proceedings **5**, 1839-1854 (1974).

French, R. G., & Nicholson, P. D. Saturn's rings II: Particle sizes inferred from stellar occultation data. Icarus 145, 502-523 (2000).

Fujiwara, A., Kamimoto, G., & Tsukamoto, A. Expected shape distribution of asteroids obtained from laboratory impact experiments. *Nature* **272**, 602-603 (1978).

Fujiwara, A., Kawaguchi, J., Yeomans, D. K., *et al.* The Rubble-Pile Asteroid Itokawa as Observed by Hayabusa. Science **312**, 1330-1334 (2006).

Gadelmawla, E. S., Koura M. M., Maksoud T. M. A., Elewa I.M., Soliman H. H. Roughness parameters. *J Mater Process Technol* **123**, 133–145 (2002).

Gilmour, C. M., Herd, C. D., & Beck, P. Water abundance in the Tagish Lake meteorite from TGA and IR spectroscopy: Evaluation of aqueous alteration. *Meteoritics & Planetary Science* **54**, 1951-1972 (2019).

Goldreich, P., & Ward, W. R. The formation of planetesimals. *The Astrophysical Journal* **183**, 1051-1062 (1973).

Greeley, R., Arvidson, R. E., Elachi, C., *et al*. Aeolian features on Venus: preliminary Magellan results. *Journal of Geophysical Research: Planets* **97**, 13319-13345 (1992).

Greeley, R., & Iversen, J. D. Wind as a geological process on Earth, Mars, Venus and Titan. Cambridge Planetary Science Series **4** (1985).

Güttler, C., Blum, J., Zsom, A., Ormel, C. W., & Dullemond, C. P. The outcome of protoplanetary dust growth: pebbles, boulders, or planetesimals?-I. Mapping the zoo of laboratory collision experiments. *Astronomy & Astrophysics* **513**, A56 (2010).

Gundlach, B. & Blum, J. A new method to determine the grain size of planetary regolith. *Icarus* **223(1)**, 479-492 (2013).

Gundlach, B., Schmidt, K. P., Kreuzig, C., *et al*. The tensile strength of ice and dust aggregates and its dependence on particle properties. *Monthly Notices of the Royal*

Astronomical Society **479**, 1273-1277 (2018).

Haack, D., Otto, K., Gundlach, B., *et al*. (2020). Tensile strength of dust-ice mixtures and their relevance as cometary analog material. *Astronomy & Astrophysics* **642**, A218.

Harbison, R. A., Nicholson, P. D., & Hedman, M. M. The smallest particles in Saturn's A and C Rings. *Icarus* **226**, 1225-1240 (2013).

Hayashi, C. Structure of the solar nebula, growth and decay of magnetic fields and effects of magnetic and turbulent viscosities on the nebula. *Progress of Theoretical Physics Supplement* **70**, 35-53 (1981).

Heavens, N. G., Richardson, M. I., Kleinböhl, A., *et al*. The vertical distribution of dust in the Martian atmosphere during northern spring and summer: Observations by the Mars Climate Sounder and analysis of zonal average vertical dust profiles. *Journal of Geophysical Research: Planets* **116**, E04003 (2011).

Heim, L. O., Blum, J., Preuss, M., & Butt, H. J. Adhesion and friction forces between spherical micrometer-sized particles. *Physical Review Letters* **83**, 3328 (1999).

Hertz, H. Miscellaneous papers, Newyork: Macmillan 146 (1896).

Hibbitts, C. A., Grieves, G. A., Poston, M. J., et al. Thermal stability of water and hydroxyl on the surface of the Moon from temperature-programmed desorption measurements of lunar analog materials. *Icarus* **213**, 64-72 (2011).

Hildebrand, A. R., McCausland, P. J., Brown, P. G., et al. The fall and recovery of the Tagish Lake meteorite. *Meteoritics & Planetary Science* **41**, 407-431 (2006).

Hirabayashi, M., Sánchez, D. P., & Scheeres, D. J. Internal structure of asteroids having surface shedding due to rotational instability. *The Astrophysical Journal* **808**, 63 (2015).

Hirabayashi, M., Scheeres, D. J., Sánchez, D. P., & Gabriel, T. Constraints on the physical properties of main belt comet P/2013 R3 from its breakup event. *The Astrophysical Journal Letters* **789**, L12 (2014).

Holsapple, K. A. Spin limits of Solar System bodies: From the small fast-rotators to 2003 EL61. *Icarus* **187**, 500-509 (2007).

Housen, K. R., Sweet, W. J., & Holsapple, K. A. Impacts into porous asteroids. *Icarus* **300**, 72-96 (2018)

Housen, K. R., Wilkening, L. L., Chapman, C. R., & Greenberg, R. Asteroidal regoliths. *Icarus* **39**, 317-351 (1979).

Iida, K., Otsuka, A., Danjo, K., & Sunada, H. Measurement of the Adhesive Force between Particles and a Substrate by Means of the Impact Separation Method. Effect of the Surface Roughness and Type of Material of the Substrate. *Chemical and pharmaceutical bulletin* **41**, 1621-1625 (1993).

Israelachvili, J. N. Intermolecular and surface forces. Academic press (2011).

Israelachvili, J., & Wennerström, H. Role of hydration and water structure in biological and colloidal interactions. *Nature* **379**, 219-225 (1996).

Johansen, A., Jacquet, E., Cuzzi, J. N., Morbidelli, A., & Gounelle, M. New paradigms for asteroid formation. In Asteroids IV, 1-492 (2015).

Johnson, K. L., Kendall, K., & Roberts, A. Surface energy and the contact of elastic solids. *Proceedings of the royal society of London. A. mathematical and physical sciences* **324**, 301-313 (1971).

Kataoka, A., Tanaka, H., Okuzumi, S., & Wada, K. Fluffy dust forms icy planetesimals by static compression. *Astronomy & Astrophysics* **557**, L4 (2013).

Kendall, K., Alford, N. M., & Birchall, J. D. A new method for measuring the surface energy of solids. *Nature* **325**, 794-796 (1987).

Kimura, H., Wada, K., Senshu, H., & Kobayashi, H. Cohesion of amorphous silica spheres: Toward a better understanding of the coagulation growth of silicate dust aggregates. *The Astrophysical Journal* **812**, 67 (2015).

Kiuchi, M. and Nakamura, A. M. Relationship between regolith particle size and porosity on small bodies. *Icarus* **239**, 291-293 (2014); Corrigendum to "Relationship between regolith particle size and porosity on small bodies". *Icarus* **248**, 221-221 (2015).

Kleinhenz, J. E., Gaier, J., Waters, D., *et al*. Measurement of Cohesion in Asteroid Regolith Materials. In 10th Symposium on Space Resource Utilization (p. 0193) (2017).

Kok, J. F., Parteli, E. J., Michaels, T. I., & Karam, D. B. The physics of wind-blown sand and dust. *Reports on progress in Physics* **75**, 106901 (2012).

Kothe, S., Blum, J., Weidling, R., & Güttler, C. Free collisions in a microgravity many-particle experiment. III. The collision behavior of sub-millimeter-sized dust aggregates. *Icarus* **225**, 75-85 (2013).

Krupp, H. Particle adhesion theory and experiment. *Adv Colloid Interf Sci* **1**, 111-239 (1967).

Kruss, M., Musiolik, G., Demirci, T., Wurm, G., & Teiser, J. Wind erosion on Mars and other small terrestrial planets. *Icarus* **337**, 113438 (2020).

Kruss, M., & Wurm, G. Composition and size dependent sorting in preplanetary growth: seeding the formation of Mercury-like planets. *The Planetary Science Journal* **1**, 23 (2020).

Lam, K. K., & Newton, J. M. Investigation of applied compression on the adhesion of powders to a substrate surface. *Powder Technology* **65**, 167-175 (1991).

LaMarche, C. Q., Leadley, S., Liu, P., Kellogg, K. M., & Hrenya, C. M. Method of quantifying surface roughness for accurate adhesive force predictions. *Chemical Engineering Science* **158**, 140-153 (2017).

Lauretta, D. S., DellaGiustina, D. N., Bennett, C. A., *et al*. The unexpected surface of asteroid (101955) Bennu. *Nature* **568**, 55-60 (2019).

Lorenz, R. D., Wall, S., Radebaugh, J., *et al*. The sand seas of Titan: Cassini RADAR observations of longitudinal dunes. *Science* **312**, 724-727 (2006).

Macke, R. J., Britt, D. T., Consolmagno, G. J. Density, porosity, and magnetic susceptibility of achondrite meteorites. *Meteoritics Planet. Sci.* **46**, 311-326 (2011a)

Macke, R. J., Britt, D. T., Consolmagno, G. J. Density, porosity, and magnetic susceptibility of carbonaceous meteorites. *Meteoritics Planet. Sci.* **46**, 1842-1862 (2011b)

Mann, H. B., & Whitney, D. R. On a test of whether one of two random variables is stochastically larger than the other. *The annals of mathematical statistics* **18**, 50-60 (1947).

Michel, P., Benz, W., Tanga, P., & Richardson, D. C. Collisions and gravitational reaccumulation: Forming asteroid families and satellites. *Science* **294**, 1696-1700 (2001).

Michel, P., O'Brien, D. P., Abe, S., & Hirata, N. Itokawa's cratering record as observed by Hayabusa: Implications for its age and collisional history. *Icarus* **200**, 503-513 (2009).

Michikami, T. Kadokawa, T, Tsuchiyama, A. *et al.* Influence of petrographic textures on the shapes of impact experiment fine fragments measuring several tens of microns: comparison with Itokawa regolith particles. *Icarus* **302**, 109-125 (2018).

Michikami, T., Nakamura, A. M., & Hirata N. The shape distribution of boulders on asteroid 25143 Itokawa: comparison with fragments from impact experiments. *Icarus* **207**, 277-284 (2010).

Michikami, T. Honda, C., Miyamoto, H. *et al.* Boulder size and shape distributions on asteroid Ryugu. *Icarus* **331**, 179-191 (2019).

Miyamoto, H., Yano, H., Scheeres, D. J., *et al*. Regolith migration and sorting on asteroid Itokawa. *Science* **316**, 1011-1014 (2007).

Morota, T., Sugita, S., Cho, Y., et al. Sample collection from asteroid (162173) Ryugu by Hayabusa2: Implications for surface evolution. *Science* **368**, 654-659 (2020).

Nagaashi Y., Omura T., Kiuchi M., *et al.* Laboratory experiments on agglomeration of particles in a granular stream. *Prog Earth Planet Sci* **5**, 52 (2018); Erratum:

Correction to: Laboratory experiments on agglomeration of particles in a granular stream. *Prog Earth Planet Sci* **5**, 71 (2018)

Nagaashi, Y., Nakamura, A. M., Hasegawa, S., & Wada, K. Packing fraction of clusters formed in free-falling granular streams based on flash x-ray radiography. *Physical Review E* **103**, 032903 (2021).

Nakamura, A. Laboratory studies on the velocity of fragments from impact disruptions. *ISAS Report*, p. 651 (1993).

Naray-Szabo, I., & Ladik, J. Strength of silica glass. *Nature* **188**, 226-227 (1960).

Nelson, J. D. & Vey, E. Relative cleanliness as a measure of lunar soil strength. *Journal of Geophysical Research* **73**, 3747-3764 (1968).

Ohtsuki, K., Kawamura, H., Hirata, N., et al. Size of the smallest particles in Saturn's rings. *Icarus* **344**, 113346 (2020).

Ormel, C. W., & Cuzzi, J. N. Closed-form expressions for particle relative velocities induced by turbulence. *Astronomy & Astrophysics* **466**, 413-420 (2007).

Perko, H. A., Nelson, J. D., & Sadeh, W. Z. Surface cleanliness effect on lunar soil shear strength. *Journal of geotechnical and geoenvironmental engineering* **127**, 371-383 (2001).

Pillich, C., Bogdan, T., Landers, J., Wurm, G., & Wende, H. Drifting inwards in protoplanetary discs II: The effect of water on sticking properties at increasing temperatures. *Astronomy & Astrophysics* **652**, A106 (2021).

Polishook, D., Moskovitz, N., Binzel, R. P., *et al*. A 2 km-size asteroid challenging the rubble-pile spin barrier–A case for cohesion. *Icarus* **267**, 243-254 (2016).

Poppe, T., Blum, J., Henning, T., Analogous experiments on the stickiness of Micron-sized Preplanetary dust. *Astrophys. J.* **533**, 454–471 (2000).

Rubincam, D. P. Radiative spin-up and spin-down of small asteroids. *Icarus* **148**, 2-11 (2000).

Rumpf, H. Zur Theorie der Zugfertigkeit von Agglomeraten bei Kraftübertragung an Kontaktpunkten. *Chem. Ing. Techn* **42**, 538-540 (1970).

Sakatani, N., Ogawa, K., Iijima, Y. I., Arakawa, M., & Tanaka, S. Compressional stress effect on thermal conductivity of powdered materials: Measurements and their implication to lunar regolith. *Icarus* **267**, 1-11 (2016).

Salazar-Banda, G. R., Felicetti, M. A., Gonçalves, J. A. S., Coury, J. R., & Aguiar, M. L. Determination of the adhesion force between particles and a flat surface, using the centrifuge technique. *Powder technology* **173**, 107-117 (2007).

Sánchez, P. & Scheeres, D. J. The strength of regolith and rubble pile asteroids. *Meteoritics & Planetary Science* **49**, 788-811 (2014).

Sánchez, P. & Scheeres, D. J. Disruption patterns of rotating self-gravitating aggregates: A survey on angle of friction and tensile strength. *Icarus* **271**, 453-471 (2016).

Schäfer, C. M., Scherrer, S., Buchwald, R., *et al*. Numerical simulations of regolith sampling processes. *Planetary and Space Science* **141**, 35-44 (2017).

Scheeres, D. J., Hartzell, C. M., Sánchez, P., & Swift, M. Scaling forces to asteroid surfaces: The role of cohesion. *Icarus* **210**, 968-984 (2010).

Schneider, C. A., Rasband, W. S., & Eliceiri, K. W. NIH Image to ImageJ: 25 years of image analysis. *Nature methods* **9**, 671-675 (2012).

Shao, Y., & Lu, H. A simple expression for wind erosion threshold friction velocity. *Journal of Geophysical Research: Atmospheres* **105**, 22437-22443 (2000).

Sing, K. S., Everett, D. H., Haul, R. A. W. *et al.* International union of pure commission on colloid and surface chemistry including catalysis* reporting physisorption data for gas/solid systems with special reference to the determination of surface area and porosity. *Pure Appl. Chem* **57**, 603-619 (1985).

Steinpilz, T., Teiser, J., & Wurm, G. Sticking Properties of Silicates in Planetesimal Formation Revisited. *The Astrophysical Journal* **874**, 60 (2019).

Sudo, T. A Geometrical Approach to the Structure of Noncrystalline Silica Precipitates. *Structural Chemistry* **11**, 15-17(2000).

Sugita, S., Honda, R., Morota, T., *et al*. The geomorphology, color, and thermal properties of Ryugu: Implications for parent-body processes. *Science* 364, 6437 (2019).

Sugiura, K., Kobayashi, H., Watanabe, S. I., *et al*. SPH simulations for shape deformation of rubble-pile asteroids through spinup: The challenge for making top-shaped asteroids Ryugu and Bennu. *Icarus* **365**, 114505 (2021).

Takayama, A., & Tomeoka, K. Fine-grained rims surrounding chondrules in the Tagish Lake carbonaceous chondrite: Verification of their formation through parent-body processes. *Geochimica et Cosmochimica Acta* **98**, 1-18 (2012).

Tarasevich, Y. I. Adsorption-calorimetric determination of the surface energy of dispersed oxides. *Theoretical and Experimental Chemistry* **43**, 79-84 (2007).

Telfer, M. W., Parteli, E. J., Radebaugh, J., et al. Dunes on Pluto. *Science* **360**, 992-997 (2018).

Thiel, P. A., & Madey, T. E. The interaction of water with solid surfaces: Fundamental aspects. *Surface Science Reports* **7**, 211-385 (1987).

Tiscareno, M. S., Hedman, M. M., Burns, J. A., & Castillo-Rogez, J. Compositions and origins of outer planet systems: insights from the Roche critical density. *The Astrophysical Journal Letters* **765**, L28 (2013).

Tsuchiyama, A., Uesugi, M., Matsushima, T. *et al.* Three-dimensional structure of

Hayabusa samples: origin and evolution of Itokawa regolith. *Science* **333**, 1125-1128 (2011).

Vaccaro, E. Physical and Chemical Properties of Matrix in Primitive Chondrites. Open University (United Kingdom) (2017).

Vey, E., & Nelson, J. D. Engineering Propeties of Simulated Lunar Soils. Journal of the Soil Mechanics and Foundations Division 91, 25-52 (1965).

Wada, K., Tanaka, H., Okuzumi, S., et al. Growth efficiency of dust aggregates through collisions with high mass ratios. *Astronomy & Astrophysics* **559**, A62 (2013).

Wada, K., Tanaka, H., Suyama, T., Kimura, H., & Yamamoto, T. Collisional growth conditions for dust aggregates. *The Astrophysical Journal* **702**, 1490 (2009).

Wada, K., Tanaka, H., Suyama, T., Kimura, H., & Yamamoto, T. The rebound condition of dust aggregates revealed by numerical simulation of their collisions. *The Astrophysical Journal* **737**, 36 (2011).

Walsh, K. J., Jawin, E. R., Ballouz, R. L., *et al*. Craters, boulders and regolith of (101955) Bennu indicative of an old and dynamic surface. *Nature Geoscience* **12**, 242-246 (2019).

Watanabe, S., Hirabayashi, M., Hirata, N., *et al*. Hayabusa2 arrives at the carbonaceous asteroid 162173 Ryugu—a spinning top–shaped rubble pile. *Science* **364**, 268-272 (2019).

Weidenschilling, S. J. Aerodynamics of solid bodies in the solar nebula. *Monthly Notices of the Royal Astronomical Society* **180**, 57-70 (1977).

Weidenschilling, S. J. Dust to planetesimals: Settling and coagulation in the solar nebula. *Icarus* **44**, 172-189 (1980).

Weidenschilling, S. J., & Cuzzi, J. N. Formation of planetesimals in the solar nebula. In Protostars and planets III (pp. 1031-1060) (1993).

Weidling, R., Güttler, C., & Blum, J. Free collisions in a microgravity many-particle experiment. I. Dust aggregate sticking at low velocities. *Icarus* **218**, 688-700 (2012).

Weisberg, M. K., McCoy, T. J., & Krot, A. N. Systematics and evaluation of meteorite classification. Meteorites early Sol. Syst. II 19–52 (2006).

Wozniakiewicz, P. J., Bradley, J. P., Ishii, H. A., Price, M. C., & Brownlee, D. E. Pre-accretional sorting of grains in the outer solar nebula. *The Astrophysical Journal* **779**, 164 (2013).

Xie, J., Zhu, Z., Yang, T., Dong, M., & Li, R. The effect of incident angle on the rebound behavior of micro-particle impacts. *Journal of Aerosol Science* **155**, 105778 (2021).

Yamamoto, T., Kadono, T., & Wada, K. An examination of collisional growth of silicate dust in protoplanetary disks. *The Astrophysical Journal Letters* **783**, L36 (2014).

Youdin, A. N., & Goodman, J. Streaming instabilities in protoplanetary disks. *The Astrophysical Journal* **620**, 459 (2005).

Zebker, H. A., Marouf, E. A., & Tyler, G. L. Saturn's rings: Particle size distributions for thin layer models. *Icarus* **64**, 531-548 (1985).